INVESTIGATIONS OF ATMOSPHERIC FORCING DURING THE HIGH RESOLUTION MAIN EXPERIMENT

FINAL REPORT

GRANT NUMBERS: N00014-92-J-1585 & N00014-96-0516

James Edson
Applied Ocean Physics & Engineering Department
Woods Hole Oceanographic Institution
Woods Hole, MA 02543-1053
E-mail: jedson@airsea2.whoi.edu
Phone: (508) 289-2935
FAX: (508) 457-2194

1 February 1999

A. Sikora, T.D, G.S. Young, R.C. Beal and J.B. Edson, 1995: On the use of spaceborne synthetic aperture radar imagery of the sea surface in detecting the presence and structure of the convective marine atmospheric boundary layer, *Mon. Weather. Rev., 123*, 3623-3632.

B. Chapman, R.D., L.K. Shay, H.C. Graber, J.B. Edson, A. Karachintsev, C. Trump, and D. B. Ross, 1997: On the accuracy of HF radar surface current measurements: Intercomparison with ship-based sensors, *J. Geophys. Res., 102*, 18737-18748.

C. Vandemark, D., J.B. Edson, and B. Chapron, 1997: Altimeter estimations of sea surface wind stress for light to moderate winds, *J. Atmos. Oceanic Tech., 14*, 716-722.

D. Edson, J.B., A. A. Hinton, K. E. Prada, J.E. Hare, and C.W. Fairall, 1998: Direct covariance flux estimates from mobile platforms at sea, *J. Atmos. Oceanic Tech., 15*, 547-562

E. Hara, T., E.J. Bock, J.B. Edson, and W.R. McGillis, 1998: Observations of short wind waves in coastal waters, *J. Phys. Oceanogr., 28*, 1425-1438.

F. Edson, J.B., and C.W. Fairall, 1998: Similarity relationships in the marine atmospheric surface layer for terms in the TKE and scalar variance budgets, *J. Atmos. Sci., 55*, 2311-2328.

I. Introduction

The long term objective of this research is to relate the information received by radar antennae into relevant atmospheric and oceanic variables at spatial scales of 0.1 to 1 kilometer. Since radar backscatter is dependent on surface conditions, a better understanding of the mechanisms at work will allow researchers to develop new models relating backscatter to geophysical parameters. The improvement in the model physics also will improve their usefulness as interpretive tools in remote sensing studies at much larger scales (e.g., climate studies). Secondly, the simultaneous measurement of short wave spectra with wind stress and direction will allow us to test current theories of the growth and equilibrium of short waves and their modification by current gradients. These theories currently parameterize wind input, long wave interactions, and dissipation in attempting to determine the equilibrium short wave spectrum.

II. Scientific Objectives

The near term objectives of this research is to study the coupling of the atmosphere and ocean in the vicinity of the Gulf Stream. This includes the Gulf Stream edge and associated features such as shingles and current rips. Therefore, the research is aimed at understanding how the ocean and atmosphere interact in regions of marked horizontal inhomogeneities in the sea surface temperature and current fields. These inhomogeneities give rise to sea surface roughness contrasts, atmospheric baroclinicity and frontogenesis. This research is expected to lead to a better understanding of the role of atmospheric forcing in the sea surface features provided by SAR, RAR, and altimeter data.

III. Approach

The PI deployed three meteorological packages during the 1993 High Resolution experiment aboard LADAS [Laser slope gauge, Acoustic Doppler current profiler (ADCP), Attitude measurement unit (AMU), Sonic anemometer] catamaran, the R/V Columbus Iselin, and the USNS Bartlett. The surface fluxes were computed using the inertial-dissipation and bulk aerodynamic methods from all three platforms. Additionally, these fluxes were computed using the direct covariance method aboard the R/V Iselin and LADAS. The direct covariance fluxes were computed after correcting for the platform's waved induced motion using the AMUs (a separate AMU was mounted aboard the Iselin). Additional measurements of the vertical structure of the atmospheric boundary layer were made during rawinsondes launches. This data was analyzed by the PI, Dr. George Young of Penn State, and Dr. Todd Sikora of the Naval Academy.

The influence of ocean currents on surface signatures seen by RAR and SAR were studied by a number of current meters from the various groups. The PI is responsible for the ADCP data from the LADAS and R/V Iselin, and is working with Dr. Rick Chapman of JHU/APL to incorporate his acoustic current meter into this data set (this current meter was mounted at a depth of 1 meter aboard LADAS). This data set was combined with results from the OSCR system, in a collaborative effort with Dr. Chapman and Dr. Lynn Shay of RSMAS at the University of Miami. OSCR remotely measures surface currents with a HF Radar, which provides a mesoscale map of the surface currents.

Finally, a quantitative measure of the scattering elements imaged by the radar systems was made using the Laser slope gauge deployed by Dr. Erik Bock of WHOI and Prof. Tetsu Hara of the University of Rhode Island. This device is capable of measuring the directional gravity-capillary wave spectra under a variety of conditions.

IV. Tasks Completed

The meteorological and near surface current data taken aboard the R/V Iselin, USNS Bartlett and LADAS catamaran have been merged into a single data set. This data set has been filtered to minimize the uncertainty due to flow distortion on these measurements. The data set includes 10 minute mean atmospheric and ocean surface variables (wind speed and direction, air and sea temperature, humidity, and near surface currents), surface flux estimates computed using the bulk and inertial-dissipation methods, and ship position. This data was made available to all High Resolution participants through an anonymous ftp site at JHU/APL.

Direct covariance estimates were also been computed from the R/V Iselin and LADAS data sets. This required removal of the platform motion from the velocity measurements before computing the covariances. These fluxes agreed extremely well with both the bulk and inertial-dissipation fluxes. These measurements are available to other members of the scientific community upon request. The direct covariance fluxes are been used in the collaborative studies described below.

V. Results

Investigations aimed at gaining a better understanding of the marine boundary layers require accurate and reliable *in situ* measurements of atmospheric and oceanic turbulence statistics. In collaboration with scientist's at NOAA's Environmental Technologies Laboratory and engineers at WHOI/AOP&E, the PI has developed systems that can compute accurate direct covariance flux estimates from moving platforms such as buoys, catamarans, coastal research vessels, and ocean going ships. The system designed at WHOI was primarily tested during the two field experiments of the High Resolution program during the summers of 1991 and 1993 (*Edson et al.*, 1998). The system developed during these experiments allowed me to acquire direct covariance fluxes from both a towed catamaran and the ship itself.

The Direct Covariance Flux System (DCFS) has led to a number of interesting collaborations and investigations that were aimed at improving the way we use satellite and remotely sensed data to investigate the sea surface and initialize numerical forecast models. These investigations and subsequent publications have made significant contributions to our understanding of how atmospheric forcing affects the surface roughness (*Hara et al.*, 1998) and, thereby, microwave radar return.

These results have shown that simple relationships between wind stress and surface roughness break down in situations where there is strong convective activity, and/or slicks are present. For example, a collaborative effort between Dr. Todd Sikora (Naval Academy), Dr. George Young (PSU), Dr. Robert Beal (JHU/APL) and the PI was undertaken to interpret SAR imagery of the ocean surface under highly convective conditions. These investigations led to a means of interpreting satellite imagery to provide information about the boundary layer height and surface heat fluxes (*Sikora et al.*, 1995) using the horizontal scale provide by SAR imagery of convective cells.

A second study was undertaken with Dr. Douglas Vandemark of NASA/Goddard using his altimeter data from the High Resolution Main Experiment. In this effort, the measured fluxes were used to validate of a model that estimates momentum fluxes from altimeter data (*Vandemark et al.*, 1997). This research clearly showed that atmospheric stability must be taken into account to properly interpret remotely sensed imagery of the ocean surface under light to moderate wind conditions.

A third study involved an investigation of the remotely sensed currents taken from the OSCR system. The PI worked extensively with oceanographers from the High Resolution program to help validate a land-based OSCR system, which is capable of remotely mapping the near surface current field out to 30 km from the coast (*Chapman et al.*, 1997). This type of technology is becoming an extremely useful tool for coastal studies as it provides the 2-D structure of the current field.

Finally, the study reported in *Edson and Fairall* (1998) involved an in depth investigation of the applicability of MO-similarity theory to the marine surface layer above the wave boundary layer (WBL). The paper demonstrated that the theory is valid in this region. It has provided researchers with an understanding of the turbulence properties at the upper limit of the WBL, which has been used as a starting point for our investigations of the WBL during ONR's Marine Boundary Layers and Coastal Mixing and Optics programs.

All of these investigations are described in detail in the following papers.

REPORT DOCUMENTATION PAGE	*Form Approved* *OMB no. 0704-0188*

1. AGENCY USE ONLY *(Leave blank)*

2. REPORT DATE
12 March 1999

3. REPORT TYPE AND DATES COVERED
Final Report 5/1/92-6/30/95 & 1/1/96-12/31/98

4. TITLE AND SUBTITLE
Post Analysis and Continued Improvement of Motion Compensating Flux System Abroad the LADAS Platform and Statistical Characteristics of Small Scale Wind-Waves and Their Modulation by Longer Gravity Waves and Atmospheric Forcing

5. FUNDING NUMBERS
N00014-92-J-1585
and
N00014-96-1-0516

6. AUTHOR(S)
Dr. James B. Edson

7. PERFORMING ORGANIZATION NAME(S) AND ADDRESS(ES)
Woods Hole Oceanographic Institution
Applied Ocean Physics and Engineering Department
98 Water Street, MS #10
Woods Hole, MA 02543-1053

8. PERFORMING ORGANIZATION REPORT NUMBER

9. SPONSORING/MONITORING AGENCY NAME(S) AND ADDRESS(ES)

10. SPONSORING/MONITORING AGENCY REPORT NUMBER

11. SUPPLEMENTARY NOTES

12a. DISTRIBUTION/AVAILABILITY STATEMENT
Approved for public release; distribution is unlimited

12b. DISTRIBUTION CODE

13. ABSTRACT *(Maximum 200 words)*
See attached report

14. SUBJECT TERMS
radar backscattering, short wave spectra, and wind stress.

15. NUMBER OF PAGES
5

16. PRICE CODE

17. SECURITY CLASSIFICATION OF REPORT unlimited	**18. SECURITY CLASSIFICATION OF THIS PAGE** unlimited	**19. SECURITY CLASSIFICATION OF ABSTRACT** unlimited	**20. LIMITATION OF ABSTRACT** unlimited

Reprinted from MONTHLY WEATHER REVIEW, Vol. 123, No. 12, December 1995
American Meteorological Society

Jse of Spaceborne Synthetic Aperture Radar Imagery of the Sea Surface in Detecting the Presence and Structure of the Convective Marine Atmospheric Boundary Layer

T. D. SIKORA AND G. S. YOUNG
The Pennsylvania State University, University Park, Pennsylvania

R. C. BEAL
The Johns Hopkins University Applied Physics Laboratory, Laurel, Maryland

J. B. EDSON
Woods Hole Oceanographic Institution, Woods Hole, Massachusetts

3 January 1995 and 14 June 1995

ABSTRACT

Two distinct backscatter regimes are seen on a European remote sensing satellite *ERS-1* C-band (5.6 cm) synthetic aperture radar (SAR) image of the sea surface during a time of fair synoptic-scale weather conditions. One backscatter regime is mottled. In contrast to that, the second backscatter regime is marbled.

The authors hypothesize that the mottled backscatter pattern is a characteristic SAR backscatter pattern linked to the presence of the convective (i.e., statically unstable/convective-eddy containing) marine atmospheric boundary layer (CMABL) and can be used to help determine CMABL structure [convective-eddy type (cellular convection versus longitudinal rolls), eddy wavelength, and CMABL depth (via mixed-layer similarity theory for aspect ratio)]. The hypothesis linking the presence and structure of the CMABL to the mottled backscatter pattern on SAR imagery is validated by analyzing data from a number of sources gathered in the vicinity of the boundary between the mottled and marbled regimes on the SAR image.

. Introduction

In situ studies of the convective (i.e., statically un:able/convective-eddy containing) marine atmo)heric boundary layer (CMABL) have been much ıore common than remote sensing studies of the MABL. Numerous field and laboratory experiments ave resulted in detailed discussions of CMABL air–ea fluxes (e.g., vertical eddy fluxes of heat, momenım, and moisture) as well as the convective boundaryıyer-spanning eddies (BLSEs) [convective updraft CU)-convective downdraft (CD) couples] that transıit these fluxes through the CMABL (Liu et al. 1979; enschow and Stephens 1980; Greenhut and Khalsa 982; Khalsa and Greenhut 1985; Fairall et al. 1990; chumann and Moeng 1991; Sikora and Young 1993; nong others).

These studies have revealed that the intensity of air–sea fluxes—as well as the BLSEs through which they are realized—are functions of many variables. To satisfy the need for universal diagnoses of marine atmospheric boundary layer (MABL) flux and eddy statistics, boundary layer similarity relationships have been developed and applied. [See Stull (1988) for an overview of boundary layer similarity theory.] Similarity theory offers a valuable means of relating the statistics of similarity stratified boundary layers through the use of scaling parameters and nondimensional relationships (Lenchow and Stephens 1980; Khalsa and Greenhut 1985; Young 1988; Sikora and Young 1994). Given the resulting similarity formulas and in situ measurements of the scaling parameters [i.e., CMABL depth z_i and the air–sea fluxes], quantitative estimates of the turbulence statistics for a particular CMABL can be calculated.

We will show in the present research that similarity theory can also provide a powerful tool in spaceborne synthetic aperture radar (SAR) remote sensing studies of the CMABL. We will combine traditional boundary layer similarity theory with a new concept we call SAR

Corresponding author address: Todd D. Sikora, Department of eteorology, College of Earth and Mineral Sciences, The Pennsylınia State University, 503 Walker Building, University Park, PA 802-5013.

similarity (based on pattern recognition) in order to relate backscatter patterns seen on SAR imagery of the sea surface with corresponding CMABL morphology.

Previous spaceborne SAR studies have suggested that kilometer-scale backscatter patterns seen on SAR imagery of the sea surface are manifestations of BLSEs contained within the CMABL (Gerling 1986; Alpers and Brummer 1994; Beal et al. 1994; Nilsson and Tildesley 1995; among others). These kilometer-scale backscatter patterns are thought to be linked to BLSE-induced sea surface roughness patterns composed of waves of centimeter-scale wavelength. These kilometer-scale BLSE-induced sea surface roughness patterns can be detected by SAR in the absence of appreciable non-CMABL sea surface wave forcing phenomena (e.g., heavy slicks that dampen the sea surface roughness field and strong synoptic-scale surface winds that enhance the sea surface roughness field).

Unfortunately, the sea surface SAR imagery acquired in previous studies has not been analyzed with respect to a concurrent, high-resolution boundary layer dataset. For this reason, there has been no hard evidence linking kilometer-scale backscatter patterns on SAR imagery of the sea surface with the presence of MABL convection. In the present research, we will investigate the link between kilometer-scale backscatter patterns on SAR imagery of the sea surface and CMABL morphology using conventional boundary layer theory and supporting meteorological and oceanographic data.

a. Theory

BLSE-induced sea surface roughness patterns result from the mixing down of high-momentum air within the CDs of BLSEs. This transport of high-momentum air into the convective marine atmospheric surface layer (CMASL) is in accordance with parcel mixing theory (Stull 1988) and has been reported in the observational literature (e.g., Wilczak 1984; Khalsa and Greenhut 1985; Schumann and Moeng 1991; Sikora and Young 1993). As the downward-moving, high-momentum air approaches the sea surface, its presence results in a vertical "squeezing" of the CMASL wind profile and, hence, an increase of the CMASL vertical wind shear. This increased wind shear results in enhanced transfer of high-momentum air to the sea surface by CMASL eddies (the feet of BLSEs). As the high-momentum air reaches the sea surface, it spreads out in the form of gusts in the general direction of the boundary-layer mean wind, enhancing sea surface roughness (Watts 1987). The reverse occurs within CUs where vertical "stretching" of the CMASL wind profile reduces the CMASL vertical wind shear. In summary then, the expected footprint of a field of BLSEs in the presence of a boundary layer mean wind is enhanced sea surface roughness beneath and down mean wind of each CD combined with decreased sea surface roughness beneath and down mean wind of each CU.

If there exists such repeatable sea surface roughness signatures that are the footprints of BLSEs, there should also exist repeatable backscatter signatures on SAR imagery of the sea surface beneath the CMABL revealing these footprints. The occurrence of these backscatter signatures on SAR imagery of the sea surface could then be looked upon as being a *characteristic* backscatter pattern depicting the presence of the CMABL.

Numerous conditional sampling and compositing studies of the convective boundary layer (e.g., Khalsa and Greenhut 1985; Young 1988; Schumann and Moeng 1991) and spectral studies of the convective boundary layer (e.g., Kaimal et al. 1972; LeMone 1973; Kaimal et al. 1976; Young 1987) have shown that the occurrence of BLSEs is indeed repeatable, and hence, the occurrence of maxima in CMASL horizontal velocity is a repeatable feature of this phenomenon. In addition, these studies have shown that the horizontal wavelengths of BLSEs as well as peak wavelengths of horizontal velocity spectra are a function of z_i via mixed-layer similarity theory for BLSE aspect ratio (defined as BLSE wavelength divided by z_i). Kaimal et al. (1976) go on to show that the peak wavelength of horizontal velocity spectra does not vary with height from z_i right down to the surface and is approximately $1.5z_i$. These observations lead us to believe that the dominant wavelength of BLSE-induced backscatter signatures from the sea surface, as seen by SAR, can be related to BLSE wavelength and z_i through mixed-layer similarity theory for aspect ratio (discussed in section 3c).

It follows then that in the absence of appreciable non-CMABL sea surface wave forcing phenomena, SAR images of the sea surface depicting characteristic (BLSE induced) backscatter patterns reveal MABLs of similar (convective) stability and can be used to help determine CMABL structure [BLSE type (cellular convection versus longitudinal rolls), BLSE wavelength, and z_i (via mixed-layer similarity theory for aspect ratio)]. These relationships between SAR backscatter patterns from the sea surface and CMABL morphology are what we call SAR similarity.

It should be emphasized here that the idea of SAR similarity in the present research is limited to the CMABL. The concept of SAR similarity is not applied in the present research to the nonconvective (i.e., non-BLSE containing) MABL, as we do not feel there is a single characteristic (i.e., SAR similar) SAR backscatter pattern for the nonconvective MABL (discussed in section 3a). In the following discussion, the references to and use of nonconvective MABL in situ data and corresponding SAR imagery (we use that of the statically stable MABL) are done solely to contrast what is seen there to what is seen for the CMABL.

The concept of SAR similarity is not without precedent. Pattern recognition for feature identification has been used extensively throughout the remote sensing/image analysis community (e.g., Swain et al. 1981; Kandel 1982; Ebert 1987; Key 1990). Putting it in a more meteorological context, the use of SAR similarity n detecting the presence and structure of the CMABL s analogous to the recognition of boundary layer cumulus clouds on a visible satellite image, followed then by an interpretation of the corresponding boundary ayer stability and structure (e.g., Miura 1986).

Note, however, that in contrast to Miura's methods, SAR is neither attenuated by clouds nor dependent on clouds. In other words, SAR can "see" through intervening cloud layers and does not require the presence of specific characteristic clouds to be of use in CMABL studies. SAR, therefore, has the advantage of being able o measure the effect of CMABL circulations on the sea surface in both the presence and absence of clouds.

Given all the above, SAR imagery has the potential o provide real-time qualitative and quantitative assessments of MABL static instability and CMABL strucure from BLSE-induced backscatter patterns. The concept of SAR similarity can facilitate CMABL research and operational analysis in regions where in situ meaurements are unavailable and is equally applicable in loudy and cloud-free regions.

. ERS-1 *SAR data*

Figure 1 shows a European remote sensing satellite *ERS-1* C-band (5.6 cm) SAR image of the sea surface aken over the northwestern edge of the Gulf Stream North Wall (GSNW), just east of the North Carolina oast (referred to as the imaged area). The image is rom *ERS-1* orbit 10 047 at 1538 UTC 17 June 1993. he SAR image, composed of portions of two adjacent 00-km-square frames, is approximately 100 km in the ross-track direction by 140 km in the along-track diection, with a pixel size of 100 m. In the cross-track irection, a systematic trend resulting from the radar ntenna pattern has been removed, and the resulting adar backscatter variations have been linearly exanded to use the full dynamic range of display. Using he frame corner coordinates as guides, a reference grid identical to that used in Figs. 4–7) has been supermposed on the image.

Goals

Within Fig. 1, areas of enhanced sea surface roughess appear as lighter shaded pixels, while darker pixels enote a more quiescent sea surface. Two distinct backcatter regimes can be seen in Fig. 1. The first is a mottled backscatter pattern seen throughout the southast portion of the image. The second is a marbled ackscatter pattern seen throughout the northwest poron of the image. The border between these two backscatter regimes lies approximately from 35.45°N, 74.95°W to 36.15°N, 73.75°W. It will be shown later that this border lies along the GSNW.

We hypothesize that the mottled backscatter pattern seen in Fig. 1 is a characteristic SAR backscatter pattern linked to the presence of the CMABL and can be used to help determine CMABL structure in the presence of fair synoptic-scale weather conditions (e.g., calm to light surface winds, precipitation free). The logic behind the development of our hypothesis linking the presence and structure of the CMABL to the mottles was described above in section 1a using CMASL air–sea momentum flux/BLSE footprint arguments. In the following sections, our hypothesis is given credence by demonstrating the occurrence of mottles in previous SAR studies of the sea surface. Our hypothesis is validated by analyzing National Climatic Data Center (NCDC), National Meteorological Center (NMC), National Oceanic and Atmospheric Administration (NOAA), and National Weather Service (NWS) analysis products, as well as data taken during experiment High-Resolution 2 (HI-RES 2), from the mottled and marbled backscatter regimes in the vicinity of the GSNW. For a review of HI-RES 2, see Thompson et al. (1994).

2. Meteorological conditions

Synoptic-scale meteorological conditions in the imaged area were uniformly fair at the time of the *ERS-1* overpass. Figure 2 shows the 1500 UTC 17 June 1993 surface analysis generated at NCDC. A stationary front extends from western North Carolina northeastward to a weak low pressure wave near Virginia Beach, Virginia. From the low pressure wave, the stationary front continues east-southeastward over the Atlantic Ocean. The imaged area was therefore located within a uniform, relatively warm air mass south of this front. This situation is consistent with HI-RES 2 shipboard-measured mean wind speeds of 4–5 kt from the west-southwest during this period.

NMC upper-air analyses from 1200 UTC 17 June 1993 (not shown) showed the imaged area to be just east of a large upper-air ridge. At Cape Hatteras (HAT), 850-mb winds were 10 kt from the northeast, 700-mb winds were 10 kt from the north, and 500-mb winds were 10 kt from the northwest.

Inspection of the NMC surface analyses between 1200 and 1800 UTC (not shown) indicated no precipitation over eastern North Carolina or adjacent coastal waters. In addition, NWS radar composites from 1235 UTC 17 June 1993 through 1835 UTC 17 June 1993 (not shown) showed the imaged area, as well as all of eastern North Carolina, to be free of precipitation. Given all the above information, it can be concluded that the imaged area was located within a region of undisturbed weather on the synoptic scale. Thus, the observed variation in SAR backscatter pattern across the imaged area is not of synoptic origin.

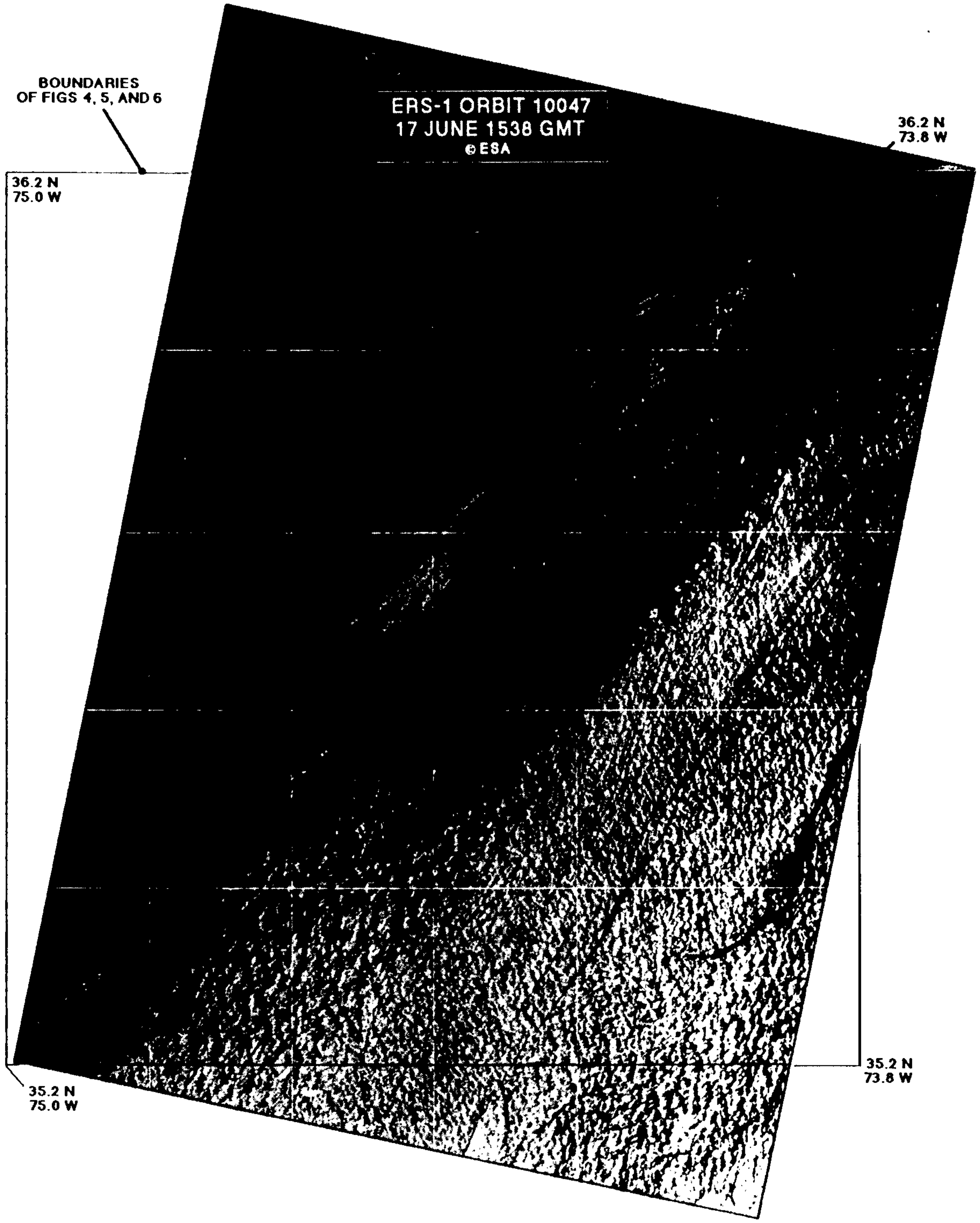

FIG. 1. *ERS-1* SAR backscatter patterns in the imaged area at 1538 UTC 17 June 1993. Two distinct patterns of sea surface roughness are detected by SAR within the imaged area. The first is a mottled backscatter pattern throughout the southeast portion of the image. The second is a marbled backscatter pattern throughout the northwest portion of the image.

While no synoptic-scale disturbed weather system was depicted on NMC analyses over the imaged area, observation notes from meteorological personnel aboard the R/V *Columbus Iselin,* participating in experiment HI-RES 2 within the imaged area, report an atmospheric mesofront in the vicinity of the GSNW.

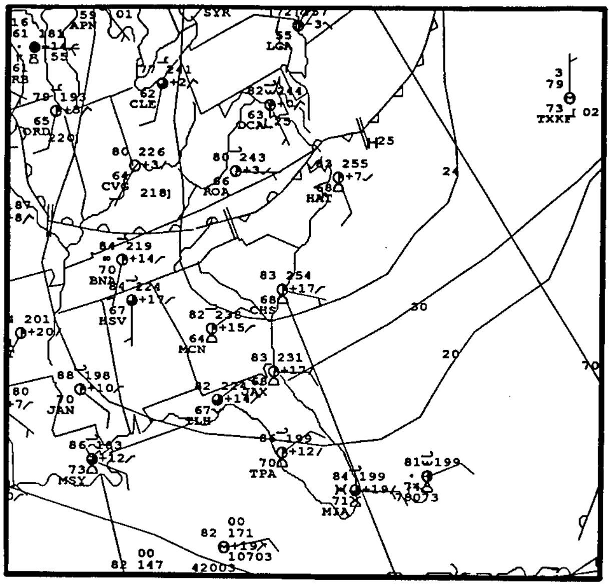

FIG. 2. Synoptic surface analysis for 1500 UTC 17 June 1993.

Clear and calm conditions were reported on the nearshore side of this mesofront, while light winds and boundary layer cumulus clouds were observed on the offshore, Sargasso Seaside. The response of the *ERS-1* SAR backscatter in the vicinity this atmospheric–oceanic front will be the emphasis of the following discussion.

3. Discussion

a. Boundary layer stability

As discussed in section 1, we assert that the mottles seen on the southeast portion of Fig. 1 result from kilometer-scale modulations of the capillary (centimeter scale) sea surface wave field caused by air–sea momentum flux patterns associated with sea surface footprints of BLSEs. These wave patterns are akin to cat's-paws rippling across a pond during conditions of strong turbulence, such as those presented by Dorman and Mollo-Christensen (1973). The hypothesized convectively induced mottles seen in the present research, however, exhibit scales on the order of z_i as opposed to Dorman and Mollo-Christensen's shear-driven cat's-paws that have scales on order of meters.

Additional examples of this type of mottled backscatter pattern have been seen in numerous SAR images of the sea surface, such as that seen in Fig. 3a provided by Beal et al. (1994). The literature provides ample examples of this characteristic backscatter pattern from many different SAR platforms. Gerling (1986) uses Seasat SAR to show such kilometer-scale variations in the radar backscatter. Beal et al. (1994) present a mosaic of backscatter patterns seen by *ERS-1* SAR, including the characteristic mottled backscatter pattern. Trokhimovsky et al. (1994) reported JPL and *ERS-1* C-band SAR detection of the characteristic mottled pattern. Nilsson and Tildesley (1995) also make reference to the mottled backscatter pattern seen on *ERS-1* SAR imagery. These observations demonstrate the characteristic nature of mottles on SAR imagery of the sea surface and therefore lend credence the concept of SAR similarity.

In contrast to the mottled backscatter pattern, it is believed that the marbled backscatter pattern, evident on the region encompassing the northwest portion of Fig. 1, is related to the occurrence of a statically stable MABL in that region. Additional examples of marbling on SAR imagery can be seen in Fig. 3b (provided by Beal et al. 1994) as well as in Nilsson and Tildesley (1995). This marbling most likely occurs due to the combination of calm surface winds in a statically stable MABL and the presence of sea surface surfactant slicks (SSSS) (Nilsson and Tildesley 1995). Therefore, this marbling is probably not a characteristic SAR backscatter pattern depicting the effect of the structure of the statically stable MABL on the sea surface in the presence of fair synoptic-scale weather conditions. Rather, it is a manifestation of several different small-scale oceanic and large-scale atmospheric factors. It is beyond the scope of this paper to thoroughly discuss the detection and morphology of SSSS and the marbled backscatter pattern on SAR imagery. For further review of this topic, the reader is directed to Najjar (1992), Huhnerfuss et al. (1994), and Nilsson and Tildesley (1995).

As stated earlier, the sea surface SAR imagery acquired in previous studies have not been analyzed with respect to a concurrent, high-resolution boundary layer dataset. For this reason, there has been no hard evidence linking the mottles seen in SAR imagery of the sea surface to MABL convection. In the present research, our hypothesis linking the existence of mottled backscatter patterns on SAR imagery of the sea surface to the presence and structure of CMABLs will be val-

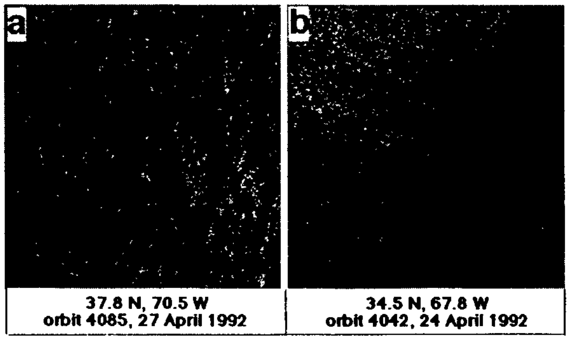

37.8 N, 70.5 W
orbit 4085, 27 April 1992

34.5 N, 67.8 W
orbit 4042, 24 April 1992

FIG. 3. Excerpts of *ERS-1* SAR imagery provided by Beal et al. (1994) along with appropriate center coordinates, orbit number, and date showing (a) a mottled backscatter pattern and (b) a marbled backscatter pattern. Horizontal dimensions are 10 km.

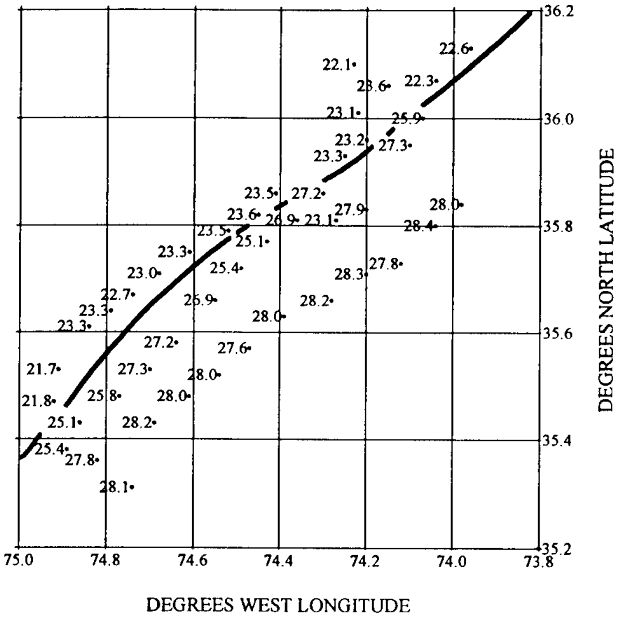

FIG. 4. Map of 10-min mean SSTs (°C) taken aboard the R/Vs *Columbus Iselin* and *Bartlett* from 0002 UTC 16 June 1993 through 2236 UTC 18 June 1993. The GSNW is depicted by the dark solid line. Note the wonderful alignment of the GSNW with the marble–mottle demarcation seen in Fig. 1.

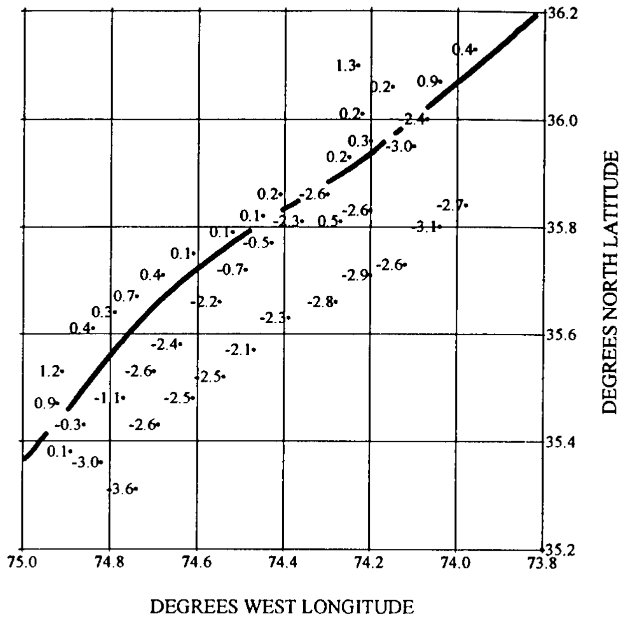

FIG. 5. Same as in Fig. 4 but for T_{air} at 10 m − T_{sea} (°C). Note that negative values are seen to the east of the GSNW, indicative of a CMABL. In contrast, positive values are found to the west of the GSNW indicative of a statically stable MABL.

idated using such a dataset composed of observations from a number of sources.

Inspection of the NOAA oceanographic features analysis (OFA) for 17 June 1993 (not shown) indicated that the border between the two backscatter regimes seen in Fig. 1 lies along the GSNW. The OFA showed sea surface temperatures (SSTs) in the imaged area to be in the range of 22°–24°C on the western side of the GSNW and 27°–28°C on the eastern side. This observation suggests that MABL convection was more likely to the east of the GSNW rather than to the west of the GSNW. To confirm or deny the existence of a CMABL on either side of the GSNW, a high-resolution MABL dataset needs to be employed, such as that taken aboard the R/Vs *Columbus Iselin* and *Bartlett* during experiment HI-RES 2.

In the following discussion, most in situ ship data presented from HI-RES 2 to the south and east of the GSNW, over the mottled regime, are from the R/V *Columbus Iselin*. Most in situ ship data presented from HI-RES 2 to the north and west of the GSNW, over the marbled regime, are from the R/V *Bartlett*. All in situ ship data presented from HI-RES 2 are 10-min means.

Figure 4 shows a map of 10-min mean SSTs (°C) taken aboard the R/Vs *Columbus Iselin* and *Bartlett* from 0002 UTC 16 June 1993 through 2236 UTC 18 June 1993. The GSNW, depicted as a dark solid line in Fig. 4, aligns rather well with the mottle–marble interregime border seen in Fig. 1. Figure 5 is a corresponding map of air–sea temperature difference (°C) (T_{air} at 10 m − T_{sea}). As is expected from the hypothetical interpretation of the SAR image, negative values of air–sea temperature difference are generally seen to the east of the GSNW, indicative of a CMABL.

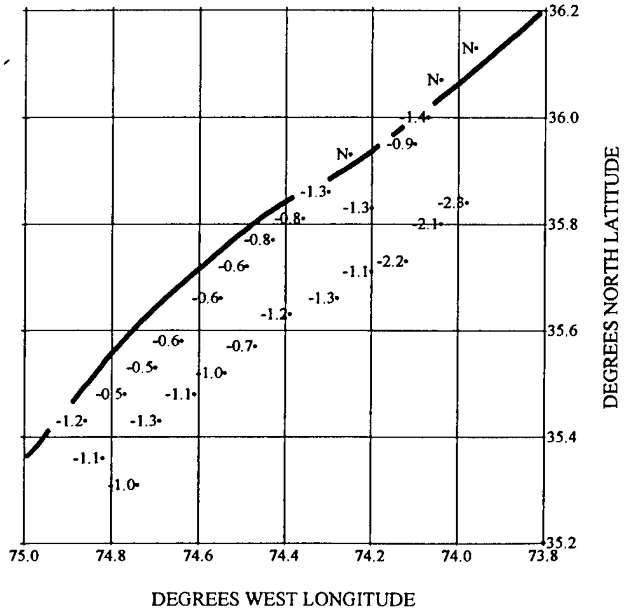

FIG. 6. Map of ratios of instrument height (z = 10 m) to Obukhov length L (m) (z/L) corresponding to R/V *Columbus Iselin* datapoint locations in Figs. 4 and 5. The GSNW is depicted by the dark solid line. Static instability is found to the east of the GSNW.

n contrast, positive values are observed to the west of he GSNW, indicative of a statically stable MABL.

Another measure of MABL static stability can be determined using Monin–Obukhov similarity. [See Stull (1988) for a review of Monin–Obukhov similarty theory.] Figure 6 shows ratios of instrument height $z = 10$ m) versus Obukhov length L (m):

$$\frac{z}{L} = \frac{-zkg\overline{(w'\theta_v')_s}}{\overline{\theta}_v u_*^3}, \qquad (1)$$

corresponding to *Columbus Iselin* data point locations n Figs. 4 and 5. (Insufficient data prevented the calculation of z/L at Bartlett datapoint locations.) In (1), is the von Kármán constant (0.40), g is the acceleration due to gravity (9.8 m s^{-2}), $\overline{(w'\theta_v')_s}$ is the air–sea buoyancy flux (m s^{-1} K), $\overline{\theta}_v$ is the average virtual potential temperature (K), and u_* is the friction velocty (m s^{-1}).

It is important to note here that the fluxes from the R/V *Columbus Iselin* were computed using the direct ovariance method (Hare et al. 1992). Therefore, the ign of z/L is determined by the fluxes themselves and not by the sign of the air–sea temperature difference, as would be the case with the bulk and inertial dissipation methods. Thus, the z/L map provides a stability ield independent of the air–sea temperature difference map. The results seen in Fig. 6 for z/L show that static nstability was generally observed to increase (increasing negative values of z/L) the farther east of the GSNW the *Columbus Iselin* sailed. Neutral stability i.e., zero buoyancy flux), denoted by "N" on Fig. 6, s seen in a few locations adjacent to the front.

The above in situ observations, combined with Monin–Obukhov similarity theory, support our hyothesis linking boundary layer convection with the observed mottled SAR backscatter pattern. Over warm waters east of the GSNW, where the mottled backscatter pattern appears on the SAR imagery, a CMABL s observed. In contrast, over cool waters to the west f the GSNW, where marbling appears on the SAR magery, a statically stable MABL is observed. As tated earlier, it is believed from previous studies that he marbling seen beneath the statically stable MABL esults from the combination of calm surface winds associated with the statically stable MABL and the presnce of SSSS (Najjar 1992; Huhnerfuss et al. 1994; Nilsson and Tildesley 1995).

The close spatial correspondence between the moted/marbled SAR regimes and the statically unstable/ table MABL stability regimes in the present research, combined with the characteristic nature of mottles as een in previous SAR studies of the sea surface, suports the use of SAR similarity. [That is, we believe here is a one-to-one match between the occurrence of he characteristic SAR backscatter pattern at a point mottled) and the occurrence of the corresponding atmospheric phenomena present at that point (CMABL).] Admittedly, though, we do find in Fig. 1 a portion of the in situ data containing the CMABL regime that does not contain mottles. This portion lies directly adjacent to the GSNW near its southwestern-most extent in Fig. 1. An explanation of this phenomenon is given in section 3c.

b. BLSE type: Cells or rolls

Within convective boundary layers, two distinct types of boundary layer circulation have been noted in the literature, cellular convection and longitudinal rolls (e.g., Woodcock 1975; Deardorff 1976; Brown 1980; Miura 1986; Alpers and Brummer 1994). The occurrence of one type or the other is dependent on the degree of boundary layer wind shear and instability (Haack and Shirer 1992). Unfortunately, accurate MABL wind data within the imaged area for 17 June is lacking. This shortcoming of the available soundings hinders the use of mixed-layer similarity theory to diagnose the type of BLSE present within the mottled regime of Fig. 1. Observational results presented by Woodcock (1975) and verified theoretically by Deardorff (1976) can, however, be used to diagnose the type of BLSE from just the air–sea temperature difference and the wind speed at 10 m using surface-layer similarity.

Inspection of the *Columbus Iselin* in situ dataset reveals that the wind speed at 10 m above sea level never exceeded 6 m s^{-1} during 17 June 1993, while the air–sea temperature differences on the Sargasso Seaside of the GSNW ranged up to −3.6°C. Using these values as inputs into the nomogram given by Woodcock (1975) and Deardorff (1976) (not shown) suggests that cellular convection rather than longitudinal rolls are dominant within at least that part of the mottled regime of Fig. 1 where in situ data are available. The agreement of this result with the observed cellular shape and intermittent distribution of the mottles leads us to believe that the mottled SAR backscatter pattern of the sea surface is the characteristic backscatter pattern of CMABL cellular convection. This cellular backscatter pattern is in contrast to the linear banded *ERS-1* SAR backscatter pattern observed in Alpers and Brummer (1994) and thought to be the result of longitudinal rolls.

When viewing Fig. 1, occasional linear southwest–northeast streaks are apparent far to the southeast of the GSNW, out of the area in Figs. 4–6 containing in situ data. These streaks may be the result of linear stretched SSSS or they may be the SAR backscatter pattern of boundary layer roll vortices. Future research will include the detailed analysis of in situ atmospheric and oceanographic data within this region in an effort to explain the streaks.

c. Aspect ratio

Recall from section 1a that numerous boundary layer compositing and spectral studies have shown that the

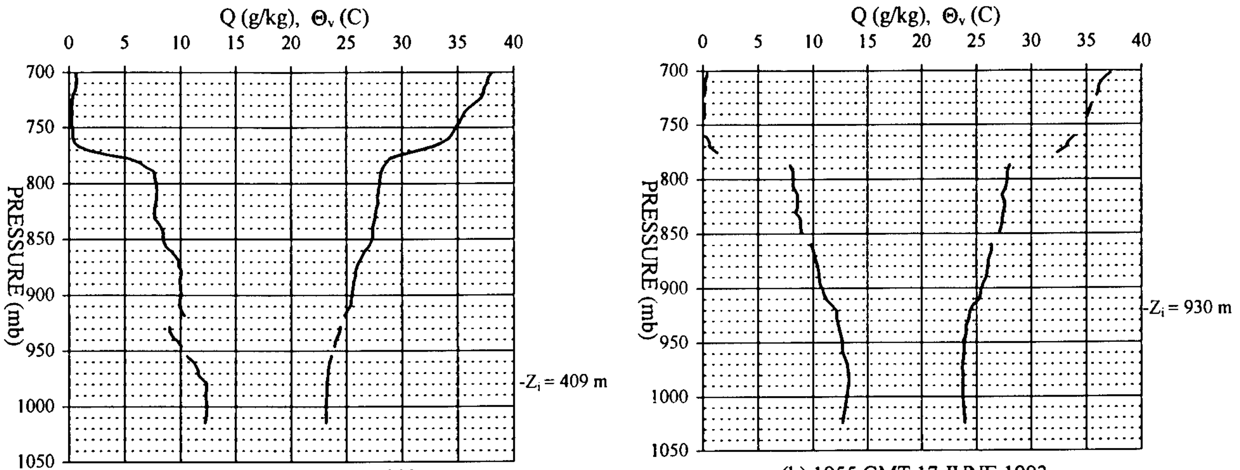

(a) 1517 GMT 17 JUNE 1993; 35.79 N, 74.23 W

(b) 1955 GMT 17 JUNE 1993; 35.72 N, 74.10 W

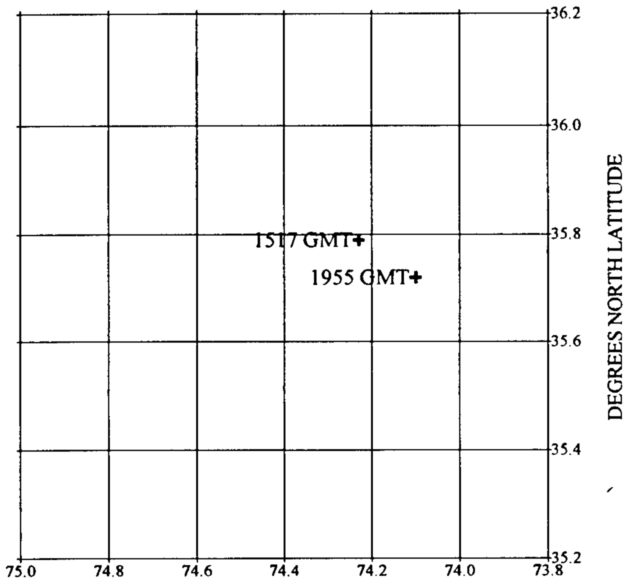

(c) DEGREES WEST LONGITUDE

FIG. 7. Vertical profiles of mixing ratio Q (g kg^{-1}) and virtual potential temperature θ_v (°C) along with the resulting estimates of z_i (m) from two radiosondes launched aboard the R/V *Columbus Iselin* into convective MABLs during 17 June 1993 from (a) 35.79°N, 74.23°W at 1517 UTC and (b) 35.72°N, 74.10°W at 1955 UTC. A corresponding map of the two radiosonde launch locations within the imaged area is found in (c).

horizontal wavelength of a BLSE is a function of z_i. Mixed-layer similarity relationships for BLSE aspect ratio have therefore been developed and applied to universally scale BLSE wavelength to z_i (e.g., Miura 1986).

Young (1988) shows that the dominant horizontal wavelength of BLSEs in the convective boundary layer is about $1.5z_i$. This aspect ratio value of 1.5 matches well with other studies. Recall from section 1a that Kaimal et al. (1976) show that the peak wavelength of horizontal velocity spectra does not vary with height from z_i right down to the surface and is also approximately $1.5z_i$. Recall also the arguments of section 1a linking mottles to the footprints of BLSEs, which lead us to believe that the wavelength of the mottles as seen by SAR can be equated to BLSE wavelength. This hypothesized relationship will now be substantiated through a comparison of the ratio of mottle wavelength to z_i versus the similarity theory value for the ratio of BLSE wavelength to z_i.

Following our logic given in section 1a, a mottle wavelength is taken to be the distance from the up-mean-wind backscatter edge of one bright mottle to the corresponding edge of the next down-mean-wind bright mottle. A sample of 50 mottle wavelengths were measured from the in situ data containing region of Fig. 1. The measurements were made by hand using a divider. The average measured wavelength of a mottle is 1.33 km with a standard deviation of 0.5 km.

To evaluate z_i in the mottled portion of the in situ data-containing region, radiosonde profiles are employed. Figures 7a,b show the two radiosonde profiles of mixing ratio Q (g kg^{-1}) and virtual potential temperature θ_v (°C), along with the resulting estimates of z_i (m). Figure 7c shows the corresponding radiosonde launch locations from the R/V *Columbus Iselin* within the imaged area. The average z_i taken from the two soundings is 670 m.

Therefore, the average mottle aspect ratio (mottle wavelength divided by z_i) seen in the present research is 1.98 plus or minus 0.5. This value compares well with the previously mentioned studies of Kaimal et al. (1976) and Young (1988) for the BLSE aspect ratio. Thus, it appears that the average wavelength of the mottles does indeed approximate the average wavelength of the corresponding BLSEs.

Note also that in Fig. 1 the scale of the BLSE-induced mottles increases to the south and east of the GSNW. Given the above aspect ratio argument, this scale gradient would lead one to believe that z_i also increases to the south and east of the GSNW. The soundings in Figs. 7a,b support this SAR-based diagnosis. CMABL depth does indeed increase to the south and east of the GSNW. This relationship between the geographical trends in z_i and mottle wavelength lends further credence to our hypothesis that the mottled backscatter pattern does result from BLSEs that scale with z_i.

The above given relationship between mottle wavelength, BLSE wavelength, and z_i also helps explain why no mottles are seen in one portion of the in situ data containing the CMABL regime of Fig. 1. This portion lies directly adjacent to the GSNW near its southwestern-most extent in Fig. 1. Presumably, z_i in this marginal area is not deep enough to support BLSEs capable of reaching the elevation necessary to mix down momentum of enough magnitude to cause SAR-detectable sea surface roughness patterns (as discussed in section 1a).

Given all the above, we feel that mottle wavelengths do indeed correspond to BLSE wavelengths. Thus, for operational analyses, the above given SAR similarity procedure could be reversed to obtain an estimate of z_i from SAR imagery using this value of the mottle aspect ratio. Future research will include more sophisticated spectral methods for obtaining estimates of mottle wavelength and, thus, z_i.

4. Conclusions

Sea surface manifestations of CMABL cellular convection are evident on the *ERS-1* SAR image seen in Fig. 1. In the presence of fair synoptic-scale weather conditions, CMASL winds flowing out of CDs and into CUs modulate air–sea momentum flux patterns that in turn force SAR-detectable roughness patterns in the sea surface wave field. These kilometer-scale modulations of the capillary sea surface wave state appear as a characteristic mottled backscatter pattern as demonstrated by its detection in numerous other SAR studies of the sea surface (e.g., Gerling 1986; Beal et al. 1994; Trokhimovsky et al. 1994; Nilsson and Tildesley 1995). These previous observations combined with what has been presented in the present research demonstrate the characteristic nature of mottles on SAR imagery of the sea surface, thereby lending credence to the concept of SAR similarity.

In contrast, a cool sea surface beneath a statically stable MABL is denoted by a marbled backscatter pattern on our SAR image. The marbling is most likely associated with nearly calm surface winds in the statically stable MABL and the presence of sea surface surfactant slicks (Najjar 1992; Huhnerfuss et al. 1994, and Nilsson and Tildesley 1995).

The occurrence and nonoccurrence of the characteristic, SAR-similar, mottled backscatter pattern on SAR imagery of the sea surface allows one to infer the presence of the CMABL and BLSE circulation type. Moreover, CMABL depth can be related to the observed mottle wavelength using mixed-layer similarity theory for BLSE aspect ratio. These results can be applied to the nowcasting of oceanic fronts and stability-related radar ducting phenomena and should be of interest to the air–sea interaction research community (Sweet et al. 1981; Wai and Stage 1989; Doyle and Warner 1990; Sublette and Young 1994).

Future research will include spectral and textural classification of SAR imagery, along with detailed statistical ground truthing, in order to obtain quantitative descriptions of sea surface stress patterns and the CMASL wind field, induced by differing scales of convection as seen by SAR. In addition, initial comparisons of the BLSE-induced SAR backscatter pattern to sea surface stress patterns derived from a nonlinear dynamical model (Shirer et al. 1995) are heartening. Close collaboration between the image analysis and model research will continue.

Acknowledgments. The authors would like to thank M. S. Sublette and J. E. Hare for their help with data acquisition. The authors would also like to acknowledge the European Space Agency for supplying the SAR image. The authors would finally like to thank the anonymous reviewers for their very helpful comments. The research reported in this work was funded by the Office of Naval Research under Grants N00014-90-J-4012 and N00014-92-J-1585.

REFERENCES

Alpers, W., and B. Brummer, 1994: Atmospheric boundary layer rolls observed by the synthetic aperture radar aboard the ERS-1 satellite. *J. Geophys. Res.*, **99**, 12 613–12 621.

Beal, R., V. Kudryavtsev, D. Thompson, S. Grodsky, D. Tilley, and V. Dulov, 1994: Large and small scale circulation signatures of the ERS-1 SAR over the Gulf Stream. *Proc. Second ERS-1 Symp.-Space at the Service of our Environment,* Hamburg, Germany, ESA SP-361, 547–552.

Brown, R. A., 1980: Longitudinal instabilities and secondary flows in the planetary boundary layer: A review. *Rev. Geophys. Space Phys.*, **18**, 683–697.

Deardorff, J. W., 1976: Discussion of 'Thermals over the sea and gull flight behavior' by A. H. Woodcock. *Bound.-Layer Meteor.*, **10**, 241–246.

Dorman, C. E., and E. Mollo-Christensen, 1973: Observation of the structure on moving gust patterns over a water surface ("cat's paws"). *J. Phys. Oceanogr.*, **3**, 120–132.

Doyle, J. D., and T. T. Warner, 1990: Mesoscale coastal processes during GALE IOP 2. *Mon. Wea. Rev.*, **118**, 283–308.

Ebert, E., 1987: A pattern recognition technique for distinguishing surface and cloud types in the polar regions. *J. Climate Appl. Meteor.*, **26**, 1412–1427.

Fairall, C. W., J. B. Edson, S. E. Larsen, and P. G. Mestayer, 1990: Inertial-dissipation air–sea flux measurements: A prototype system using realtime spectral computations. *J. Atmos. Oceanic Technol.*, **7**, 425–453.

Gerling, T. W., 1986: Structure of the surface wind field from the Seasat SAR. *J. Geophys. Res.*, **91**, 2308–2320.

Greenhut, G. K., and S. J. S. Khalsa, 1982: Updraft and downdraft events in the atmospheric boundary layer over the equatorial Pacific Ocean. *J. Atmos. Sci.*, **39**, 1803–1818.

Haack, T., and H. N. Shirer, 1992: Mixed convective-dynamic roll vortices and their effects on initial wind and temperature profiles. *J. Atmos. Sci.*, **49**, 1181–1201.

Hare, J. E., J. B. Edson, E. J. Bock, and C. W. Fairall, 1992: Progress on direct covariance measurements of air–sea fluxes from ships and buoys. Preprints, *10th Symp. on Turbulence and Diffusion*, Portland, OR, Amer. Meteor. Soc., 281–284.

Huhnerfuss, H., A. Gericke, W. Alpers, R. Theis, V. Wismann, and P. A. Lange, 1994: Classification of sea slicks by multifrequency radar techniques: New chemical insights and their geophysical implications. *J. Geophys. Res.*, **99**, 9835–9845.

Kaimal, J. C., J. C. Wyngaard, D. A. Haugen, O. R. Cote, Y. Izumi, S. J. Caughey, and C. J. Readings, 1976: Turbulence structure in the convective boundary layer. *J. Atmos. Sci.*, **33**, 2152–2169.

——, ——, Y. Izumi, and O. R. Cote, 1972: Spectral characteristics of surface-layer turbulence. *Quart. J. Roy. Meteor. Soc.*, **98**, 563–589.

Kandel, A., 1982: *Fuzzy Techniques in Pattern Recognition.* Wiley, 356 pp.

Key, J., 1990: Cloud cover analysis with arctic advanced very high resolution radiometer data. Part 2: Classification with spectral and textural measures. *J. Geophys. Res.*, **95**, 7661–7675.

Khalsa, S. J. S., and G. K. Greenhut, 1985: Conditional sampling of updrafts and downdrafts in the marine atmospheric boundary layer. *J. Atmos. Sci.*, **42**, 2550–2562.

LeMone, M. A., 1973: The structure and dynamics of horizontal roll vortices in the planetary boundary layer. *J. Atmos. Sci.*, **30**, 1077–1091.

Lenschow, D. H., and P. L. Stephens, 1980: The role of thermals in the convective boundary layer. *Bound.-Layer Meteor.*, **19**, 509–532.

Liu, W. T., K. B. Katsaros, and J. A. Businger, 1979: Bulk parameterization of air–sea exchanges of heat and water vapor including the molecular constraints at the interface. *J. Atmos. Sci.*, **36**, 1722–1735.

Miura, Y., 1986: Aspect ratios of longitudinal rolls and convection cells observed during cold air outbreaks. *J. Atmos. Sci.*, **43**, 26–39.

Najjar, R. G., 1992: Marine biogeochemistry. *Climate System Modeling*, K. E. Trenberth, Ed., Cambridge University Press, 241–283.

Nilsson, C. S., and P. C. Tildesley, 1995: Imaging of oceanic features by ERS 1 synthetic aperture radar. *J. Geophys. Res.*, **100**, 953–967.

Schumann, U., and C.-H. Moeng, 1991: Plume fluxes in clear and cloudy convective boundary layers. *J. Atmos. Sci.*, **48**, 1746–1757.

Shirer, H. N., L. V. Zuccarello, P. J. Bromfield, B. A. Lambert, and R. Wells, 1995: Sea surface stress variability caused by kilometer-scale boundary layer circulations. Preprints, *11th Symp. on Boundary Layers and Turbulence*, Charlotte, NC, Amer. Meteor. Soc., 76–79.

Sikora, T. D., and G. S. Young, 1993: Observations of planview flux patterns within convective structures of the marine atmospheric surface layer. *Bound.-Layer Meteor.*, **65**, 273–288.

——, and ——, 1994: Observations and applications of the horizontal perturbation wind field within convective structures of the marine atmospheric surface layer. *Bound.-Layer Meteor.*, **68**, 419–426.

Stull, R. B., 1988: *An Introduction to Boundary Layer Meteorology.* Kluwer Academic Publishers, 666 pp.

Sublette, M. S., and G. S. Young, 1994: An analysis of the Gulf Stream atmospheric front during the summer season. Preprints, *Sixth Conf. on Mesoscale Processes*, Portland, OR, Amer. Meteor. Soc., 258–261.

Swain, P. H., S. B. Vardeman, and J. C. Tilton, 1981: Contextual classification of multispectral image data. *Pattern Recognit.*, **13**, 429–441.

Sweet, W., R. Fett, J. Kerling, and P. La Violette, 1981: Air–sea interaction effects in the lower troposphere across the north wall of the Gulf Stream. *Mon. Wea. Rev.*, **109**, 1042–1052.

Thompson, D. R., J. C. Graber, and R. E. Carande, 1994: Measurements of ocean currents with SAR interferometry and HF radar. *Int. Geoscience and Remote Sensing Symp. 94*, Pasadena, CA, IEEE 2020–2022.

Trokhimovsky, Y. G., V. Yakovlev, R. D. Chapman, and D. R. Thompson, 1994: The coherence of wind and radar data obtained during the joint US–Russia Internal Wave Experiment. *Int. Geoscience and Remote Sensing Symp. 94*, Pasadena, CA, IEEE 802–804.

Wai, M. M.-K., and S. A. Stage, 1989: Dynamic analysis of marine atmospheric boundary layer structure near the Gulf Stream oceanic front. *Quart. J. Roy. Meteor. Soc.*, **115**, 29–44.

Watts, A., 1987: *Wind and Sailing Boats, the Structure and Behavior of the Wind as it Affects Sailing Craft.* David and Charles, 224 pp.

Wilczak, J. M., 1984: Large-scale eddies in the unstably stratified atmospheric surface layer. Part I: Velocity and temperature structure. *J. Atmos. Sci.*, **41**, 3537–3550.

Woodcock, A. H., 1975: Thermals over the sea and gull flight behavior. *Bound.-Layer Meteor.*, **9**, 63–68.

Young, G. S., 1987: Mixed layer spectra from aircraft measurements. *J. Atmos. Sci.*, **44**, 1251–1256.

——, 1988: Turbulence structure of the convective boundary layer. Part II: Phoenix 78 aircraft observations of thermals and their environment. *J. Atmos. Sci.*, **45**, 727–735.

JOURNAL OF GEOPHYSICAL RESEARCH, VOL. 102, NO. C8, PAGES 18,737–18,748, AUGUST 15, 1997

On the accuracy of HF radar surface current measurements: Intercomparisons with ship-based sensors

R. D. Chapman,[1] L. K. Shay,[2] H. C. Graber,[2] J. B. Edson,[3] A. Karachintsev,[3]
C. L. Trump,[4] and D. B. Ross[5]

Abstract. High-frequency (HF) radar systems can provide periodic, two-dimensional, vector current estimates over an area approaching 1000 km^2. As the use of these HF systems has gained wider acceptance, a number of attempts have been made to estimate the accuracy of such systems. However, comparisons of HF radar current estimates with in situ sensors are difficult to interpret since HF systems measure currents averaged over an area of ~1 km^2 and to a depth of only ~50 cm while in situ sensors measure currents at a point and somewhat greater depths (~1 to 10 m). Previous studies of the accuracy of HF radar technology have thus attributed the differences observed between HF radar and in situ sensors to an unknown combination of vertical shear, horizontal inhomogeneity, in situ instrument errors, and HF radar system errors. This study examines the accuracy of HF radar current measurements using data from the 1993 High Resolution Remote Sensing Experiment, conducted off Cape Hatteras, North Carolina. Data from four shipborne in situ current meters are compared with data from an Ocean Surface Current Radar (OSCR), a commercial current-measuring radar. We attempt to discern the predominant sources of error in these data by using multiple simultaneous measurements from different sensors and by examining the variation of observed current differences as a function of location. The results suggest an upper bound on the accuracy of the OSCR-derived radial currents of 7 to 8 cm/s.

1. Introduction

Near-surface ocean currents play a variety of roles in coastal environments. Physically, wind stress is imparted through an upper surface boundary layer. These upper layer stresses play an important role in the development and maintenance of the mixed layer. Biologically, near-surface currents distribute and disperse both plankton and fish eggs. Ecologically, many pollutants, such as oil, are surface borne. The dispersion of such pollutants depends critically on the near-surface current structure. Thus, from multiple viewpoints, the measurement of near-surface currents in the coastal environment is an important problem.

Unfortunately, conventional methods for measuring near-surface currents (depths ~1 m) are somewhat problematic. While careful design of surface drifters can minimize problems due to windage and wave interaction, single drifters are limited and uncontrollable in their spatial and temporal coverage, especially in convergent and divergent flow regimes. Multiple drifters can be prohibitively expensive when used in sufficient quantities to adequately characterize the current within a large region over a significant period of time. Moored instruments can be used to obtain long time series, but they usually suffer from motions of the moored body. Furthermore, the instruments are typically suspended below a surface float, which physically restricts the minimum depth of the current measurement to a few meters. Currents measured from ship-mounted acoustic Doppler current profilers (ADCPs) can be useful, but the first measurement bins are necessarily below the draft of the ship and ship time is expensive. For these reasons, a land-based method for continuously measuring surface currents in the coastal region has considerable merit.

The measurement of near-surface ocean currents using electromagnetic backscatter measured from a high-frequency radar was first demonstrated over 20 years ago [*Stewart and Joy*, 1974; *Barrick et al.*, 1974]. (Generally, the term high-frequency, or HF, refers to systems with carrier frequencies between 3 and 30 MHz.) This technique, based on the results of *Crombie* [1972], utilizes the fact that HF backscatter from the ocean at near-grazing angles is predominantly due to Bragg scattering. Thus the Doppler spectrum of the HF radar return contains sharp peaks associated with those surface gravity waves with a wavelength of half of the radar wavelength that are either approaching toward, or receding from, the radar site [*Crombie*, 1955]. The frequency of these Doppler peaks reflects the phase velocity of the scattering waves. By subtracting the known phase velocity of the scattering wave in the absence of current, $c_p = \sqrt{g/k}$, from the measured phase velocity, an estimate of the component of the surface current in the look direction of the radar can be obtained. Two or more stations, viewing a particular measurement point from different directions, can then be used to estimate surface current vectors.

Several practical radar systems for measuring ocean currents in the near-coastal environment have been developed and commercialized. At least two such systems are currently available: the

---

[1] Applied Physics Laboratory, Johns Hopkins University, Laurel, Maryland
[2] Rosenstiel School of Marine and Atmospheric Sciences, University of Miami, Miami, Florida
[3] Woods Hole Oceanographic Institution, Woods Hole, Massachussetts
[4] Naval Research Laboratory, Washington, D. C.
[5] Ivy Inc., Miami, Florida

Paper number 97JC00049
0148-0227/97/97JC-00049$09.00

Coastal Ocean Dynamics Application Radar (CODAR), manufactured by CODAR Ocean Sensors, Ltd., and the Ocean Surface Current Radar (OSCR), manufactured by Marconi, Inc. While we utilize an OSCR system, owned and operated by the University of Miami, for this study, we believe that the results presented here would, in principle, be the same for a CODAR system. The two systems differ in beam-forming technology but rely on fundamentally similar physics and Doppler-processing algorithms for their operation. An informative side-by-side comparison of an OSCR and several CODAR systems has just been published by *Fernandez and Paduan* [1996].

These commercial systems are limited to near-coastal environments because of their design and the nature of ground wave HF radio propagation. (Attempts have been made to operate OSCR from both an anchored and a moving ship [cf. *Skop et al.*, 1994; *Peters and Skop*, 1995].) Most HF communication systems rely on reflections off the ionosphere to achieve over-the-horizon operation. Unfortunately, motions in the ionosphere, which are responsible for the fading typically observed in HF communications, act to blur the Doppler signature of the Bragg scatterers. While some encouraging progress has been made on long-range current estimates using HF radars [*Trizna*, 1982; *Georges and Harlan*, 1995], the most common HF current-measuring systems utilize ground wave propagation to eliminate ionospheric effects. Losses in ground wave propagation subsequently limit CODAR and OSCR systems to effective ranges of less than 100 km, although we note that additional power could be combined with higher gain antennas to extend this range to several hundred kilometers.

Since the development of HF radar for current measurement, there have been a number of experiments to evaluate the accuracy of this technology. The first experiments [*Stewart and Joy*, 1974; *Barrick et al.*, 1977; *Frisch and Weber*, 1980] compared HF radar estimates of current to those derived from drifting buoys. These studies reported differences between the radar- and drifter-derived currents of 15 to 27 cm/s. *Paduan and Rosenfield* [1996] present a more recent study using the same technique, reporting 13 cm/s rms differences in current magnitude. Later studies, comparing HF data with current measurements from moorings or bottom-mounted ADCPs [*Holbrook and Frisch*, 1981; *Leise*, 1984; *Porter et al.*, 1986; *Matthews et al.*, 1988], reported differences ranging from 9 to 17 cm/s. While the level of agreement found in these studies is encouraging, all acknowledged the difficulties in comparing HF radar-derived currents, which are area-averaged estimates made at the surface, with in situ measurements, which are essentially point measurements made at some finite depth. *Prandle* [1991] includes an overview of a series of studies comparing tidal ellipses determined from HF radar and conventional current meters. Using HF-radar-derived surface currents from the High Resolution Remote Sensing Experiment, *Shay et al.* [1995] found rms differences of 12–15 cm/s between surface and moored subsurface current measurements. This study focused on understanding these differences within the context of bulk vertical current shears of about 1–2 cm/s per meter by decomposing the observations into various frequency bands. More recently, *Paduan and Rosenfield* [1996] reported on extensive intercomparisons of HF radar data with in situ sensors in Monterey Bay, including a rather complete discussion of the difficulties and uncertainties in such a comparison.

This study is an attempt to better estimate the accuracy of current estimates made by an HF radar system. Our approach is to compare shipborne surface current measurements to those obtained by HF radar over the 2 weeks of the High Resolution Remote Sensing Experiment. We utilize two techniques in an attempt to apportion the observed current estimate differences to physical differences and instrument errors. The first technique involves the simultaneous comparison of estimates derived from multiple instruments, including the HF radar. We hoped that the relative magnitude of the observed differences would lead to an apportionment of the errors. The second technique examines the dependence of the observed current estimate differences with location. By combining the data with a simple model of the spatial dependence of errors in the HF radar system, we estimate upper bounds on the accuracy of that system.

2. Data Sources

The data used in this study were obtained during the High Resolution Remote Sensing Experiment [*Herr et al.*, 1991]. This experiment, jointly supported by the Office of Naval Research and the Naval Research Laboratory, was designed to investigate the detailed processes involved in radar imaging of submesoscale features. The experiment took place 10 to 50 km offshore from Cape Hatteras, North Carolina, from June 10 through June 26, 1993. The reader is referred to *Shay et al.* [1995] for a description of the oceanography of the region during the period of the experiment.

The experiment was supported by a wide variety of research platforms, including two research vessels fielding in situ sensors, several aircraft with real and synthetic aperture radars, the ERS-1 satellite, and a land-based Ocean Surface Current Radar (OSCR). Both of the research vessels, USNS *Bartlett* and R/V *Columbus Iselin*, also deployed small towed platforms containing current sensors as well as other instrumentation. Our study compares data from four separate current sensors on the research vessels and towed platforms to those obtained from the OSCR in order to evaluate the accuracy and limitations of OSCR. Each of the systems involved in the comparison is described in the paragraphs below.

2.1. OSCR

OSCR is a dual-site pulse-Doppler radar operating at a frequency of 25.4 MHz. The transmit antenna for this system is a four-element Yagi configuration with a front-to-back power ratio of 6 dB and a 90° wide beam pattern. A phased-array receiving antenna, with a beam width of approximately 6°, is used to azimuthally scan the ocean region illuminated by the transmitted beam. The radar estimates near-surface currents within each range and azimuth cell by identifying and tracking frequency shifts in the peaks of the Doppler spectra of the ocean backscatter corresponding to the advection of the Bragg wave. Since an individual station is only sensitive to radial Doppler velocities, two separate stations are used in the system to obtain vector current estimates. During the High Resolution Remote Sensing Experiment the two stations of the OSCR system were deployed on the shore in the towns of Avon and Waves, North Carolina. These two sites were separated by a distance of 24 km [*Shay et al.*, 1995].

While intermediate data products were recorded from the OSCR system, the final data products, used in this study, were maps of surface current estimates. These maps display estimates of the near-surface current everywhere within a circle of about 35-km diameter centered about 25 km off shore and with a mean horizontal resolution of approximately 1.2 km. Such maps were produced every 20 min during nearly the entire period of the experiment. One such map is shown in Figure 1.

Several aspects of the OSCR system, some of which are important for this analysis, are worth noting.

1. In contrast to the in situ sensors, which essentially measure currents at a point, the OSCR current estimates are based on averages taken over an area of between 2.5 and 5.6 km^2. More precisely,

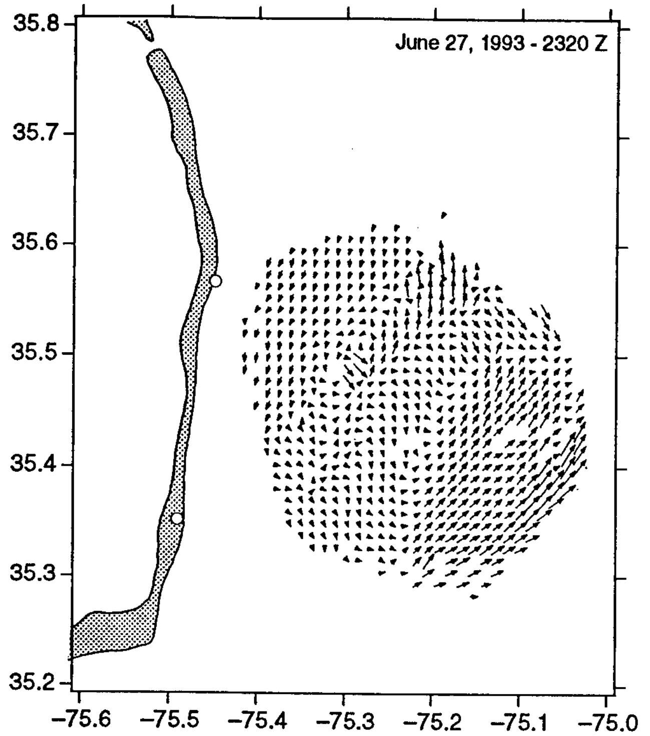

Figure 1. Typical surface current map produced by OSCR. During the course of the experiment, over 1100 of these maps were produced.

the OSCR current estimates are based upon all of the spectral information obtained within the resolved area. Horizontal variations in the current field with scale lengths less than 1 km will result in broadened or multiple Doppler spectral peaks. The software must then choose between valid Bragg pairs. Thus there will be times when the OSCR-estimated current, though valid, will differ from an in situ measurement. Due to the complexity of the current regime off Cape Hatteras, these averaging effects may contribute substantially to the observed rms differences.

2. The wavelength of the Bragg scatterers for OSCR is 5.9 m. As such, OSCR responds to surface currents integrated over approximately the upper 0.5 m (= $\lambda_r/8\pi$, where λ_r is the radar wavelength) of the water column [*Stewart and Joy*, 1974]. The in situ data used in this study were obtained at depths of 1 to 10 m. Vertical inhomogeneity in the near-surface current over these scales contributes to differences in the current estimates.

3. The OSCR system utilizes simple criteria to eliminate bad data. These criteria are based on the strength of the backscatter and the form of the resulting Doppler spectra. In particular, current estimates are not recorded for those points and times where neither the approaching nor the receding Bragg peaks are greater than 6 dB above the background noise floor. Thus the current maps produced by OSCR have some gaps in them. This explains some of the holes in the coverage shown in Figure 1. These gaps are not common, representing at most a few percent of the data within the interior of the measurement domain.

4. The data quality criteria used by OSCR are not perfect, and some current estimates that are wildly erroneous can still be found in the data. Such wild points were observed to occur less than 1% of the time within the data.

5. To avoid interference with each other, the OSCR master and slave sites are not operated simultaneously but are instead operated sequentially. The sequence begins with the master site operating for a period of 5 min. The master site then goes silent and the slave site operates for 5 min. Both sites are then silent for the remainder of the 20-min cycle during which time data are exchanged between the sites and processing is performed. This sequencing of measurements means that the two radial measurements used for each vector estimate are not taken simultaneously. Errors due to this temporal undersampling are unlikely, as this would require a feature with a phase velocity of the order of 4 m/s (= 1.2 km/5 min).

6. The phase velocity of the Bragg waves is altered in shallow water, which directly affects the surface current estimates. Fortunately, at the wavelength at which OSCR operates, this effect only becomes significant for water depths less than 3 m, and no depths this shallow were encountered in this study.

7. The expected precision of a radial current estimate made by OSCR is 2.2 cm/s. This figure is based on the length of the analysis records for the specific setup utilized during this experiment and represents a limit in the system's ability to locate a particular Doppler peak.

2.2. R/V *Columbus Iselin*

R/V *Columbus Iselin* was equipped with a hull-mounted 300-kHz narrowband ADCP. This ADCP produced current estimates starting at a depth of 4.6 m. In the shallower waters, from the center of the OSCR measurement domain to near shore, bottom tracking and the ship's gyrocompass were used to estimate true near-surface currents. In less than 5% of the data, the bottom track signal became too weak to use, so the ADCP and gyrocompass data were combined with data from the ship's standard Global Positioning System (GPS) to estimate currents.

In bottom track mode, the theoretical standard deviation for horizontal current from a single ping from this ADCP is 5.7 cm/s (10-m bin, ±30° beam angles). With a ping every 1.5 s, 20 min of averaging should reduce this standard deviation to 2 mm/s. Unfortunately, this calculation fails to take into account longer-term biases caused by flow distortion about the vessel, the effect of bubbles entrained near the sensor head, compass errors, and variations in flow during the averaging interval. These other sources of errors, which are difficult to estimate, are likely to dominate in our measurements. Experience suggests though that the combined errors can be expected to be on the order of 1 to 5 cm/s. The same considerations hold true for the other ADCPs used in this study.

2.3. LADAS

LADAS was a towed catamaran system developed by Erik Bock at the Woods Hole Oceanographic Institution for measuring the structure of centimeter-scale surface waves and the modulations of these short waves by long waves. (We use the past tense here since LADAS was lost at sea during a recent experiment on the West Coast.) Its primary instruments were a scanning laser slope gauge [*Bock and Hara*, 1995], a suite of meteorological instruments, a differential GPS (DGPS) receiver, a six-degree-of-freedom, strapdown motion sensing package [*Edson et al.*, 1996], and a three-axis ultrasonic current meter. Data from this current meter and the differential GPS (DGPS) receiver were utilized in this study.

The three-axis ultrasonic current meter was a UCM 40 Mk II, manufactured by NE Sensortec, Norway. This instrument measures currents over a set of orthogonal 10-cm paths by measuring the time of flight of a series of high-frequency acoustic pulses. The instrument has a resolution of 1 mm/s and an accuracy of 3% of the measured value ± 5 mm/s with an integration period of 1 s. The instrument utilizes an internal three-axis flux gate compass and a two-axis tilt sensor to compensate the data for the instrument orientation. The system also includes built-in temperature, conductivity, and pressure sensors. This instrument was mounted forward on the body of the catamaran, between the two hulls. In this mounting position the sensors were outside the wakes of the pontoons when the catamaran was being towed forward. The current sensors were located at a mean depth of 1.0 m.

The data from the LADAS UCM were combined with the differential GPS data to estimate true currents. The predominant errors in this combined data set are likely due to biases and noise introduced by pitch and rolling motions of the catamaran in the wave field. While to lowest order, these high-frequency motions should average out, they may introduce biases into the estimate since the depth of the UCM measurements varied coherently with the surface waves as the platform pitched up and down.

2.4. USNS *Bartlett*

USNS *Bartlett* was equipped with a 300-kHz hull-mounted, narrowband ADCP. In the shallower waters, throughout most of the OSCR measurement domain, bottom tracking and the ship's gyrocompass were used to estimate true currents. In approximately 3% of the data the bottom track signal became too weak to use, so the ADCP and gyrocompass data were combined with data from a real-time differential GPS system to estimate currents.

2.5. TOAD

The Towed Acoustic Doppler (TOAD) platform is a small tube with stabilizing fins that is designed to hold an ADCP as it is towed on the surface, outboard of a vessel [*Marmorino and Trump*, 1996]. This system, developed by the Naval Research Laboratory, was designed to keep the ADCP away from the influences of the ship while still providing a relatively stable platform for making current measurements. During the High Resolution Remote Sensing Experiment, a 600-kHz broadband ADCP was deployed from TOAD. The TOAD platform was deployed periodically from USNS *Bartlett* throughout the experiment to track near-surface current features.

Because of its small size, the TOAD platform experiences more transient accelerations than the towing ship. These accelerations adversely affected the onboard attitude sensors, making the absolute water velocities measured from TOAD noisier than those from the shipboard system. To minimize this problem the shipboard data were merged into the TOAD data by offsetting the TOAD data so that the average absolute water velocity between 10 and 20 m measured by TOAD was identical to the value measured by the shipboard system. The result of this merging process is that the absolute water velocities reported by both systems between 10 and 20 m will be virtually identical. The advantage of the TOAD data lies in its smaller bins (0.5 m versus 1.0 m) that measure closer to the surface (1.6 m versus 8.8 m) than the *Bartlett* ADCP.

3. Methodology

This study compares the OSCR current maps with the near-surface current measurements made from three separate ADCPs (*Iselin*, *Bartlett*, and TOAD) as well as data from the three-axis current meter mounted at 1-m depth on LADAS. The methodology used to compare these data is relatively straightforward. Data from the in situ sensors were combined with the bottom track velocities, or the differential GPS navigation data where the depth of the water precluded bottom tracking, and platform orientation data to obtain estimates of the Earth-fixed currents at the platform location. These time series were reduced to a sample every 20 min by averaging those values corresponding to each OSCR observation period. We estimate that the errors in alignment of these data-averaging periods are less than a few seconds, since all of the data streams included timing information traceable to GPS time. An equivalent series of surface current data were then constructed by selecting the OSCR data closest to the in situ data in time and space.

Note that while the data were in the form of a time series, this time series was obtained at the time-varying position of the platforms as they moved about the experimental area. Thus conventional time series analyses cannot be usefully applied to these data. Instead, we restrict ourselves to nontemporal statistical comparisons.

Our initial analysis is based on simple scatterplots between pairs of related estimates of the north and east components of the surface velocity. The rms difference in the velocity estimates, which we refer to as σ_d, is used to characterize the comparisons. This is the most commonly used statistic in previous intercomparison studies, making our results directly comparable to those studies. The reader is cautioned though not to attribute all of the rms difference to errors in the HF radar current estimate.

The reader should note that throughout this paper we are careful to distinguish between the terms "differences" and "errors." In our usage, subtracting two current estimates results in a current estimate "difference." This current estimate difference is likely due to a combination of differences in the quantity measured due to physical processes and to noise in the instruments themselves. We refer to noise within an instrument, causing the instrument to read other than a true value, as an "error." Thus we are trying to estimate HF radar errors by studying observed differences.

4. Results and Discussion

Before presenting the results, it is instructive to consider the possible causes of differences in surface current estimates made by the OSCR system, an ADCP, and the ultrasonic current meter.

The first possible cause is the comparison of dissimilar quantities. The OSCR measures surface currents averaged over a 1.5-km^2 area and to an effective depth of about 50 cm. The ADCPs measure over an area of at most a few square meters in the bins nearest the surface and measure at an effective depth of several meters, depending on the system and how it is mounted. The ultrasonic current meter measures over a scale length of 10 cm at a depth of 1 m. One should not expect such measurements to agree for a variety of physical reasons. For example, differences could be due to horizontal inhomogeneity caused by local eddies and fronts. Likewise, vertical shears arising from the near-surface boundary layers or internal waves can also lead to differences [*Shay et al.*, 1995]. Here, and elsewhere throughout the paper, by vertical shear we mean those bulk vertical shears remaining after 20 min of averaging.

The second possibility is temporal or spatial misalignments of the measurement data sets. Any misalignments of the data sets, either temporally or spatially, will cause a decorrelation of the results. Given the relatively high accuracy of the data set timing, we do not expect temporal decorrelation to be a problem. Likewise we believe that the spatial mismatch was also small. The in situ sensors utilized differential or standard GPS data for spatial positioning, systems with accuracies of better than 100 m. The other possible uncertainty was the positioning of the OSCR grid locations. In the radial direction, these positions are determined quite accurately by the system range gate timing. In the azimuthal direction, these positions are determined by the physical and electrical alignment of the OSCR phased-array antenna. The estimated physical accuracy of the antenna alignment was less than 0.5°, which would bound the errors in cell positioning to less than 1/3 of the cell size.

Electrical misalignment of the phased array, which could take the form of increased sidelobes in the antenna pattern, is a concern with this type of system. No significant correlation was observed between antenna look angle and radial current estimates differences made from each OSCR site and from the *Bartlett* and *Iselin* ADCPs. This suggests that phase misalignments of the antenna are at least uniformly varying across the antenna aperture, making substantial errors due to this source unlikely.

A third possibility is systematic biases or noise in the OSCR data. Any biases or noise within the estimates derived by OSCR will contribute to the differences in the comparison with other instruments. These are the errors we are trying to evaluate.

The fourth possibility is systematic biases or noise in the in situ data. Likewise, any biases or noise in the in situ data will also contribute to differences in the comparisons. Such errors could arise from errors in the sensors themselves or the platform motion and orientation corrections. Hence these data depend on the accuracies of the current sensors, bottom-tracking algorithms, or DGPS velocity estimates, as well as compass sensors.

An appreciation for the possible sources of differences led to our general approach of comparing these data streams. In this approach, to the extent that we could, we utilized multiple data comparisons in an attempt to apportion the observed differences to one of the above causes. This approach is explained in detail below.

4.1. OSCR Versus *Columbus Iselin*

Figure 2 presents the comparisons between OSCR and the *Iselin* ADCP data. The north and east current component comparisons are shown in the upper panels (Figures 2a, 2b, and 2c) and lower panels (Figures 2d, 2e, and 2f), respectively. The leftmost two panels (Figures 2a and 2d) compare OSCR and the shallowest ADCP bin at 4.6-m depth. The middle two panels (Figures 2b and 2e) compare OSCR and the next deepest ADCP bin at 5.6-m depth. The rightmost two panels (Figures 2c and 2f) compare the data from the two adjacent ADCP bins. The dotted line, which has been placed on each panel for visual comparisons only, indicates the line where the two current estimates are equal. This line does not represent a least squares fit to these data. The rms difference of each of the comparisons, σ_d, is given in the upper left corner of each panel.

In Figure 2a at least two erroneous points in the OSCR estimates are evident. These wild points can easily be associated with errors in the OSCR estimates since the OSCR-estimated current component value of 90 cm/s is beyond any others observed by either instrument. A third wild point is evident, although its source is not so clear. Other than these three wild points, the remaining 401 points are nicely clustered about the line of equal velocity. The standard deviation of the difference is 14.8 cm/s for all 404 points. If these differences were drawn from a Gaussian distribution, the error bounds on this estimate of σ_d, to the 95% confidence level, are estimated to be ±1.0 cm/s.

Figure 2b shows a similar grouping of points about the equal velocity line, but with a slightly higher standard deviation of the difference of 15.1 cm/s. One point, which is not visible in this figure, has been excluded from the computation of σ_d in Figures 2b and 2c because the OSCR velocity estimate was greater than 1.5 m/s.

Given the error bars of ±1.0 cm/s at the 95% confidence level, the differences observed between the OSCR and ADCP data at 4.6-m and 5.6-m depth are on the border of statistical insignificance. At the same time, as should be expected, the agreement between the 4.6-m and 5.6-m ADCP bins (Figure 2c) is much better than the agreement between either ADCP bin and OSCR.

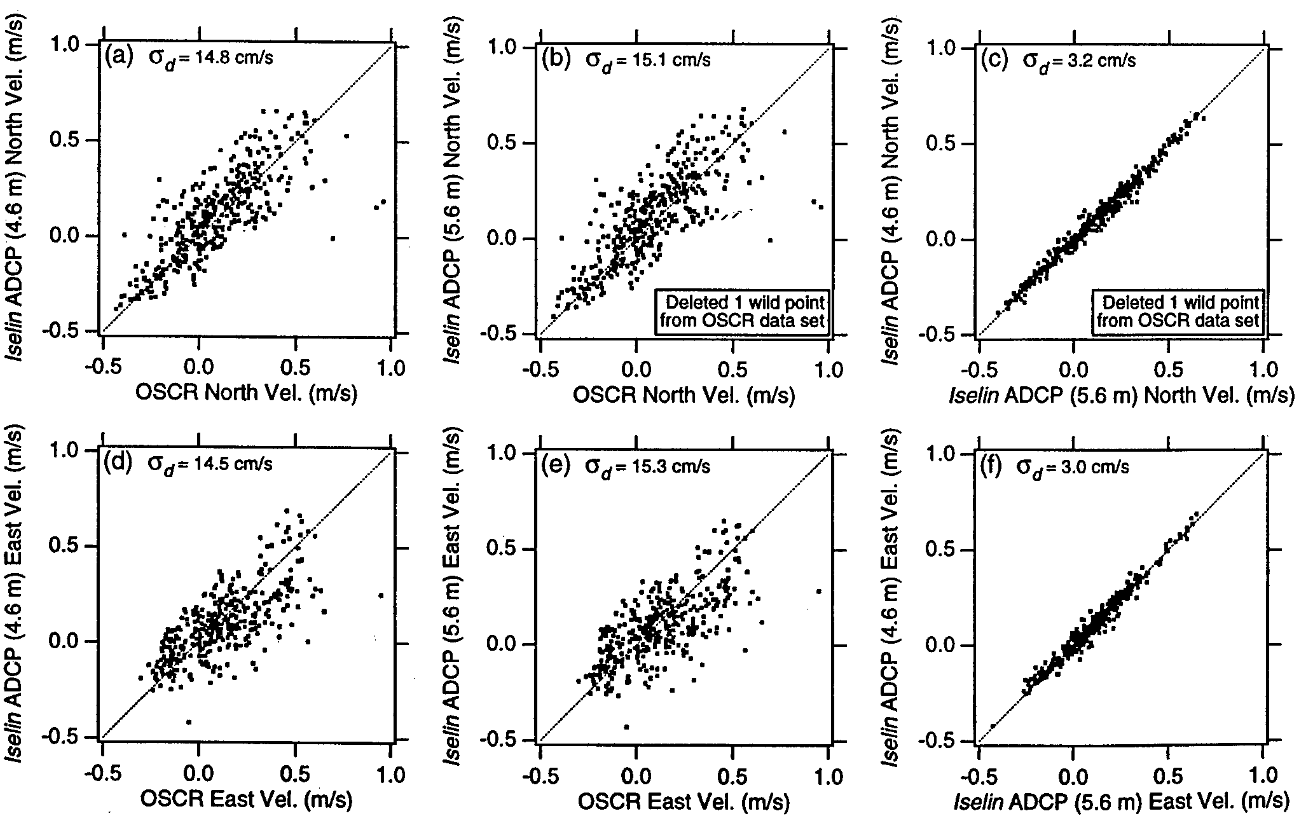

Figure 2. Comparisons of the surface current component estimates made from the *Iselin* ADCP and OSCR. The dotted line indicates the line of equal currents. It does not represent a fit to the data. The rms difference between the estimates, σ_d, is given in the upper left corner.

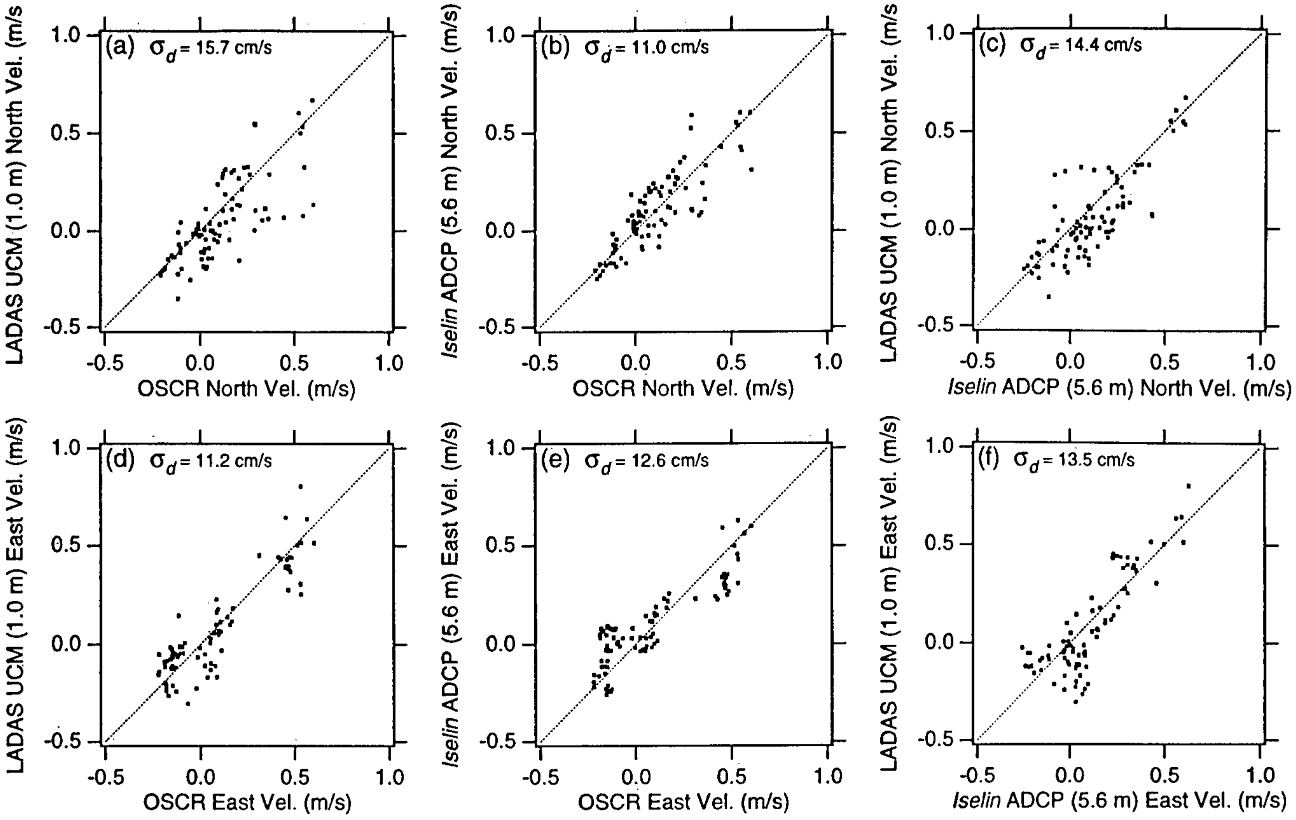

Figure 3. Comparisons of the surface current component estimates made from the LADAS UCM, *Iselin* ADCP, and OSCR.

4.2. OSCR Versus LADAS

Comparisons of the OSCR, UCM, and ADCP data from LADAS are shown in the six panels in Figure 3. While the total number of points is much smaller for these comparisons because of the limited amount of time that LADAS was deployed during the experiment, all of the comparisons show a similar trend about the line of equal current. The rms differences for these comparisons range from 11 to 16 cm/s.

The LADAS comparisons are particularly interesting due to the presence of three distinct types of sensors. If the differences in the OSCR comparisons were predominantly due to mean vertical shear, we would expect to find that the agreement between OSCR and the LADAS UCM would be substantially better than the agreement of either instrument with the deeper ADCP. This does not appear to be the case. If, on the other hand, the differences were predominantly due to the differences between point measurements and area-averaged measurements, we would expect that the agreement between the LADAS UCM and *Iselin* ADCP would be superior to either in situ sensor compared to OSCR. Again, this does not appear to be the case.

4.3. OSCR Versus USNS *Bartlett*

Figure 4 contains the data comparisons between OSCR and the *Bartlett* ADCP. Note that a single wild point, with a current estimate exceeding 1.5 m/s, was deleted from the OSCR north component data set prior to estimating the rms difference.

4.4. OSCR Versus TOAD

Our final set of data, containing comparisons between OSCR and the TOAD ADCP, is shown in Figure 5. Again, the comparisons show good agreement between the data sets, with rms differences ranging from 9 to 16 cm/s.

4.5. Comparison Summary

The results of these comparisons are summarized in Table 1. The second and third columns present the number of points used in the comparison and the linear correlation coefficient for those comparisons. The rms differences for each comparison are given in the fourth column, along with error bounds for these estimates. These bounds were computed at the 95% confidence level, assuming that the component differences are Gaussian-distributed random variables. The estimates of the variance from a given sample size are thus assumed to be χ^2 distributed, and the error bounds are easily computed. The last two columns contain depth corrections as described below.

Several interesting observations can be made from this data summary.

1. All of the comparisons with OSCR show roughly comparable differences of between 9 and 16 cm/s. This places an absolute upper bound on the errors of the OSCR estimates, which is comparable to that reported in previous studies [*Shay et al.*, 1995].

2. There is a statistically significant difference between the north and east rms differences for only two cases, the LADAS UCM and the TOAD 2-m ADCP. These are also the two shallowest instruments. More will be made of this point in the following section.

3. The lowest correlation coefficients are associated with the comparisons of OSCR with the deepest instruments. This suggests that near-surface vertical shear is an important, but not dominant, component in the differences observed between OSCR and the in situ sensors.

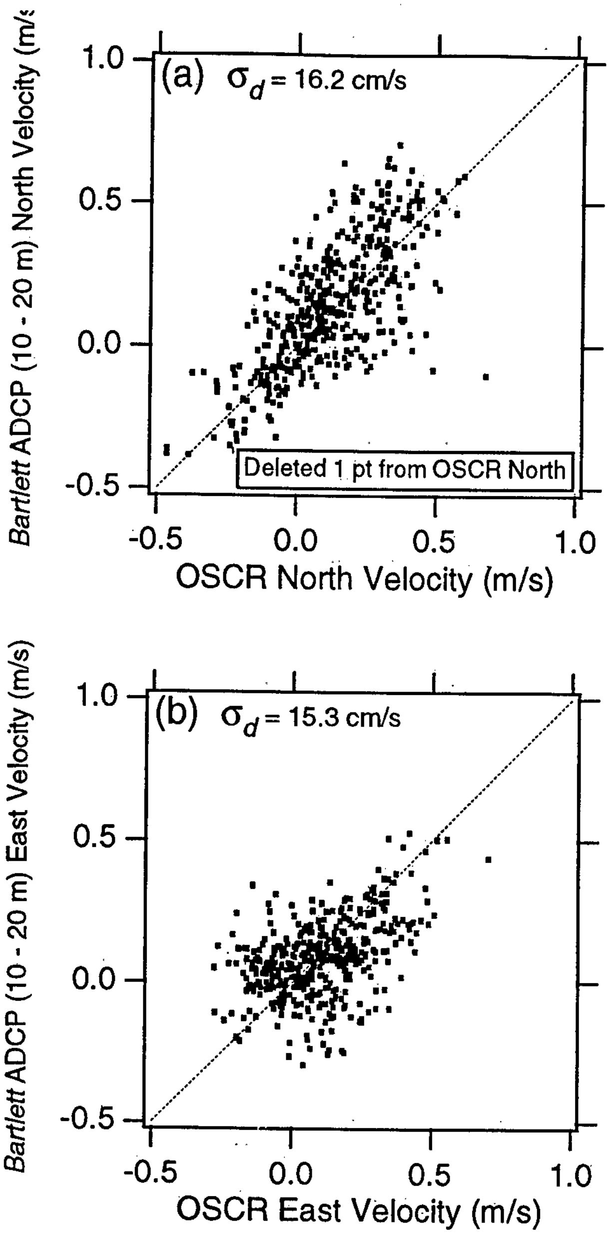

Figure 4. Comparisons of the surface current component estimates made from the *Bartlett* ADCP and OSCR.

4. The *Iselin* ADCP shows better agreement during the period when LADAS was deployed then for the experiment as a whole. There are two likely explanations for this. First, the *Iselin* was limited in speed when LADAS was deployed. Second, LADAS was only deployed in low-to-moderate sea state conditions. These effects combined to reduce ADCP noise during LADAS deployment relative to the experiment as a whole.

4.6. Estimates of Shear

To better examine the effects of shear, we computed the rms differences between measurements at various depths and the measurement at 1.6-m depth made by the TOAD ADCP. Figure 6 shows these rms differences as a function of depth for the north and east current components. We are using the rms differences, which include the mean biases between the measurement sets, because any mean shear will contribute to the observed differences between the in situ and OSCR data in the same manner as fluctuating differences or noise.

Figure 6 indicates that the rms differences grow quickly in the upper 4 to 5 m, and then more slowly below that depth. The last column in Table 1, labeled "TOAD rms Shear," contains estimated rms differences taken from Figure 6 at the depths of the instruments being compared. In making these estimates we assumed that there was no vertical shear in the near-surface layer above the bins sampled by the TOAD ADCP. The reader is cautioned that these results cannot be directly applied to compensate for shear in Table 1, because many of the measurements were taken at different locations and because the analysis does not separate the shear effects from depth-dependent noise in the TOAD ADCP. We have included these values solely for the purpose of comparison. Despite these caveats, the data do suggest that the effects of vertical shear are largest on the differences observed between the deepest and shallowest instruments. Furthermore, it appears that the differences due to shear are probably comparable to the differences due to other sources.

4.7. Calculation of Geometric Dilution of Precision for OSCR

The comparisons we have presented to this point have been limited to scatterplots and first-order statistics. The next step in this analysis is to examine the spatial dependence of the observed differences. During the 2 weeks of the experiment, the two research vessels traversed most of the OSCR measurement domain numerous times. Figure 7 is a map of the locations of the research vessels during the experiment. This wide range of measurement locations, combined with a simple theoretical model predicting the response of OSCR, can be used to examine the spatial dependencies of errors in the OSCR estimates.

Simple figures of merit for OSCR's ability to estimate surface current components can be derived. (The reader is referred to *Lipa and Barrick* [1983] for an alternative derivation.) Figure 8 presents a sketch of the geometry pertinent to current component determination with OSCR. Within this diagram, site 1 and site 2 are the locations of the OSCR master and slave sites, respectively. At each point in the OSCR measurement domain, the radial velocities, V_1 and V_2, are estimated.

The in-line and orthogonal velocities, V_i and V_o, can be estimated in terms of the sums and differences of the radial velocities:

$$\begin{aligned} V_i &= (V_1 + V_2)/2\cos\theta, \\ V_o &= (V_1 - V_2)/2\sin\theta, \end{aligned} \tag{1}$$

where θ is half of the angle between the intersecting beams. The in-line and orthogonal velocities can then be rotated to obtain estimates of the north and east velocity components:

$$\begin{aligned} V_n &= V_i \sin\alpha + V_o \cos\alpha, \\ V_e &= V_i \cos\alpha - V_o \sin\alpha, \end{aligned} \tag{2}$$

where α is the mean look angle as defined in Figure 8. Substitution yields

$$\begin{aligned} V_n &= \left(\frac{\sin\alpha}{2\cos\theta} + \frac{\cos\alpha}{2\sin\theta}\right)V_1 + \left(\frac{\sin\alpha}{2\cos\theta} + \frac{\cos\alpha}{2\sin\theta}\right)V_2, \\ V_e &= \left(\frac{\cos\alpha}{2\cos\theta} - \frac{\sin\alpha}{2\sin\theta}\right)V_1 + \left(\frac{\cos\alpha}{2\cos\theta} + \frac{\sin\alpha}{2\sin\theta}\right)V_2. \end{aligned} \tag{3}$$

These equations are of the form $z = aV_1 + bV_2$, where V_1 and V_2 are random variables representing the radial current measure-

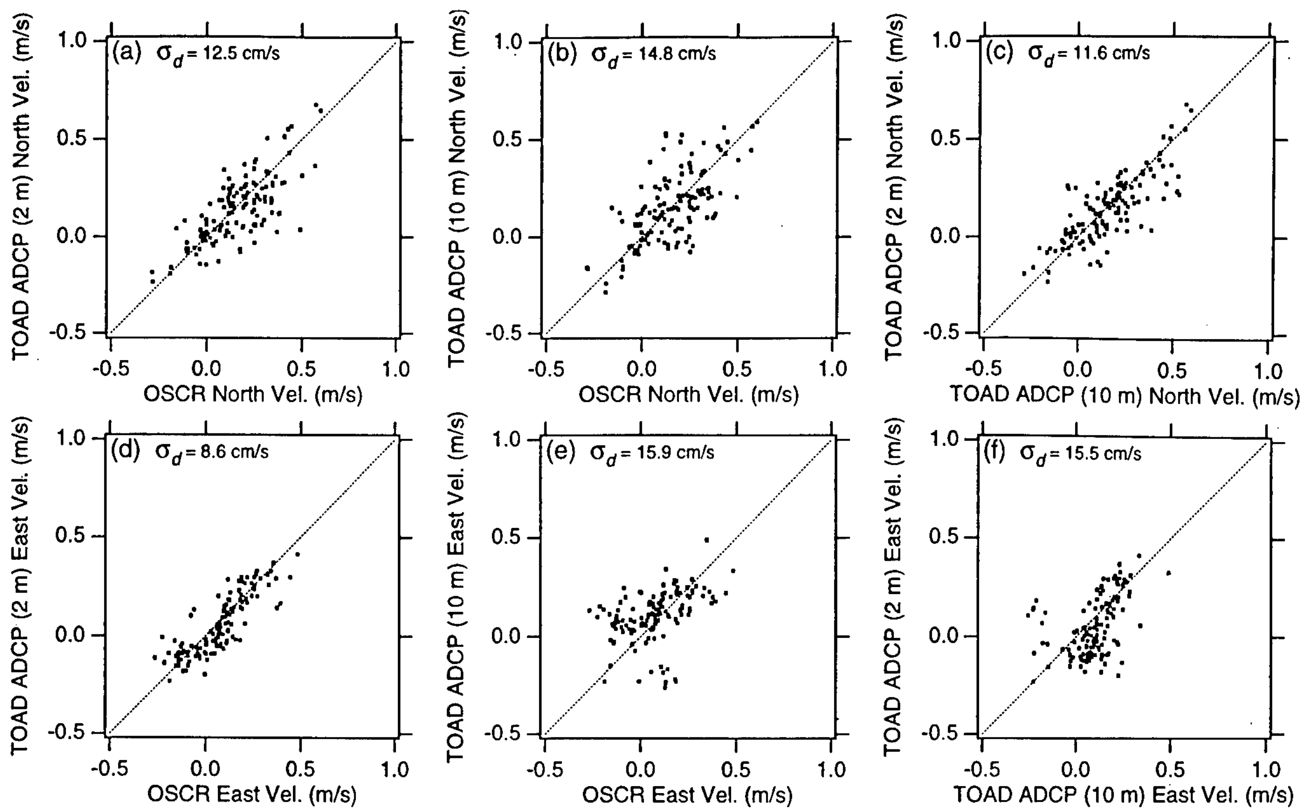

Figure 5. Comparisons of the surface current component estimates made from the TOAD ADCP and OSCR.

ments. If we assume that the noise in each radial measurement, σ, is identical, then the noise of the scaled sum is given by $\sigma_z = \sigma\sqrt{a^2+b^2}$. Applying the relationship $(u+v)^2 + (u-v)^2 = 2(u^2+v^2)$ to (3) yields estimates for the errors in the north and east components:

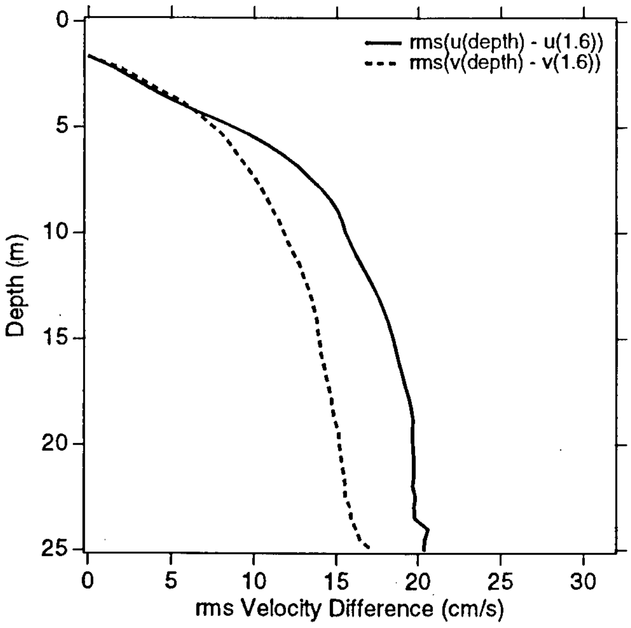

Figure 6. The rms differences observed in the TOAD ADCP data between current measurements made at various depths and those made at 1.6-m depth.

Table 1. Summary of the rms Differences Obtained from Comparisons of Differing Estimates of Surface Current Component Estimates

Measurement	Number	ρ	rms Difference, (cm/s)	TOAD rms Shear, (cm/s)
Iselin 4.6-m ADCP		0.79	14.8 ± 1.0	6.2
versus OSCR	404	0.73	14.5 ± 1.0	6.2
Iselin 5.6-m ADCP		0.79	15.1 ± 1.0	7.7
versus OSCR	404	0.70	15.3 ± 1.0	9.1
Iselin 4.6-m ADCP		0.99	3.2 ± 0.2	1.4
versus *Iselin* 5.6-m ADCP	404	0.99	3.0 ± 0.2	2.6
LADAS 1-m UCM		0.75	15.7 ± 2.2	0.0
versus OSCR	86	0.90	11.2 ± 1.6	0.0
Iselin 5.6-m ADCP versus OSCR (only during LADAS deployment)		0.85	11.0 ± 1.5	7.7
	86	0.88	12.6 ± 1.8	9.1
LADAS 1-m UCM versus		0.80	14.4 ± 2.0	8.3
Iselin 5.6-m ADCP	86	0.84	13.5 ± 1.9	10.3
Bartlett 10-m ADCP		0.71	16.2 ± 0.9	11.6
versus OSCR	465	0.48	15.3 ± 0.8	15.4
TOAD 2-m ADCP		0.75	12.5 ± 1.4	0.0
versus OSCR	130	0.85	8.6 ± 1.0	0.0
TOAD 10-m ADCP		0.66	14.8 ± 1.7	11.6
versus OSCR	130	0.39	15.9 ± 1.8	15.4
TOAD 2-m ADCP		0.80	11.6 ± 1.3	10.6
versus TOAD 10-m ADCP	130	0.46	15.5 ± 1.8	14.6
TOAD 2-m ADCP		0.78	12.2 ± 1.4	10.6
versus *Bartlett* ADCP	130	0.43	15.9 ± 1.8	14.6

The upper and lower values on each line are the north and east current component statistics, respectively. The last column, representing the magnitude of the vertical shear observed by the TOAD ADCP during the experiment, is based on an analysis of Figure 6.

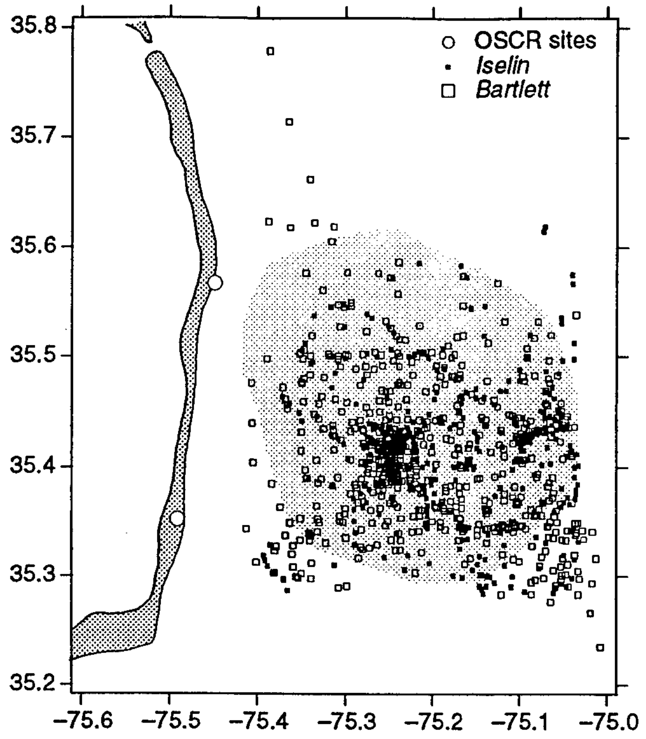

Figure 7. Map of research vessel locations during the experiment relative to the OSCR measurement domain.

$$\sigma_\mathrm{n} = \left[2\left(\frac{\sin^2\alpha \sin^2\theta + \cos^2\alpha \cos^2\theta}{\sin^2(2\theta)} \right) \right]^{1/2} \sigma,$$

$$\sigma_\mathrm{e} = \left[2\left(\frac{\cos^2\alpha \sin^2\theta + \sin^2\alpha \cos^2\theta}{\sin^2(2\theta)} \right) \right]^{1/2} \sigma. \qquad (4)$$

Borrowing from the terminology of the GPS navigation system [*Wells et al.*, 1986], we will refer to the ratios σ_n/σ and σ_e/σ as the north and east geometric dilution of precisions or GDOPs. These GDOPs can be thought of as multipliers of the noise associated with the geometry of the HF radar measurement. Applying these formulae, we can derive the map of the north and east GDOPs for the OSCR measurement domain shown in Figure 9.

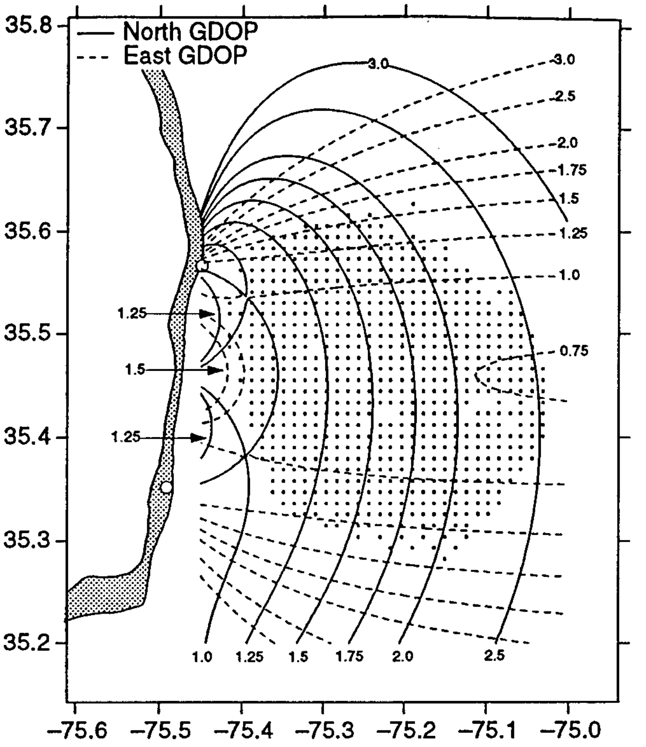

Figure 9. Map of the north (solid lines) and east (dashed lines) geometric dilution of precision (GDOP) for the OSCR measurement domain.

The map in Figure 9 indicates that the north GDOP varies from 1 to 2.5 in the OSCR domain, with the largest errors occurring at the farthest range cells. The east GDOP varies from 0.75 to 1.5, with the largest errors occurring at the northern and southern extremes of the domain. That the east GDOP falls below 1.0 at the farthest

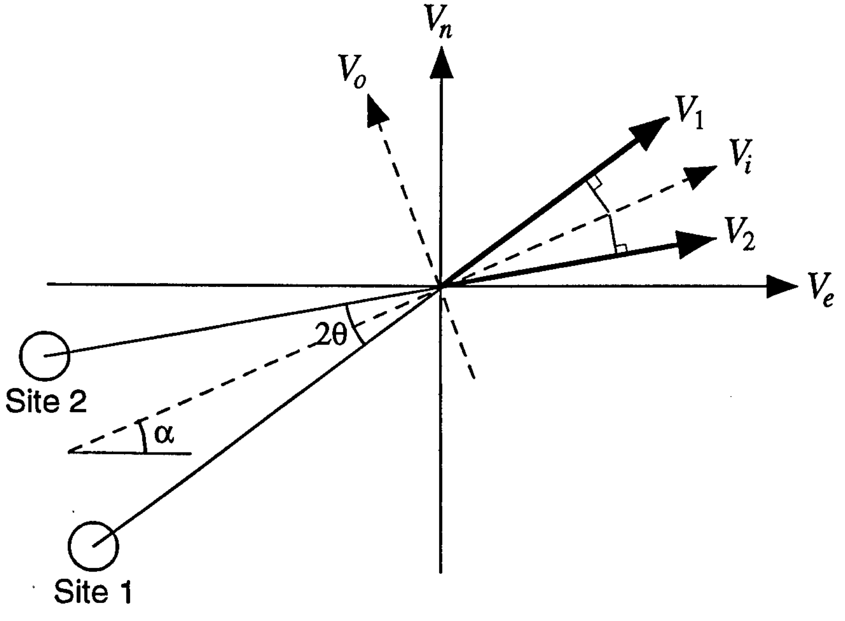

Figure 8. Geometry of OSCR current determination.

range cells should cause no surprise. At these locations, the radial velocity estimates are nearly parallel and so the estimate of the east component of velocity is nearly the average of the two radial velocity estimates. In the limiting case of a point infinitely distant toward the east, the error in the east velocity estimate would go to $\sigma/\sqrt{2}$ due to the averaging of two, like random variables. The apparent lack of symmetry in the map in Figure 9 is due to the fact that the sites are not aligned along a north-south axis.

It is important to note that the GDOP does not take into account the effects of reduced signal to noise that might be expected to decrease the accuracy of the current estimates in the farthest range bins. Its sole purpose is to predict the purely geometric component of the errors expected in the OSCR current estimates. We also note that the expressions in (4) are apparently not consistent with the similar but more general expressions derived by *Lipa and Barrick* [1983, equations (41) and (42)]. We attribute these differences to minor typographical errors in the paper by Lipa and Barrick. A reanalysis of their least squares approach to current determination in overdetermined systems shows that their corrected expressions reduce to our formula in the case of two sites.

Finally, our results are in disagreement with those of *Prandle* [1991, equation (2) and Figure 3]. We find that there is a typographical error in equation (2): the terms should be subtracted, not added. Furthermore, Figure 3 was apparently obtained by taking the absolute value of each of the terms in equation (2). This approach cannot be reconciled with our results, which correspond to adding the two terms of his equation (2) in quadrature. (Strictly speaking, this result only holds in the limit of large mean current magnitude. In general, the standard deviation of current magnitude depends on true mean current magnitude in a complex fashion, making it in an inappropriate method for comparison of current measuring devices.)

4.8. Apportionment of Errors

The theory of the previous section shows that the OSCR-dependent errors are position dependent. It is reasonable to assume that the errors due to other sources will not be position dependent. This distinction can be used to apportion the errors between the two sources.

The GDOP predictions suggest that the north component errors in our OSCR data should be larger than the east component errors. As we noted previously, there are only two cases where the differences between the north and east errors are statistically significant, and these are for the two shallowest in situ measurements, made by the LADAS UCM at 1-m depth and the TOAD ADCP at 2-m depth.

These observed differences can be used to apportion the observed errors through the observation that the total current difference variance for each component can be split into the sum of the variances of two terms:

$$\sigma_a^2 = \mathrm{GDOP}^2 \sigma_{\mathrm{OSCR}}^2 + \sigma_{\mathrm{other}}^2 , \qquad (5)$$

where σ_{OSCR}^2 is the effective radial velocity variance for OSCR and $\sigma_{\mathrm{other}}^2$ represents the variance from all other sources including the in situ measurement errors and the true differences in the measured quantities.

Given a pair of data sets with differing mean GDOP and assuming that the variances σ_{OSCR}^2 and $\sigma_{\mathrm{other}}^2$ are independent of direction or location, we can solve these equations for σ_{OSCR}^2 and $\sigma_{\mathrm{other}}^2$ using the observed mean σ_d for the data sets. The results of such an analysis are shown in the first two lines of Table 2. Note that the average north and east GDOPs for both the LADAS and TOAD data sets are 1.6 and 0.9, respectively. These average GDOP values are determined by the distribution of locations of the *Iselin* and *Bartlett* during the experiment. The fact that they are the same for LADAS and TOAD is somewhat coincidental.

Table 2. Analysis of Current Differences as a Function of GDOP

Platform Component	Mean GDOP	σ_d, cm/s	σ_{OSCR}, cm/s	σ_{other}, cm/s
LADAS UCM north	1.6	15.7	8.3	8.3
LADAS UCM east	0.9	11.2	8.3	8.3
TOAD 2 m north	1.6	12.5	6.9	5.9
TOAD 2 m east	0.9	8.6	6.9	5.9
Iselin north	···	11.1	6.3	6.7
Bartlett north	···	14.7	5.6	12.5

An alternative approach is to examine the dependence of differences on GDOP within a given data set. Figure 10 contains plots of the square of current estimate differences from both the *Iselin* and *Bartlett* ADCP/OSCR comparisons as a function of the square of GDOP. (The reasons for this particular choice of parameters will be made clear in the following discussion.) Similar plots for the TOAD and LADAS are not presented because of the limited number of points available from these platforms.

While an increase in the variance of the differences as a function of GDOP^2 is difficult to see, a consistent trend is indeed present in the north component current data. A statistical method for estimating the GDOP-dependent and -independent components of the variance is required to examine this trend. We began by assuming that for each point, the component difference is given by the two-dimensional stochastic equation

$$z_i = \mathrm{GDOP}_i \, x_i + y_i , \qquad (6)$$

where z_i is the observed component difference at the ith point, GDOP$_i$ is the GDOP at that location, x_i is the equivalent error in the OSCR radial velocities at point i, and y_i is the error in the other instrument. Squaring and taking the expected value yields

$$\langle z_i^2 \rangle = \langle \mathrm{GDOP}_i^2 \, x_i^2 \rangle + \langle y_i \rangle + 2 \langle \mathrm{GDOP}_i \, x_i y_i \rangle . \qquad (7)$$

Note that the expectation value is taken over the range of possible errors, which is, as in Figure 10, geometrically orthogonal to the GDOP axis. Thus we expect that GDOP$_i$ (which is not stochastic, but deterministic) and x_i are independent, an assertion we later check. We also assert that $\langle \mathrm{GDOP}_i^2 \rangle = \mathrm{GDOP}_i^2$, since the expectation operator acts orthogonal to GDOP$_i$. Finally, GDOP$_i$ and y_i are certainly independent and x_i should be independent of y_i, so (7) reduces to

$$\langle z_i^2 \rangle = \mathrm{GDOP}_i^2 \langle x_i^2 \rangle + \langle y_i^2 \rangle \qquad (8)$$

With the proper substitutions, this is exactly equation (5).

The mean error is very close to zero in these data, and more importantly, we a priori expect the errors to be zero mean, so the optimal estimator for variance is exactly the average of the variable y_i^2. Thus each y_i^2 can individually be thought of as a single point estimate of the local variance. With this as background, we chose to perform a least squares fit of a line to the squared errors y_i^2 plotted against GDOP$_i^2$. In the above notation the slope and intercept then are $\sigma_{\mathrm{OSCR}}^2 = \langle x_i^2 \rangle$ and $\sigma_{\mathrm{other}}^2 = \langle y_i^2 \rangle$, respectively.

This analysis depends on the independence of the radial errors in OSCR and GDOP. Possible reasons for such a dependence include reduced signal-to-noise ratio (SNR) with distance or an-

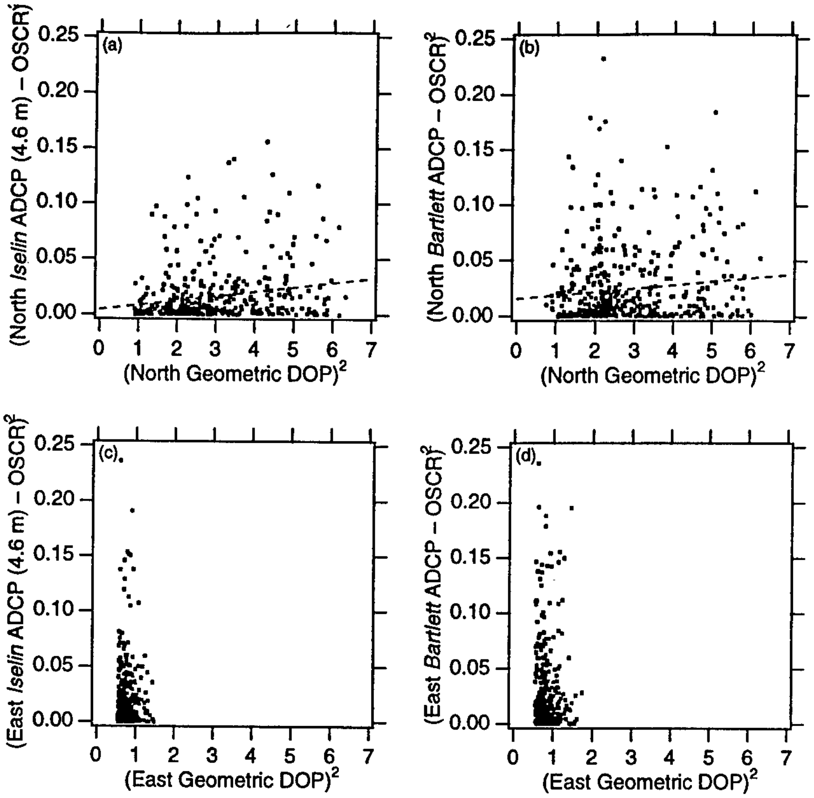

Figure 10. Comparisons of the *Iselin* and *Bartlett* current component estimation differences squared as a function of GDOP^2. The dashed lines in Figures 10a and 10b are the least squares line fit to the data, indicating the dependence of the error on GDOP.

tenna pattern effects. Thus, before applying the technique to the *Bartlett* and *Iselin* north data, the correlation of the radial errors with GDOP was examined. This comparison was performed by computing the differences between the radial current estimates from each OSCR site and the in situ currents projected into these same radial directions. We were somewhat surprised to find a statistically significant correlation between these differences and the GDOP. This correlation appears to be due to SNR reduction with distance, as the differences also correlated with distance from the site, but not with the antenna look angle. We found that these correlations were driven by measurements made at distances greater than about 30 km and disappeared when the data sets were limited to points closer than 30 km.

Thus the least squares line fit technique was applied to the subset of the *Bartlett* and *Iselin* north data that fall within 30 km of the central point between the OSCR sites. This analysis is somewhat sensitive to wild points so we eliminated all data points from the calculation where the total error exceeded 50 cm/s. This eliminated only four points from the *Iselin* data set and two points from the *Bartlett* data set.

The results of this analysis, shown in the last two lines of Table 2, agree substantially with the previous estimates. These results indicate that the effective radial velocity errors in the OSCR system are no worse than 6 to 8 cm/s, values comparable to those of all of the other combined errors.

We refer to σ^2_{OSCR} as the effective radial velocity variance in order to distinguish it from the simple radial velocity variance previously quoted as having a value of (2.2 cm)^2. We feel that this distinction is necessary since σ^2_{OSCR} is the sum of the simple radial velocity variance plus any additional variance which is correlated with the GDOP. For example, any variance due to measurement field mismatch, such as that resulting from an azimuthal misalignment of the antenna, is directly correlated with location. Given a direct correlation with location, this variance will also be indirectly correlated with the GDOP. Thus the fact that we estimate an effective radial velocity error of 7 to 8 cm/s is not necessarily in contradiction with the manufacturer's assertion of radial velocity errors of 2.2 cm/s.

5. Summary

This study is an attempt to assess the accuracy of remote surface current measurements using HF radars. In this study we have compared coincident near-surface current data from four separate platforms with data from a commercial HF radar system. Intercomparisons of the data from the various systems exhibit rms differences ranging from 9 to 16 cm/s. At the very least, these comparisons provide an absolute upper bound on the errors associated with the current estimates from the HF radar system.

We recognize though that all of the observed differences are not attributable to errors in the remote current estimates. Some of the differences are undoubtedly due to errors in the in situ measurements. More importantly, some of the differences are likely due to physical processes associated with different effective depths at which the measurements are made (i.e., vertical shear), as well as the difference in temporal and areal averaging of the remote and in situ measurements. An improvement in the error estimate for the HF radar system can thus only be obtained by some apportionment of the differences between these possibilities.

In order to further this analysis, we developed a simple model of the effect of measurement location on the HF radar errors. We utilize the fact that HF radar errors vary over the deployment area of our experiment. This allows us to decompose the differences observed between the HF radar data and those obtained from the in situ sensors. Four such decompositions suggest that the effective radial velocity errors in the HF radar system are no more than 7 to 8 cm/s, a value comparable to the total noise from all other sources of current differences.

Even given HF radar errors as large as 7 to 8 cm/s, such systems can still be extremely useful for a variety of research projects. It is important to note that due to the nature of our analysis we are unable to examine the temporal correlation of the noise. If, as we expect, the noise in the OSCR system is not temporally correlated, this noise will be spread over a broad range of temporal frequencies. The noise within any particular frequency band of interest, say a tidal band, would thus be a small fraction of the values quoted here. For example, the standard deviation within a single frequency bin of a spectral estimate obtained from an 1100-point time series would be $(8\ \mathrm{cm/s})/\sqrt{550} = 0.34$ cm/s. A realistic tidal surface current of 5 to 8 cm/s, as found by *Shay et al.* [1995], could be easily resolved above this noise level.

In summary, while HF radar systems have been promoted for remote surface current measurements for over a decade, we believe that their acceptance within the general oceanographic community has been slowed by a lack of validation studies. This study, along with the related studies of *Shay et al.* [1995] and *Graber et al.* [this issue], is our attempt to fill this void. These studies demonstrate that the remote sensing of surface currents in coastal areas using HF radar systems is an accurate technology suitable for wider use within the oceanographic community.

Acknowledgments. The authors would like to thank Daniel Fernandez for pointing out the underlying consistency of our work with that of Lipa and Barrick. We'd also like to thank Erik Bock for use of LADAS as a platform for making some of these measurements. The insightful reviews of Jeff Paduan and David Prandle were much appreciated. This research was supported, in part, by the following grants from the Office of Naval Research: N00039-91-C-0001 (Chapman), N00014-92-J-1585 (Edson and Karachintsev), N000-96-1-1111 (Shay), and N00014-91-J-1775 (Graber). The OSCR measurements were supported by the ONR Remote Sensing program and Minerals Management Service through grant N00014-91-J-4133 (Shay, Ross, and Graber).

References

Barrick, D. E., J. M. Headrick, R. W. Bogle, and D. D. Crombie, Sea backscatter at HF: Interpretation and utilization of the echo, *Proc. IEEE, 62*, 673–680, 1974.

Barrick, D. E., M. W. Evans, and B. L. Weber, "Ocean surface currents mapped by radar," *Science, 198*, 138–144, 1977.

Bock, E. J., and T. Hara, Optical measurements of capillary-gravity wave spectra using a scanning laser slope gauge, *J. Atmos. Oceanic Technol., 12*(2), 395–403, 1995.

Crombie, D. D., Doppler spectrum of sea echo at 13.56 Mc./s., *Nature, 175*, 681–682, 1955.

Crombie, D. D., Resonant backscatter and its application to physical oceanography, in *Proceedings of IEEE Ocean '72 Conference on Engineering in the Ocean Environments*, 174–179, IEEE Press, Piscataway, N.J., 1972.

Edson, J. B., J. E. Hare, and C. W. Fairall, Direct covariance flux estimates from mobile platforms at sea, *J. Atmos. Oceanic Technol.*, in press, 1996.

Fernandez, D. M., and J. D. Paduan, Simultaneous CODAR and OSCR measurements of ocean surface currents in Monterey Bay, in *IEEE International Geoscience and Remote Sensing Symposium*, pp. 1749–1752, IEEE Press, Piscataway, N.J., 1996.

Frisch, A. S., and B. L. Weber, A new technique for measuring tidal currents by using a two-site HF Doppler radar system, *J. Geophys. Res., 85* (C1), 485–493, 1980.

Georges, T. M., and J. A. Harlan, Mapping surface currents near the Gulf Stream using the Air Force over-the-horizon radar, in *Proceedings of the IEEE Fifth Working Conference on Current Measurement*, pp. 115–120, IEEE Press, Piscataway, N.J., 1995.

Graber, H., B. K. Haus, L. K. Shay, and R. D. Chapman, HF radar comparisons with moored estimates of current speed and direction: Expected differences and implications, *J. Geophys. Res.*, this issue.

Herr, F., C. Luther, G. Marmorino, R. Mied, and D. Thompson, Ocean surface remote-sensing program planned, *Eos, 72*, 214, 1991.

Holbrook, J. R., and A. S. Frisch, A comparison of near-surface CODAR and VACM measurements in the Strait of Juan De Fuca, August 1978, *J. Geophys. Res., 86*(C11), 10,908–10,912, 1981.

Leise, J. A, The analysis and digital signal processing of NOAA's surface current mapping system, *IEEE J. Oceanic Eng., OE-9*(2), 106–113, 1984.

Lipa, B. J., and D. E. Barrick, Least-squares methods for the extraction of surface currents from CODAR crossed-loop data: Application at ARSLOE, *IEEE J. Oceanic Eng., OE-8*(4), 226–253, 1983.

Marmorino, G. O., and C. L. Trump, Preliminary side-scan ADCP measurements across a ship's wake, *J. Atmos. and Oceanic Technol., 13*(2), 507–513, 1996.

Matthews, J. P., J. H. Simpson, and J. Brown, Remote sensing of shelf sea currents using a high-frequency ocean surface current radar system, *J. Geophys. Res., 93*(C3), 2303–2310, 1988.

Paduan, J. D., and L. K. Rosenfield, Remotely sensed surface currents in Monterey Bay from shore-based HF radar (Coastal Ocean Dynamics Application Radar), *J. Geophys. Res., 101*(C9), 20,669–20,686, 1996.

Peters, N. J., and R. A. Skop, VHF radar measurements of ocean surface currents from a moving ship, *RSMAS Tech. Rep. 95-007*, 56 pp., Univ. of Miami, Miami, Fla., 1995.

Porter, D. L., R. G. Williams, and C. R. Swassing II, CODAR intercomparison: Delaware Bay 1984, in *Proceedings of IEEE Third Working Conference on Current Measurement*, pp. 36–44, IEEE Press, Piscataway, N.J., 1986.

Prandle, D., A new view of near-shore dynamics based on observations from HF radar, *Prog. Oceanogr., 27*, 403–438, 1991.

Shay, L. K., H. C. Graber, D. B. Ross, and R. D. Chapman, Mesoscale ocean surface current structure detected by HF radar, *J. Atmos. Oceanic Technol., 12*(4), 881–900, 1995.

Skop, R. A., D. B. Ross, N. J. Peters, and L. Chamberlain, Measurements of coastal currents using a ship based VHF radar system, *RSMAS Technical Report 94-001*, 25 pp., Univ. of Miami, Miami, Fla., 1994.

Stewart, R. H., and J. W. Joy, HF radio measurements of surface currents, *Deep Sea Res., 21*, 1039–1049, 1974.

Trizna, D., Mapping ocean currents using over-the-horizon HF radar, *Int. J. Remote Sens., 3*(3), 295–309, 1982.

Wells, D. E., et al., *Guide to GPS Positioning*, Can. GPS Assoc., Fredericton, N. B., Canada, 1986.

R. D. Chapman, Applied Physics Laboratory, Johns Hopkins University, Laurel, MD 20723 (e-mail: chapman@tesla.jhuapl.edu).

L. K. Shay and H. C. Graber, Rosenstiel School of Marine and Atmospheric Sciences, University of Miami, 4600 Rickenbacker Causeway, Miami, FL 33149.

J. B. Edson and A. Karachintsev, Woods Hole Oceanographic Institution, Woods Hole, MA 02543.

C. L. Trump, Code 7340, Naval Research Laboratory, 4555 Overlook Ave., S.W. Washington, D. C. 20375.

D. B. Ross, Ivy Inc., 3100 N. Bay Road, Miami, FL 33140.

(Received March 21, 1996; revised November 12, 1996;
accepted November 22, 1996.)

Made in United States of America
Reprinted from Journal of Atmospheric and Oceanic Technology
Vol. 14, No. 3, Part 2, June 1997

Altimeter Estimation of Sea Surface Wind Stress for Light to Moderate Winds

DOUGLAS VANDEMARK

NASA/Goddard Space Flight Center, Wallops Island, Virginia

JAMES B. EDSON

Woods Hole Oceanographic Institution, Woods Hole, Massachusetts

BERTRAND CHAPRON

Institut Français de Recherche pour l'Exploitation de la Mer, Plouzane, France

3 May 1996 and 10 September 1996

ABSTRACT

Aircraft altimeter and in situ measurements are used to examine relationships between altimeter backscatter and the magnitude of near-surface wind and friction velocities. Comparison of altimeter radar cross section with wind speed is made through the modified Chelton–Wentz algorithm. Improved agreement is found after correcting 10-m winds for both surface current and atmospheric stability. An altimeter friction velocity algorithm is derived based on the wind speed model and an open-ocean drag coefficient. Close agreement between altimeter- and in situ–derived friction velocities is found. For this dataset, quality of the altimeter inversion to surface friction velocity is comparable to that for adjusted winds and clearly better than the inversion to true 10-m wind speed.

1. Introduction

Relationships between ocean wind speed, wind stress, and microwave remote sensing are both elementary and complicated. Because of the relative ease and availability of wind speed measurements, ocean wind speed algorithms for the scatterometer, altimeter, and radiometer have been the first developed. Wind models for these three sensors have been demonstrated with uncertainty of order 2 m s^{-1} (Stoffelen and Anderson 1993; Witter and Chelton 1991; Wentz 1992). The physics behind these semiempirical wind algorithms is quite different for each sensor. For each case, it is clear they cannot directly map their respective measurement to the 10-m wind speed. For radar scatterometers, known contamination of wind speed inversion can come from nonwind geophysical effects such as atmospheric stratification, current or SST fronts, surfactant, and sea state. To account for these influences, some have suggested relating scatterometer measurements directly to surface friction velocity u_*, a measure of wind stress that implicitly carries a response to near-surface phenomena. A major limitation here has been that wind stress measurements are not available on anywhere near the scale of buoy and ship wind speed data. Field data have just recently become available (Colton et al. 1995; Weissmann et al. 1994) that indicate Ku-band scatterometer backscatter is more closely correlated with u_* than with 10-m wind speed.

A clear connection between altimeter radar cross section (σ_0) and sea surface wind stress is not yet established. Wu (1992) proposed an altimeter algorithm for wind stress based on the physical relationship of altimeter response to changes in ocean ripples and on examination of the modified Chelton–Wentz (MCW) (Witter and Chelton 1991) altimeter wind speed retrieval algorithm. However, aside from several studies on sea state effects (Glazman and Greysukh 1993; Queffeulou et al. 1995), there is little published data to support or deny measurable nonwind effects on the altimeter–wind speed relationship. This may be because of a scarcity of altimeter measurements collected over well-instrumented research sites. Nonetheless, theory suggests a strong parallel between surface wind stress and altimeter backscatter in that both are formed through partial integration of the wave slope distribution (Brown 1979; Kitaigorodskii 1973). If a satellite altimeter can reliably retrieve wind stress, this may aid refinement of other satellite sensor and general circulation model wind stress estimates.

Recently, aircraft altimeter backscatter data were collected over open-ocean research platforms during the High Resolution Remote Sensing program. Our objec-

---

Corresponding author address: Douglas Vandemark, NASA/GSFC, Bldg. N-159, Wallops Island, VA 23337.
E-mail: vandemark@gsfc.nasa.gov

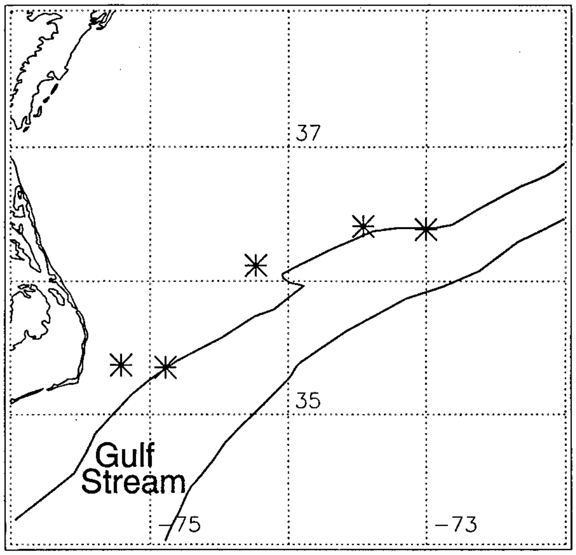

FIG. 1. Map of the High Resolution Program, June 1993 experiment area. The area is centered near 36°N, 74°W. Gulf Stream is depicted based on AVHRR imagery of 18 June 1993. Symbols represent the vicinity of R/V measurements for each of five ROWS flight days.

tive is to use the resulting altimeter–in situ dataset to examine altimeter σ_0 conversion to wind and wind stress relying primarily on the MCW satellite wind speed algorithm.

2. Remote and in situ measurements

a. Experiment background

Data for this presentation were collected during the Office of Naval Research High Resolution Remote Sensing experiment of June 1993. Near-surface environmental measurements were made by the R/V *Iselin,* the LADAS (laser slope gauge, acoustic Doppler current meter, acoustic anemometer, sodar) platform, and USNS *Bartlett.* A map of R/V locations for five separate aircraft flight days is provided in Fig. 1. The ships were generally located near the Gulf Stream north wall. Aircraft radar altimeter overflights of the experiment area occurred on 11, 14, 17, 20, and 27 June. NASA's T-39 aircraft carried the Radar Ocean Wave Spectrometer (ROWS), with its Ku-band radar altimeter, at a nominal altitude of 5500 m. Typically the aircraft was over the experiment area for a period lasting between 1.5 and 2 h during each flight, passing near the ships intermittently.

b. Surface measurements

Extensive near-surface measurements were acquired by the research vessels. These included wind and wind stress vectors, as well as parameters needed to determine atmospheric stratification. Wind speeds were measured at heights ranging from 6 to 12 m and adjusted to 10 m using the boundary layer model of Fairall et al. (1996). Friction velocity estimates were made using inertial dissipation (*Iselin,* LADAS, *Bartlett*) and direct eddy correlation (*Iselin,* LADAS) methods. We note that the inertial dissipation technique does not provide wind stress vector direction. Near-surface currents were estimated based on current measurements made at 1 m (LADAS) to several meters depth (ship-based ADCP). Because the ships were often in the Gulf Stream, near-surface current vector measurements were crucial for correct boundary layer characterization. Wind speeds relative to the earth (the absolute wind speed) and relative to the drift current were computed. All parameters were derived using a 10-min averaging period. Uncertainty for the 10-min-averaged wind and friction velocity estimates is less than 10% and 30%, respectively. These somewhat higher than normal uncertainties are mainly due to the nonhomogeneous conditions encountered near the Gulf Stream edge.

Wind conditions for the five ROWS flights varied from a very light wind event to moderate 10 m s^{-1} southerly flow. Significant wave height was 1.5 m on 14 and 27 June, below 1.0 m otherwise. The range of air–sea temperature difference was $-5.6°$ to $3.9°$, the range of the stability parameter z/L (at 10 m) was -0.5 to 0.82, and the range of effective current (current with respect to wind vector) was -2.0 to $+0.5$ m s^{-1}.

c. Aircraft altimeter measurements

The airborne altimeter measurements were made using NASA's airborne ROWS. This Ku-band (2.24-cm wavelength) radar system comprises both an altimeter and a scanning high-resolution scatterometer (Vandemark et al. 1994a). ROWS altimeter data are collected using a pulse-limited altimeter technique associated with wide-beam horn antenna operation. The altimeter derives cross section rolloff versus incidence angle from the omnidirectional return signal (Hammond et al. 1977). Incidence angle coverage is near vertical, from 0° out to 12°. Slope of the falloff is proportional to rms sea surface slope and after correction for the antenna pattern is termed the Ku-band mean-square slope (mss$_{\text{ku}}$). The subscript differentiates altimeter mss from the true or total surface slope because diffraction effects limit the microwave sensor to a partial integration of total slope. The altimeter signal reflects off a "filtered surface" composed of all length scales greater than about three times the transmit wavelength. Theoretical prediction and measurements show that mean-square slope is inversely proportional to altimeter σ_0 at 0° incidence (the pulse-limited altimeter σ_0) (Brown 1978; Hammond et al. 1977; Jackson et al. 1992). For a Ku-band altimeter,

$$\sigma_0(\theta = 0°) = \frac{R_{\text{eff}}}{\text{mss}_{\text{ku}}}, \tag{1}$$

where we define R_{eff} as an effective Fresnel coefficient and θ as the radar's pointing or incidence angle. We convert the ROWS mss_{ku} to Ku-band $\sigma_0(0°)$ using $R_{\text{eff}} = 0.34$. This number compares well with others at Ku-band (Wu 1992; Apel 1994; Jackson et al. 1992). Compilation and processing details for this dataset are given in Vandemark et al. (1994b). ROWS mss_{ku} estimates are generated at 2-km intervals along the flight track and the nominal area for each estimate is 2 km^2. Uncertainty of the mss_{ku} measurement is estimated at 5% due to antenna pattern measurement and processing algorithm limitations. This translates to about 0.2 dB in σ_0.

d. Altimeter wind speed and friction velocity algorithms

The modified Chelton–Wentz wind speed retrieval algorithm is used to convert our altimeter σ_0 to altimeter-derived wind speed at 10 m ($U_{10\,\text{MCW}}$). MCW is given in tabular format without a closed functional dependence between wind and σ_0. This model was empirically derived for the Ku-band satellite altimeter. Independent buoy comparisons indicate a root-mean-square algorithm–buoy wind speed difference of 1.9 m s^{-1}, a result recently affirmed by Gower (1996) using TOPEX satellite altimeter data. The intercomparison error budget comprises the algorithm, buoy uncertainties, sensor noise, and time–space sampling differences (Monaldo 1988).

Wu (1992) proposed an altimeter friction velocity algorithm that simply combined his semianalytical altimeter wind speed algorithm with a wind stress, or drag, coefficient. The open-ocean, neutral stability drag coefficient at 10 m (Cd_{10}) was defined as

$$\begin{aligned}\text{Cd}_{10} &= \left[\left(\frac{1}{\kappa}\right)\ln\left(\text{Cd}_{10}^{1/2}U_{10}\frac{10}{\nu}\right) + 5.5\right]^{-2},\\ &\qquad U_{10} < 2.4\ \text{m s}^{-1}\\ \text{Cd}_{10} &= (0.8 + 0.065U_{10})10^{-3},\\ &\qquad U_{10} > 2.4\ \text{m s}^{-1},\end{aligned} \tag{2}$$

where ν is the kinematic viscosity of air and $\kappa = 0.4$ is the von Kármán constant. Our proposed altimeter u_* algorithm is also a mapping of altimeter σ_0 into friction velocity using (2), but for altimeter wind speed we use the empirically derived MCW algorithm to give

$$u_{*\,\text{MCW}} = \text{Cd}_{10}^{1/2}U_{10\,\text{MCW}}. \tag{3}$$

Note that both terms on the right-hand side of (3) are assumed to represent open-ocean, neutral stratification conditions.

Equations (2) and (3) imply that surface wind stress and wind speed are, on average, closely coupled. However, it is recognized that significant deviation from this average relationship can occur with surface layer stratification changes and because wind stress is also affected by additional near-surface, nonwind phenomena such as drift current and shear, slicks, swell, and wave steepness (Geernaert and Plant 1990). If altimeter σ_0 and u_* are indeed more highly correlated than σ_0 and U_{10}, Eq. (3) will provide a better alternative for single parameter inversion between the Ku-band altimeter and a measurable geophysical parameter.

3. Results

a. Wind speed

After assembling R/V and aircraft datasets, coincident pairs were found using a search radius of ±30 min and ±15 km. The resulting dataset contains 39 samples. Sampling is spatial for the altimeter with a footprint equal to 2 km^2, and temporal for the R/V data with an averaging time equal to 10 min. These are of the same order, as 10 min at nominal 7 m s^{-1} wind advection would amount to a sampling of 4 km along wind. This sampling is at a slightly higher resolution than typical satellite altimeter–buoy comparisons that use about 6-km along-track altimeter data (~12 km^2) and 10-min buoy averages.

Figure 2 shows wind speed estimates at 10 m versus altimeter σ_0. Abscissas for the three plots are, respectively, wind speed with respect to earth reference (absolute wind speed), with respect to surface current (relative wind speed), and with both current and atmospheric stability adjustments applied. The range of wind speeds is 2–12 m s^{-1}. The MCW wind speed algorithm is shown on all plots. Altimeter cross-section values appear above the curve (negative wind speed bias) at light winds, but there is good overall agreement between data and model. Improved agreement between data and MCW model is apparent for successive wind corrections at both light and higher wind speeds. Statistics from the direct comparison of altimeter- and in situ–derived wind speed are given in Table 1. Marked improvement in each statistical parameter is found as wind corrections are applied. The largest improvements appear to come with the adjustment for current.

For these data, MCW-derived altimeter wind speed is most closely related to an adjusted wind speed, not the true wind speed. The 11% increase in regression correlation coefficient R is considerable. Bias and rms uncertainty are lowered by a factor nearing 2. Thus, the altimeter wind speed inversion is subject to nonwind effects. Moreover, best agreement with adjusted wind speed suggests the link between friction velocity and altimeter σ_0.

b. Friction velocity

Friction velocity versus altimeter σ_0 is shown in the upper panel of Fig. 3. The model is altimeter $u_{*\,\text{MCW}}$ (3). Data agree closely with the model although σ_0 values are slightly high at lighter winds. Direct comparison

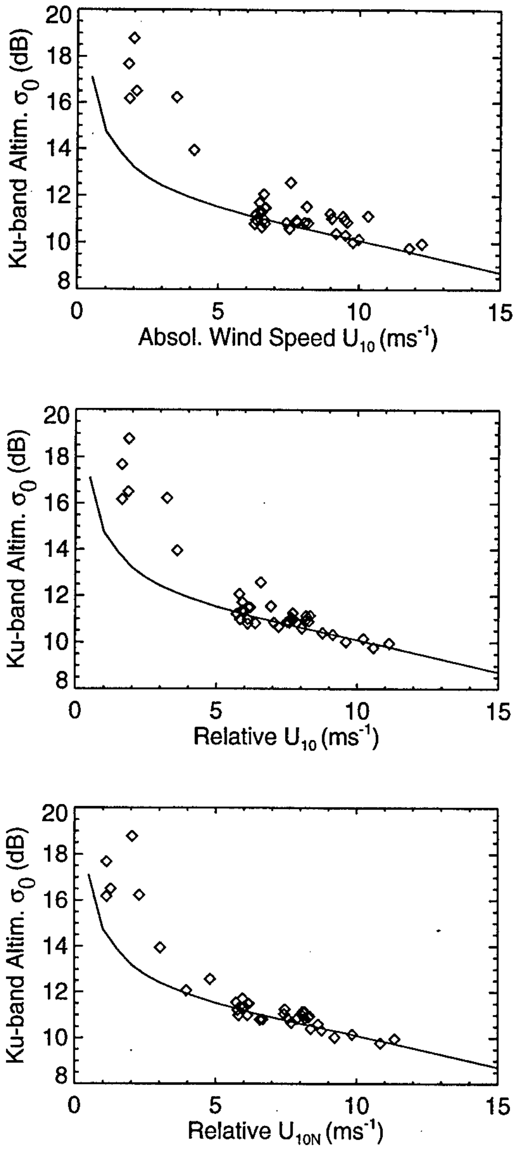

FIG. 2. Ku-band altimeter normalized radar cross section (NRCS) and R/V absolute and adjusted wind speed measurements. The curve is the MCW 10-m wind speed algorithm. Adjustment of R/V 10-m wind speed estimates between plots is indicated.

TABLE 1. Correlation coefficient, bias, and root-mean-square error between in situ and altimeter wind and friction velocities.

Wind comparisons	R	Bias (m s^{-1})	rms error
U_{10} vs $U_{10\,\mathrm{MCW}}$	0.86	−1.41	1.43
Relative U_{10} vs $U_{10\,\mathrm{MCW}}$	0.93	−0.83	1.10
Relative $U_{10\mathrm{N}}$ vs $U_{10\,\mathrm{MCW}}$	0.96	−0.69	0.86
Bulk u_*vs $u_{*\,\mathrm{MCW}}$	0.94	−0.029	0.037
u_* vs $u_{*\,\mathrm{MCW}}$	0.93	−0.016	0.039

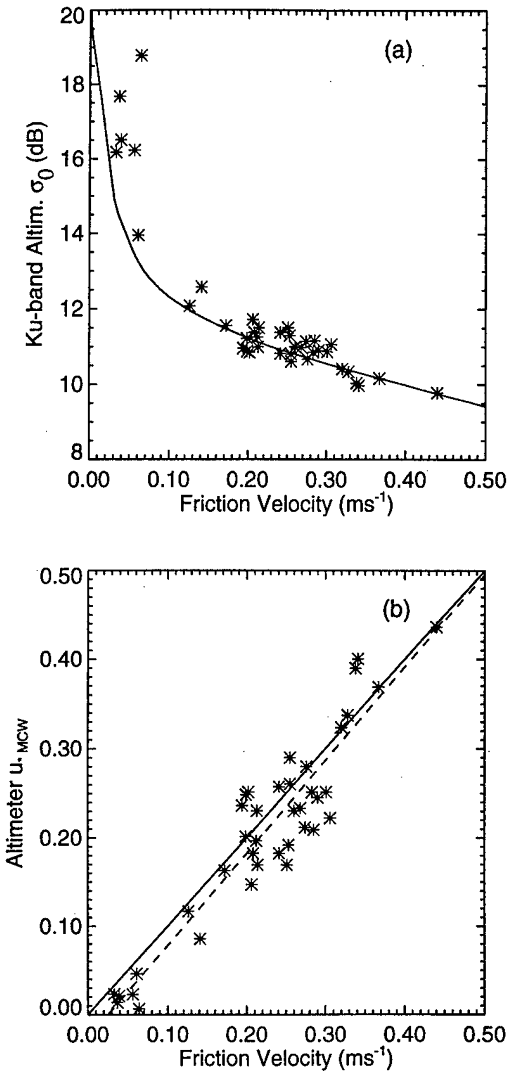

FIG. 3. (a) Ku-band altimeter σ_0 and R/V friction velocity measurements. The curve is the proposed $u_{*\,\mathrm{MCW}}$ algorithm. (b) Scatterplot of altimeter- and R/V-derived friction velocities. Linear regression (dashed) is shown.

between altimeter- and ship-derived u_* is shown in the bottom panel. A linear fit gives a slope of 1.04 and intercept of −0.026. Statistics are again shown in Table 1. We include comparison to u_* derived using the bulk method. In large part, bulk-derived friction velocity and adjusted 10-m wind speeds are the same entity. Therefore, we have included this entry to allow further comparison between the adjusted wind speed and turbulence-derived estimates of u_* found from the inertial-dissipation and direct covariance methods. The comparison bias using turbulence-derived estimates is half that when using the bulk data, otherwise the two u_* comparisons are very similar. Table 1 then indicates that altimeter-derived wind stress is as viable a derivative as corrected wind speed and clearly an improvement over an inversion to true wind speed.

c. Current and atmospheric stability effects on u_*–altimeter correlation

The altimeter and in situ friction velocity comparison demonstrates very good agreement between our measurements and model. Remaining scatter between those measurements is presented here to examine the robustness of this direct mapping between altimeter σ_0 and u_*.

Previously, Wu (1991) found that both optical mean-square slope (in situ) and C-band scatterometer (remote) data indicated enhanced (suppressed) small-scale surface roughness under unstable (stable) atmospheric conditions at a given wind speed. This indicated a closer tie between those measurements and surface wind stress than between those measurements and wind speed. However, Wu went on to find that both sensors measured a response to stratification change that was stronger than the response of wind stress to the same conditions. The conclusion was that a significant air–sea temperature dependence still existed to preclude direct mapping between u_* and those particular measurements. The altimeter differs significantly from those sensors in its response to surface roughness, and we now examine our measurements in the presence of current and stability influences to see how altimeter and u_* measurements behave.

The difference between altimeter and in situ u_* estimates is presented here as a ratio between the actual altimeter mean-square slope measurements and the prediction from our proposed u_*–altimeter model (3). This approach provides consistency with past studies (Hwang and Schemdin 1988; Wu 1991). Recall that $\mathrm{mss}_{\mathrm{ku}}$ is directly tied to altimeter σ_0 through (1). Inversion of (3) using in situ friction velocity input provides the normalizing mss_{u_*}:

$$S_r = \frac{\mathrm{mss}_{\mathrm{ku}}}{\mathrm{mss}_{u_*}}. \qquad (4)$$

The upper plot of Fig. 4 shows this altimeter mean-square slope ratio S_r against effective current for each sample. Ambient or effective current v is defined here as the current vector's dot product with the unit wind vector. For almost all of these samples, wind and current directions were at least partially aligned, giving an effective wind suppression or negative current. There is a significant spread in S_r with current, but also an apparent positive correlation. An effective current stronger than $-1.0\ \mathrm{m\ s^{-1}}$ suppresses $\mathrm{mss}_{\mathrm{ku}}$ in comparison to the still-water u_* relationship. The plus symbols in both panels of Fig. 4 represent data collected in very stable atmospheric conditions. If these outliers ($10/L > 0.2$) are excluded from the data, a linear regression yields

$$S_r = 1.02 + 0.05v \pm 0.063. \qquad (5)$$

The bottom plot of Fig. 4 shows S_r against the dimensionless Monin–Obukhov stability length, L, at 10 m. In stable conditions, $\mathrm{mss}_{\mathrm{ku}}$ is reduced relative to u_* for

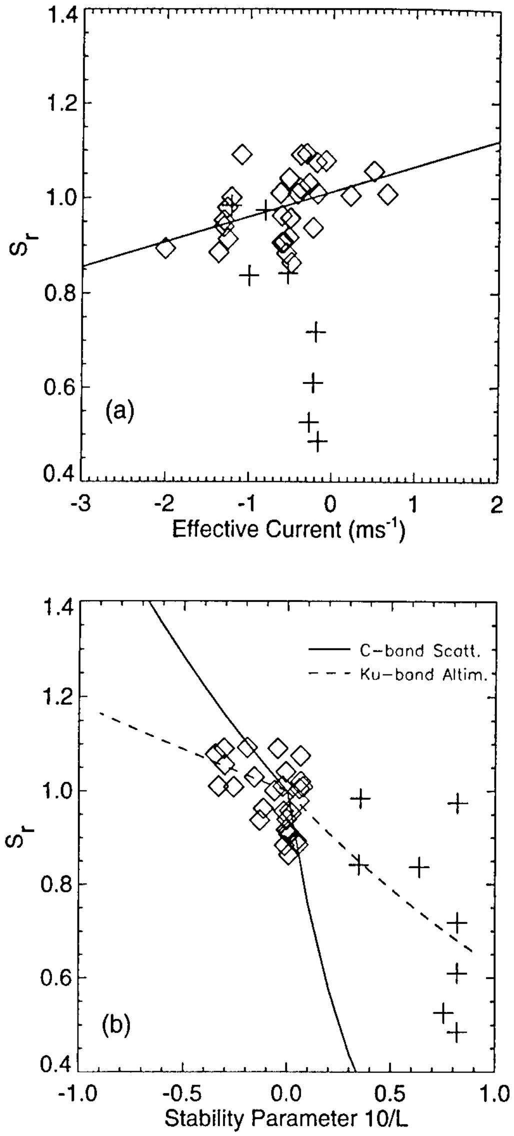

FIG. 4. Environmental parameters (a) effective current, and (b) stability vs altimeter measurement deviation, Eq. (5), from the $u_{*\,\mathrm{MCW}}$ algorithm. Measurements in stable stratification are denoted with the "+" symbol. In (a) a linear regression for S_r vs current is shown. In (b), solid curve is (6) and (7) with exponents from the C-band scatterometer. Dashed curve is the present data fit to (6) and (7) giving $\alpha = 0.17$ and $\beta = 0.47$.

several samples but not all. In unstable conditions, the departure from u_* is not strong. Model curves on the plot are based on previous empirical examination of atmospheric stability and small-scale wave observations (Wu 1991). The form proposed was

unstable cases

$$S_r = e^{(-\alpha 10/L)}, \qquad (6)$$

stable cases

$$S_r = e^{(-\beta 10/L)}. \qquad (7)$$

The Ku-band mss data do not support the large coefficients ($\alpha = 16.5$, $\beta = 3.1$) suggested by Wu for optical mean-square slope data of Hwang and Schemdin (1988). These values predict very strong slope growth (suppression) with instability (stability). As notably, they suggest a *large* departure between optically derived slope and wind stress response. The solid curve in Fig. 4b is that suggested for C-band (Keller et al. 1989), 45° incidence, scatterometer σ_0 ratio data; having a much smaller value in unstable conditions ($\alpha = 0.50$, $\beta = 2.75$). These values also appear too drastic for the present S_r data. Best fit for the Ku-band altimeter data is $\alpha = 0.17$ and $\beta = 0.47$ (dashed curve) with large scatter that clearly limits our confidence in these values. However, the data do indicate less departure than for the optical and scatterometer results.

The considerable scatter found in Fig. 4 points to the limited size and constraints of our dataset. Further data are needed to confirm or deny the slightly differing responses of altimeter $\mathrm{mss}_{\mathrm{ku}}$ and direct covariance u_* measurements to these nonwind parameters. The main point is that there is not a big divergence between them; nominally less than 15% for a broad range of both surface current and stability conditions.

For atmospheric stability, these data appear to support the idea of enhancement (suppression) with atmospheric instability (stability) beyond that of friction velocity's response, but altimeter-derived u_* has much closer agreement with in situ u_* than was found for scatterometer or optical slope measurements. We note that one primary difference between sensors is that the microwave altimeter is somewhat "blind" to very short-scale gravity capillary waves (Brown 1978), while the scaterometer and optical slope sensor are very sensitive to hem. Thus, previous results (Wu 1991) may imply this narrow gravity–capillary wave regime (waves less than approximately 6-cm wavelength) is more responsive to stratification effects than are the respective integrated slope domains that are thought to dictate altimeter σ_0 Brown 1978) and wind stress (Kitaigorodskii 1973).

4. Concluding remarks

Results of the Ku-band altimeter–in situ wind speed comparisons indicate that MCW-derived altimeter wind peed is most closely related to an adjusted 10-m wind peed, not the true wind speed. Adjusting wind estimates or surface current and atmospheric stability effects proided clear improvement in the wind data comparison. There was a factor of 2 reduction in bias and of 1.6 in ms error. This result is not fully supported or agreed pon in the literature. For example, when developing a tatistical altimeter wind model, Freilich and Challenor 1995) assumed a monotonic relationship between wind peed and σ_0 and also assumed near-surface influences re negligibly small. The present dataset was of limited ize, but collected over a region with strong current and or a fairly broad range of stratification. These local nonwind influences will be present in a global sampling, and our data suggest they will be an error source in satellite altimeter wind speed retrieval.

Perhaps the more fundamental finding is derived from the altimeter–in situ friction velocity comparisons. These measurements indicate that Ku-band altimeter σ_0 is more highly correlated with u_* than with the 10-m wind speed. A single parameter (current, stratification, or other ancillary data not required) mapping between altimeter σ_0 and u_* shows very good agreement for u_* ranging from 0.0 to 0.4 m s^{-1}. A drag coefficient from Wu (1992) and the MCW wind speed algorithm were used for our altimeter–u_* algorithm (3), but we find that the general characteristics of Table 1 hold for other light-to-moderate wind altimeter routines (e.g., Brown et al. 1981) and drag coefficients (e.g., Smith 1988). In summary, these field data suggest that Ku-band altimeter backscatter data would be better used for direct wind stress derivation rather than for wind speed.

Acknowledgments. We thank J. Hare, A. Karachintsev, and G. Young for their help in collecting the *Iselin* data, and T. Donato, J. Kaiser, G. Mormorino, and C. Trump for their help in collecting the *Bartlett* data. We also thank D. Hines and K. Stewart for their work with ROWS. This work was supported by NASA's Physical Oceanography Program Grant 461-31-05 and the Office of Naval Research Grants N00014-92-J-1585 and N00014-94-MP-23031.

REFERENCES

Apel, J. R., 1994: An improved model of the ocean surface wave vector spectrum and its effects on radar backscatter. *J. Geophys. Res.*, **99**, 16 269–16 291.

Brown, G. S., 1978: Backscattering from a Gaussian-distributed perfectly conducting rough surface. *IEEE Trans. Antennas Propag.*, **26**, 472–482.

——, 1979: Estimation of surface wind speeds using satellite-borne radar measurements at normal incidence. *J. Geophys. Res.*, **84**, 3974–3978.

——, H. R. Stanley, and N. A. Roy, 1981: The windspeed measurement capability of spaceborne radar altimetry. *IEEE J. Oceanic Eng.*, **OE-6**, 59–63.

Colton, M., W. J. Plant, W. C. Keller, and G. L. Geernaert, 1995: Tower-based measurements of normalized radar cross section from Lake Ontario: Evidence of wind stress dependence. *J. Geophys. Res.*, **100**, 8791–8813.

Fairall, C. W., E. F. Bradley, D. P. Rogers, J. B. Edson, and G. S. Young, 1996: Bulk parameterization of air–sea fluxes for Tropical Ocean–Global Atmosphere Coupled–Ocean Atmosphere Response Experiment. *J. Geophys. Res.*, **101**, 3747–3764.

Freilich, M. H., and P. G. Challenor, 1995: A new approach for determining fully empirical altimeter wind speed model functions. *J. Geophys. Res.*, **99**, 25 051–25 062.

Geernaert, G. L., and W. J. Plant, Eds., 1990: *Surface Waves and Fluxes.* Vol. I, *Current Theory.* Kluwer Academic, 336 pp.

Glazman, R. E., and A. Greysukh, 1993: Satellite altimeter measurements of surface wind. *J. Geophys. Res.*, **98**, 2475–2483.

Gower, J. F. R., 1996: Intercalibration of wave and wind data from TOPEX/POSEIDON. *J. Geophys. Res.*, **101**, 3817–3829.

Hammond, D. L., R. A. Menella, and E. J. Walsh, 1977: Short pulse radar used to measure sea surface wind speed and SWH. *IEEE J. Oceanic Eng.*, **OE-2,** 61–67.

Hwang, P. A., and O. H. Schemdin, 1988: The dependence of sea surface slope on atmospheric stability and swell conditions. *J. Geophys. Res.*, **93,** 13 903–13 912.

Jackson, F. C., W. T. Walton, B. A. Walter, and C. Y. Peng, 1992: Sea surface mean square slope from Ku-band backscatter data. *J. Geophys. Res.*, **97,** 11 411–11 427.

Keller, W. C., V. Wismann, and W. Alpers, 1989: Tower-based measurements of the ocean C band radar backscattering cross section. *J. Geophys. Res.*, **94,** 924–930.

Kitaigorodskii, S. A., 1973: *The Physics of Air–Sea Interactions.* Keter Press, 237 pp.

Monaldo, F., 1988: Expected differences between buoy and radar altimeter estimates of wind speed and significant wave height and their implications on buoy-altimeter comparisons. *J. Geophys. Res.*, **93,** 2285–2302.

Queffeulou, P., T. Elfouhaily, V. Kerbaol, P. Le Borgne, and J. M. Lefevre, 1996: Remote sensing of wind and waves over the western Mediterranean Sea. *Proc. Second ERS Pilot Project Workshop,* London, United Kingdom, European Space Agency, 47–52.

Smith, S. D., 1988: Coefficients for sea surface wind stress. *J. Geophys. Res.*, **93,** 15 467–15 472.

Stoffelen, A., and D. L. T. Anderson, 1993: ERS-1 scatterometer data characteristics and wind retrieval skill. *Proc. First ERS-1 Symp.* Cannes, France, European Space Agency, 41–47.

Vandemark, D., F. C. Jackson, E. J. Walsh, and B. Chapron, 1994a: Airborne radar measurements of ocean wave spectra and wind speed during the Grand Banks ERS-1 SAR Wave Experiment. *Atmos.–Ocean,* **32,** 143–178.

——, D. Hines, S. Bailey, and K. Stewart, 1994b: Airborne ROWS data report for the High Resolution Experiment, June 1993. NASA Tech. Memo. NASA/TM-104609, 73 pp. [Available from NASA/Goddard Space Flight Center, Greenbelt, MD 20771.]

Weismann, D. E., K. L. Davidson, R. A. Brown, C. A. Friehe, and F. Li, 1994: The relationship between the microwave radar cross section and both wind speed and stress: Model function studies using Frontal Air–Sea Interaction Experiment data. *J. Geophys. Res.*, **99,** 10 087–10 108.

Wentz, F. J., 1992: Measurement of oceanic wind vector using satellite microwave radiometers. *IEEE Trans. Geosci. Remote Sens.*, **30,** 960–972.

Witter, D. L., and D. B. Chelton, 1991: A Geosat altimeter wind speed algorithm and a method for altimeter wind speed algorithm development. *J. Geophys. Res.*, **96,** 8853–8860.

Wu, J., 1991: Effects of atmospheric stability on ocean ripples: A comparison between optical and microwave measurements. *J. Geophys. Res.*, **96,** 7265–7269.

——, 1992: Near-nadir microwave specular returns from the sea surface—Altimeter algorithms for wind and wind stress. *J. Atmos. Oceanic Technol.*, **9,** 659–667.

Direct Covariance Flux Estimates from Mobile Platforms at Sea*

J. B. EDSON, A. A. HINTON, AND K. E. PRADA

Woods Hole Oceanographic Institution, Woods Hole, Massachusetts

J. E. HARE

Cooperative Institute for Research in Environmental Sciences, University of Colorado, Boulder, Colorado

C. W. FAIRALL

Environmental Technologies Laboratory, NOAA, Boulder, Colorado

(Manuscript received 14 December 1995, in final form 22 April 1997)

ABSTRACT

This paper describes two methods for computing direct covariance fluxes from anemometers mounted on moving platforms at sea. These methods involve the use of either a strapped-down or gyro-stabilized system that are used to compute terms that correct for the 1) instantaneous tilt of the anemometer due to the pitch, roll, and heading variations of the platform; 2) angular velocities at the anemometer due to rotation of the platform about its local coordinate system axes; and 3) translational velocities of the platform with respect to a fixed frame of reference. The paper provides a comparison of fluxes computed with three strapped-down systems from two recent field experiments. These comparisons shows that the direct covariance fluxes are in good agreement with fluxes derived using the bulk aerodynamic method. Additional comparisons between the ship system and the research platform *FLIP* indicate that flow distortion systematically increases the momentum flux by 15%. Evidence suggests that this correction is appropriate for a commonly used class of research vessels. The application of corrections for both motion contamination and flow distortion results in direct covariance flux estimates with an uncertainty of approximately 10%–20%.

1. Introduction

In recent years a great deal of attention has been directed toward air–sea interaction as scientists have begun to study environmental issues by properly treating the ocean and atmosphere as a coupled system. This approach has resulted in a number of air–sea interaction studies, which have united scientists from a variety of disciplines. These studies have also forced researchers to address the problems associated with making high-resolution measurements of turbulence statistics at sea. The problems largely arise from three sources: platform motion, flow distortion, and environmental factors unique to the ocean.

Some of the environmental factors that prove troublesome include the contamination of temperature probes by sea spray (Friehe et al. 1975; Larsen et al. 1993) and mechanical failure induced by a combination of corrosion, wave stress, and unavoidable neglect due to infrequent maintenance. Many of these problems have been overcome by the use of the latest generation of sonic anemometers–thermometers. However, sea-spray contamination of fast-response humidity sensors still plagues marine meteorologists. Dual-wavelength infrared hygrometers have shown some promise in combating this problem in recent field experiments. Unfortunately, these devices often present additional problems (e.g., Fairall and Young 1991), which make the development of a reliable fast-response humidity sensors one of the greatest challenges in marine instrumentation.

Attempts have been made to combat the problems of platform motion and flow distortion by choosing indirect measurement techniques that are less sensitive to their contaminating effects. An example of an indirect measurement is the use of the inertial-dissipation method to infer meteorological fluxes from spectral estimates in the inertial subrange (Fairall and Larsen 1986; Fairall et al. 1990). This method is commonly used on research vessels because the inertial subrange estimates are generally uncontaminated by wave-induced motion. The method has also been shown by Edson et al. (1991) to be less sensitive to flow distortion because it is based

---

* WHOI Contribution Number 9126.

Corresponding author address: Dr. James B. Edson, AOP&E Dept., Woods Hole Oceanographic Institution, Bigelow 3, Woods Hole, MA 02543.
E-mail: jedson@whoi.edu

on autovariance statistics rather than covariances (see also Anderson 1993; Yelland et al. 1994).

Unfortunately, the inherent limitations of less direct methods can lead to unsatisfactory flux estimates depending on the project's research objectives. For example, the bulk aerodynamic (e.g., Liu et al. 1979; Large and Pond 1981, 1982; Fairall et al. 1996) and inertial dissipation methods have a disadvantage in that they provide only an estimate of the magnitude of the flux. One can assume that the stress is directed along the streamwise velocity component, but recent studies have shown that this is not necessarily the case and that the difference between the two vectors may be an important indicator of larger-scale forcing (Geernaert 1988). Additionally, recent studies by Davidson et al. (1991), Geernaert et al. (1993), and Rieder et al. (1994) have shown that sea-state parameters such as swell and gradients in the surface currents can also influence the direction of the stress vector. Therefore, it is necessary to compute the vector stress using the eddy correlation technique if the objective of the experiment is to understand directional processes.

Second, both indirect methods must rely on additional parameterizations to account for the interaction between the wave field and the surface fluxes. These parameterizations are presently poorly understood and vary widely depending on the oceanic conditions (e.g., open ocean versus coastal zones), such that direct estimates of the fluxes are necessary if we hope to improve these methods. Since these interactions include those associated with surface slicks, wave–current interactions, and temperature stratification, directional stress estimates must be combined with directional wave spectra, current measurements, oceanic and atmospheric stratification parameters, and surfactant concentrations to examine the functional relationship between the wind forcing and wave state. This is clearly a difficult task but one that will become less daunting with the data collected during several field experiments, one of which is briefly discussed in section 6.

Direct covariance (or eddy correlation) measurements generally require an experimental setup around a platform that removes or minimizes the aforementioned effects. One such experimental design is the use of a fixed structure (such as a shallow-water tower) to eliminate platform motion. The sensors are then mounted on low profile masts or booms to move them away from the distorted flow near the platform. This approach was used during the Humidity Exchange over the Sea Main Experiment (HEXMAX), where eddy correlation (or direct covariance) flux estimates were made on a boom extending 17 m upwind of a research platform (Oost et al. 1994). The obvious disadvantage to this approach is that these fixed platforms are relatively scarce and are generally limited to shallow water, and it is often difficult to reduce the flow distortion to satisfactory levels.

Still another approach is to start with a low profile platform, moored buoy (e.g., Dugan et al. 1991; Anctil et al. 1994), or mast, and then correct for platform motion by carefully measuring this motion relative to some reference frame. The systems required to make these measurements generally use a combination of radial and linear accelerometers, compasses, and gyros. These sensors can either be mounted on a stabilized subplatform that has sufficiently slow response to motion or they can be strapped down to the main platform. Signals from both these types of systems are processed in various ways to ultimately produce an estimate of the platform's velocity at the measurement location. Further processing of these signals can be used to estimate the position of the platform relative to the sea surface.

This paper describes our recent efforts to directly measure turbulent fluxes and statistics at sea from mobile platforms using the latter approach. In sections 2–5 we examine the methods used to compute the mean and turbulent meteorological statistics from moving platforms at sea. This involves a detailed description of the methods for obtaining the necessary correction terms using either a strapped-down or gyro-stabilized system. In section 6 we provide a discussion of the results obtained from two strapped-down systems deployed during the High Resolution experiment (Herr et al. 1991). This section describes the system components in some detail and gives examples of the velocity measurements before and after correction to illustrate the effects of motion contamination. The section concludes with a comparison of the eddy correlation derived fluxes with bulk aerodynamic derived estimates.

2. Direct covariance flux systems

The time-averaged flux determined using the eddy correlation technique is regarded as the most direct estimate of the ensemble average flux. In the field, a sonic anemometer is commonly used to provide the three velocity measurements required to compute the vector stress

$$\tau = -\rho[\mathbf{i}\langle u'w'\rangle + \mathbf{j}\langle v'w'\rangle], \tag{1}$$

where ρ is the density of air, the brackets denote a time average, and u', v', and w' are the longitudinal, lateral, and vertical velocity fluctuations about their means. In (1), $-\langle u'w'\rangle$ represents the longitudinal (along wind) component of the stress, and $-\langle v'w'\rangle$ is the lateral component.

The corrected vertical velocity can also be correlated with scalar quantities to compute their vertical flux. In particular, meteorologists are interested in computing the sensible and latent heat fluxes,

$$H = \rho c_p\langle w'\theta'\rangle \tag{2}$$

$$E = \rho L_e\langle w'q'\rangle, \tag{3}$$

respectively, where c_p is the specific heat of air at constant pressure, L_e is the latent heat of evaporation of water, and θ' and q' denote fluctuations in potential temperature and specific humidity, respectively. These fluxes can then be combined with estimates of the surface stress to compute atmospheric stability parameters.

The obvious problem that arises when estimating these fluxes from a moving platform is that part of the fluctuating velocity is due to platform motion. This motion contamination must therefore be removed before we can compute the fluxes. The contamination arises from three sources: 1) instantaneous tilt of the anemometer due to the pitch, roll, and heading variations of the platform; 2) angular velocities at the anemometer due to rotation of the platform about its local coordinate system axes; and 3) translational velocities of the platform with respect to a fixed frame of reference (Hare et al. 1992).

A variety of approaches have been used to correct wind sensors for platform motion. True inertial navigation systems (Axford 1968; Lenschow and Spyers-Duran 1987) are standard for research aircraft. These systems are expensive and subject to the so-called Schuler oscillation, so simpler techniques have been sought for ships where the platform mean vertical velocity is unambiguously zero. The basic approach that we are using follows that of Fujitani (1981), where the true wind vector (i.e, uncontaminated by motion) can be written as

$$\mathbf{V}_{\text{true}} = \mathbf{T}\mathbf{V}_{\text{obs}} + \boldsymbol{\Omega} \times \mathbf{T}\mathbf{M} + \mathbf{V}_{\text{CM}}, \tag{4}$$

where $\mathbf{V}_{\text{true}}$ is the desired wind velocity vector in the reference coordinate system, $\mathbf{V}_{\text{obs}}$ is the measured wind velocity vector in the platform frame of reference, $\mathbf{T}$ is the coordinate transformation matrix for a rotation of the platform frame coordinate system to the reference coordinates, $\boldsymbol{\Omega}$ is the angular velocity vector of the platform coordinate system, $\mathbf{M}$ is the position vector of the wind sensor with respect to the center of gravity, and $\mathbf{V}_{\text{CM}}$ is the translational velocity vector at the center of motion of the platform with respect to a fixed coordinate system.

If the motion measurement system is not located at the center of motion, then an additional correction term arises due to angular velocities that are sensed at that location as translational velocities by the accelerometers (Fujitani 1985). This term is incorporated in (4) as

$$\mathbf{V}_{\text{true}} = \mathbf{T}\mathbf{V}_{\text{obs}} + \boldsymbol{\Omega} \times \mathbf{T}(\mathbf{M} - \mathbf{S}) + \mathbf{V}_{\text{mot}}, \tag{5}$$

where $\mathbf{S}$ is the vector distance from the motion system to the center of motion of the platform and $\mathbf{V}_{\text{mot}}$ now includes the additional translational velocities. Fortunately, $\mathbf{M} - \mathbf{S}$ is just the position vector of the wind sensor with respect to the motion package. Therefore, one does not need to know the exact location of the center of motion, which is often difficult to identify.

3. Angles and angular rates

To use (5), we need three angular variables describing the platform's orientation in the fixed frame and the angular velocity vector describing the time rate of change of its orientation. Several different angular coordinate systems are available (Goldstein 1965), but roll ϕ, pitch θ, and yaw Ψ are most often used because they are the variables output from common doubly gimbaled gyro-stabilized systems. In the sections that follow, we will describe two common approaches to compute these variables from moving platforms.

a. Gyro-stabilized systems

Gyro-stabilized systems provide the user with pitch, roll, and yaw angles that describe the ship's orientation in the fixed frame. These angles can be used directly in the total rotational coordinate transformation matrix that we define as

$$\begin{aligned}
&(\phi, \theta, \Psi) \\
&= A(\Psi)A(\theta)A(\phi) \\
&= \begin{bmatrix} \cos(\Psi) & \sin(\Psi) & 0 \\ -\sin(\Psi) & \cos(\Psi) & 0 \\ 0 & 0 & 1 \end{bmatrix} \begin{bmatrix} \cos(\theta) & 0 & \sin(\theta) \\ 0 & 1 & 0 \\ -\sin(\theta) & 0 & \cos(\theta) \end{bmatrix} \begin{bmatrix} 1 & 0 & 0 \\ 0 & \cos(\phi) & -\sin(\phi) \\ 0 & \sin(\phi) & \cos(\phi) \end{bmatrix}, \\
&= \begin{bmatrix} \cos(\Psi)\cos(\theta) & \sin(\Psi)\cos(\phi) + \cos(\Psi)\sin(\theta)\sin(\phi) & -\sin(\Psi)\sin(\phi) + \cos(\Psi)\sin(\theta)\cos(\phi) \\ -\sin(\Psi)\cos(\theta) & \cos(\Psi)\cos(\phi) - \sin(\Psi)\sin(\theta)\sin(\phi) & -\sin(\theta)\cos(\phi)\sin(\Psi) - \sin(\phi)\cos(\Psi) \\ -\sin(\theta) & \cos(\theta)\sin(\phi) & \cos(\theta)\cos(\phi) \end{bmatrix}, \quad (6)
\end{aligned}$$

nere the sign convention here is based on a right-nded (x, y, z) coordinate system with x positive for-rd (to bow), y positive to port, z positive upward, Ψ sitive for the ship's bow yawed clockwise from north, ϕ positive for the port side rolled up, and θ positive for the bow pitched down. Note that ϕ and θ are right-handed rotations, but to conform to the normal convention for heading, we have used a left-handed defion for Ψ. This definition allows us to directly use platform's compass in the transformation matrix.

quation (6) represents the coordinate system trans- m for a combination of the three separate rotations the platform coordinate frame about the three axes our frame of reference (i.e., the earth). Note that this al coordinate transformation matrix is dependent on order of the three separate rotations. However, for all roll and pitch angles such as those encountered a large research vessel or discus buoy in the ocean vironment (perhaps ±10°), the error due to the order rotation is negligible. On smaller vessels such as the wed catamaran described in section 6, the errors as- ciated with the order of rotation are minimized by the 2, 1 rotation used in (6). Additionally, these errors main small simply because the catamaran cannot be perated in high sea states, such that the angles rarely xceed ±10°.

The three angular rates can be computed from the ime derivatives of the orientation angles. Unfortunately, nly yaw is measured in the fixed frame, pitch is mea- ured in a yawed frame, and roll is measured in a pitched nd yawed frame. Thus, the time derivatives of these angles must be rotated to create a fixed frame angular rate pseudovector given by

$$\mathbf{\Omega} = \begin{bmatrix} 0 \\ 0 \\ -\dot{\Psi} \end{bmatrix} + A(\Psi)\begin{bmatrix} 0 \\ \dot{\theta} \\ 0 \end{bmatrix} + A(\Psi)A(\theta)\begin{bmatrix} \dot{\phi} \\ 0 \\ 0 \end{bmatrix}$$

$$= \begin{pmatrix} \dot{\phi}\cos(\Psi)\cos(\theta) + \dot{\theta}\sin\Psi \\ \dot{\theta}\cos(\Psi) - \dot{\phi}\sin(\Psi)\cos(\theta) \\ -\dot{\Psi} - \dot{\phi}\sin(\theta) \end{pmatrix}, \qquad (7)$$

where the overdot denotes a time derivative. This vector can then be used in either (4) or (5) to compute the required angular velocities.

b. Strapped-down systems

As an alternative to gyro-stabilized pitch and roll sensors, it is also common practice to use angular rate sensors that measure the rate of angular rotation about the three axes in the platform frame. These systems are often referred to as strapped-down systems because the motion package is firmly attached to the platform frame. In such systems, the angular rate vector is given by

$$\mathbf{\Omega}_{\text{obs}} = \begin{pmatrix} \dot{\phi}_{\text{obs}} \\ \dot{\theta}_{\text{obs}} \\ -\dot{\Psi}_{\text{obs}} \end{pmatrix}, \qquad (8)$$

where the subscript obs again denotes measurements made in the platform's frame of reference. We remind the reader that the yaw rate is defined positive for a left-handed rotation. The negative sign in front of the yaw rate is therefore required to compute the angular velocities in our otherwise right-handed coordinate system. We feel that the small amount of confusion that this introduces is more than offset by the ease in which the platform's heading is introduced into the corrections. This vector can be related to the fixed frame angular rate through

$$\mathbf{\Omega} = \mathbf{T}\mathbf{\Omega}_{\text{obs}}. \qquad (9)$$

This relationship allows one to rewrite (5) using our direct measurements of angular rate in the platform frame as

$$\mathbf{U}_{\text{true}} = \mathbf{T}(\mathbf{U}_{\text{obs}} + \mathbf{\Omega}_{\text{obs}} \times \mathbf{R}) + \mathbf{V}_{\text{mot}}, \qquad (10)$$

where **R** is the position vector of the wind sensor with respect to the motion package.

The difficulty then is to approximate ϕ, θ, and Ψ from the strapped-down angular rate sensors. The general approach is to use (6) and (7) in (9) to obtain an expression for the time derivative of these angles in terms of the measured angular rates given by

$$A(\Psi)A(\theta)A(\phi)\begin{bmatrix} \dot{\phi}_{\text{obs}} \\ \dot{\theta}_{\text{obs}} \\ -\dot{\Psi}_{\text{obs}} \end{bmatrix}$$

$$= \begin{bmatrix} 0 \\ 0 \\ -\dot{\Psi} \end{bmatrix} + A(\Psi)\begin{bmatrix} 0 \\ \dot{\theta} \\ 0 \end{bmatrix} + A(\Psi)A(\theta)\begin{bmatrix} \dot{\phi} \\ 0 \\ 0 \end{bmatrix}. \qquad (11)$$

Using the coordinate system defined above, a few algebraic manipulations result in the following expression:

$$\begin{bmatrix} \dot{\phi} \\ \dot{\theta} \\ -\dot{\Psi} \end{bmatrix} = \begin{pmatrix} \dot{\phi}_{\text{obs}} + [-\dot{\Psi}_{\text{obs}}\cos(\phi) + \dot{\theta}_{\text{obs}}\sin(\phi)]\tan(\theta) \\ \dot{\theta}_{\text{obs}}\cos(\phi) + \dot{\Psi}_{\text{obs}}\sin(\phi) \\ [-\dot{\Psi}_{\text{obs}}\cos(\phi) + \dot{\theta}_{\text{obs}}\sin(\phi)]/\cos(\theta) \end{pmatrix}, \qquad (12)$$

which we can rewrite using small angle approximations as

$$\begin{bmatrix} \dot{\phi} \\ \dot{\theta} \\ -\dot{\Psi} \end{bmatrix} \approx \begin{pmatrix} \dot{\phi}_{\text{obs}} - \dot{\Psi}_{\text{obs}}\theta \\ \dot{\theta}_{\text{obs}} + \dot{\Psi}_{\text{obs}}\phi \\ -\dot{\Psi}_{\text{obs}} + \dot{\theta}_{\text{obs}}\phi \end{pmatrix}. \qquad (13)$$

In principle, (12) could be integrated by updating this matrix with successive approximation of ϕ and θ as one stepped through the measurements. In practice, problems often arise with this approach due to the drift found in angular rate sensors. Therefore, the angles are generally found by high-pass filtering the angles that are computed by integration of (12) or (13) and then adding these results to low-pass filtered reference angles. This is the approach taken by Fairall et al. (1997) and Thwaites et al. (1995).

c. Complementary filtering

The Woods Hole Oceanographic Institution (WHOI) system uses a slightly simpler approach based on complementary filtering. In a strapped-down system, the measured accelerometer output is a combination of the gravitational component due to the pitching and rolling of the platform (i.e., due to tilting of the system) plus the accelerations arising from the motion of the platform along the accelerometer axes

$$\begin{pmatrix} \ddot{x}_{\text{obs}} \\ \ddot{y}_{\text{obs}} \\ \ddot{z}_{\text{obs}} \end{pmatrix} = \begin{pmatrix} \ddot{x} \\ \ddot{y} \\ \ddot{z} \end{pmatrix} + \begin{pmatrix} -g \sin(\theta) \\ g \sin(\phi) \cos(\theta) \\ g \cos(\phi) \cos(\theta) \end{pmatrix}, \tag{14}$$

where the double dots denote second derivatives of the position vector $\mathbf{X} = (x, y, z)$, and g is the gravitational acceleration.

The second term on the right-hand side of (14) represents the tilt-induced acceleration. These tilt-induced accelerations will eventually have to be removed before we integrate our accelerometers to compute the platform velocities as described in section 4. However, we can use these measured accelerations and angular rates to approximate the desired angles using complementary filtering.

We can easily illustrate this technique using Laplace transform notation, where we estimate ϕ, θ, and Ψ by applying filters to our signals to obtain

$$\phi \approx \frac{1}{\tau s + 1} \frac{\ddot{y}_{\text{obs}}}{g} + \frac{\tau s}{\tau s + 1} \phi_{\text{obs}} \tag{15}$$

$$\theta \approx \frac{1}{\tau s + 1} \frac{\ddot{x}_{\text{obs}}}{g} + \frac{\tau s}{\tau s + 1} \theta_{\text{obs}} \tag{16}$$

and

$$\Psi \approx \frac{1}{\tau s + 1} \Psi_{\text{slow}} + \frac{\tau s}{\tau s + 1} \Psi_{\text{obs}}, \tag{17}$$

where s represents the differentiation operator such that $\dot{\phi}_{\text{obs}} = s\phi_{\text{obs}}$, τ is a time constant, Ψ_{slow} represents the compass output, and we have again assumed that these angles are small in (15) and (16). The first term on the right-hand side is the low-frequency tilt reference from the accelerometers as follows from (14). The second term on the right-hand side represents a high-pass filter [i.e., $\tau s/(\tau s + 1)$] that integrates the angular rate sensors to provide the wave-induced angular motions. By filtering the signals in this way we do not introduce any time delays, that is, the process is an all-pass filter that removes the unwanted drift in the rate gyros while reaining the low-frequency tilt reference.

In practice, these expression can be rewritten in the orm

$$\phi \approx \frac{1}{\tau s + 1} \left[\tau \dot{\phi}_{\text{obs}} + \frac{\ddot{y}_{\text{obs}}}{g} \right], \tag{18}$$

o that we can compute the angles by performing an FFT on the bracketed expressions, applying the above first-order Butterworth filter in frequency space, and then performing an inverse FFT to obtain the time series of ϕ, θ, and Ψ. Alternatively, we have computed the angles using a digital filter on the time series such that

$$\begin{aligned} \phi(t) \approx {} & B_1 \left[\tau_c \dot{\phi}(t)_{\text{obs}} + \frac{\ddot{y}(t)_{\text{obs}}}{g} \right] \\ & + B_0 \left[\tau_c \dot{\phi}(t - \Delta t)_{\text{obs}} + \frac{\ddot{y}(t - \Delta t)_{\text{obs}}}{g} \right] \\ & + A_1 \phi(t - \Delta t), \end{aligned} \tag{19}$$

where Δt is the time step between samples, τ_c is the filter time constant given by

$$\tau_c = \frac{\Delta t}{2\omega_c}, \tag{20}$$

where ω_c is the prewarped frequency

$$\omega_c = \tan\left(\frac{\Delta t}{2\tau}\right) \tag{21}$$

and the filter coefficients are given by Hamming (1977) as

$$A_1 = \frac{1 - \omega_c}{1 + \omega_c}, \qquad B_0 = B_1 = \frac{\omega_c}{1 + \omega_c}. \tag{22}$$

While both techniques give essentially the same results, the latter approach may turn out to be more attractive since one could design an analog system that filters the combined signals before they reach the data acquisition computer. This would allow the angles to be computed in real time, without any loss of data (after a short spinup period) and less computational processing. The digital filter approach is used to compute the flux estimates presented in section 6.

The choice of the time constant τ is dependent on how the platform responds to the wave field. During the High Resolution Main Experiment, our spectra showed that the peak in the accelerometer spectra generally occurred around $f_n = 0.2$–0.25 Hz, that is, the platforms were responding strongly to 4–5-s waves. Since the accelerometers are sensing both platform and tilt-induced accelerations about this maximum, it is necessary to use a much longer time constant to obtain the low-frequency tilts. In practice, we have found that a value of τ equal to $5/(2\pi f_m)$ provides a smooth transition between the spectral components as shown in Fig. 1.

4. Translational velocities

Historically, instruments that measure absolute velocities have not been available (differential GPS may soon change this). As a result, velocities are usually computed by integrating measurements of platform acceleration after removal of the tilt-induced components discussed in section 3c. The removal of all traces of the

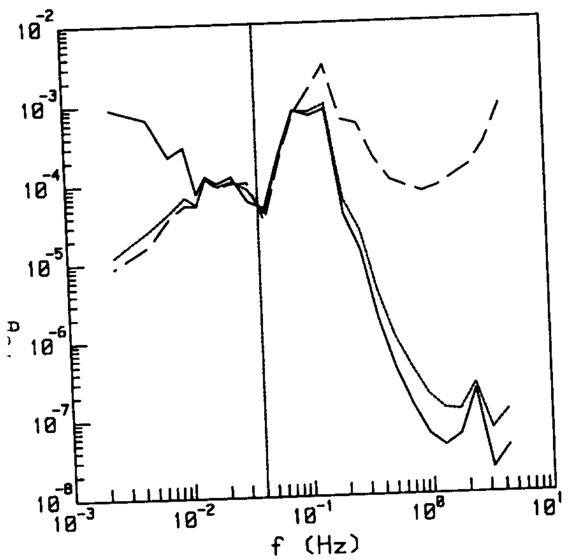

IG. 1. The variance spectra of our angular estimates of θ. The ken line is computed from $-x/g$, the solid line is computed from ime series of the integrated rate sensor, and the dotted line is nputed using complementary filtering. The vertical line in the fig- shows the location of our cutoff frequency $f_m/5$.

it-induced components in our measured accelerations a difficult task. Additionally, ship maneuvers require ccurate measurements of the low-frequency transla- onal velocity that can be difficult to obtain from the ntegrated accelerations. Therefore, we again rely on iltering to provide us with the high- and low-frequency ranslational velocity components.

To illustrate this process, we rewrite the translational elocity as

$$\mathbf{V}_{\rm mot} = \mathbf{V}_{\rm lp} + \mathbf{V}_{\rm hp}, \tag{23}$$

where we have divided the translational velocities into low-pass (lp) and high-pass (hp) components. In the strapped-down systems, the high-pass components are computed by rotating the accelerations into the fixed frame using the transformation matrix $\mathbf{T}(\phi, \theta, \psi)$, subtracting the gravity vector, high-pass filtering and integrating the remainder, and then high-pass filtering the resultant velocities,

$$\mathbf{V}(t)_{\rm hp} = {\rm Hp}\left[\int [{\rm Hp}(\mathbf{T}\ddot{\mathbf{x}}(t)_{\rm obs} + \mathbf{g})]\,dt\right], \tag{24}$$

where Hp represents a high-pass filter operator and $\mathbf{g} = (0, 0, -g)$. The same expression applies for the gyro-stabilized velocities except that the gyro-stabilized accelerometers need only be rotated to account for any change in heading before subtraction of gravity. This high-passed component represents the wave-induced motions of the anemometer where we typically use a time constant of 2 min for the filter.

The low-pass components are computed only for the horizontal velocities (i.e., we assume the platform does not leave the ocean surface) using either GPS or a current meter that measures the platform speed relative to water. The combination of the high-pass and low-pass signals results in a value of $\mathbf{V}_{\rm mot}$ that describes the mean velocity platform relative to earth (measured with a GPS system) or relative to water (measured with a current meter) plus the fluctuating velocity components computed from our accelerometers. The method used to compute the low-frequency component depends on whether we are using real-time or postprocessing of the data as described below.

5. Data processing

For real-time processing we use simple exponential time filters and compute fluxes in 10-min blocks. These simple filters introduce a time lag that must be taken into account before the high-pass platform velocities are added to transformed velocities in (10). The mean translational motion of the platform is computed over the 10-min period and then added to the otherwise corrected velocities at the end of the averaging period (i.e., the low-pass time constant is 10 min). The averages, variances, and covariances are then computed and displayed at the end of each averaging period. This allows us to check the system performance during the cruise.

A flowchart for the postprocessing procedure is given in Fig. 2, which is intended to summarize the process described above. In this procedure we first remove any mean in our angular rate time series when the angles are found from complementary filtering. This step helps offset the gentle roll-off of our first-order Butterworth filters and gives us more flexibility in choosing the cutoff frequency $1/\tau$. We then use time-symmetric high-pass filters to avoid time lags in our translational velocities and apply the low-pass filtered GPS or current meter data at every time step. In this instance, the low-pass time constant is chosen to compliment the high-pass filter.

The relative velocity components obtained from our current meters are rotated by the transformation matrix to give the north and west components. When these are added from the north and west components of the wind speed relative to the platform we obtain the wind velocity relative to the water,

$$\mathbf{U}^{\rm water}_{\rm true} = \mathbf{T}(\mathbf{U}_{\rm obs} + \mathbf{\Omega}_{\rm obs} \times \mathbf{R}) + \mathbf{V}_{\rm hp} + {\rm Lp}[\mathbf{T}\mathbf{V}_o], \tag{25}$$

where $\mathbf{V}_o$ is the platform velocity relative to water and Lp represents a low-pass filter operator. Equation (25) provides us with the relative velocity used in our bulk flux algorithm. The GPS system is used to directly compute the north and west components of the ship speed relative to earth. These are then used to compute the north and west components of the wind velocity relative to earth:

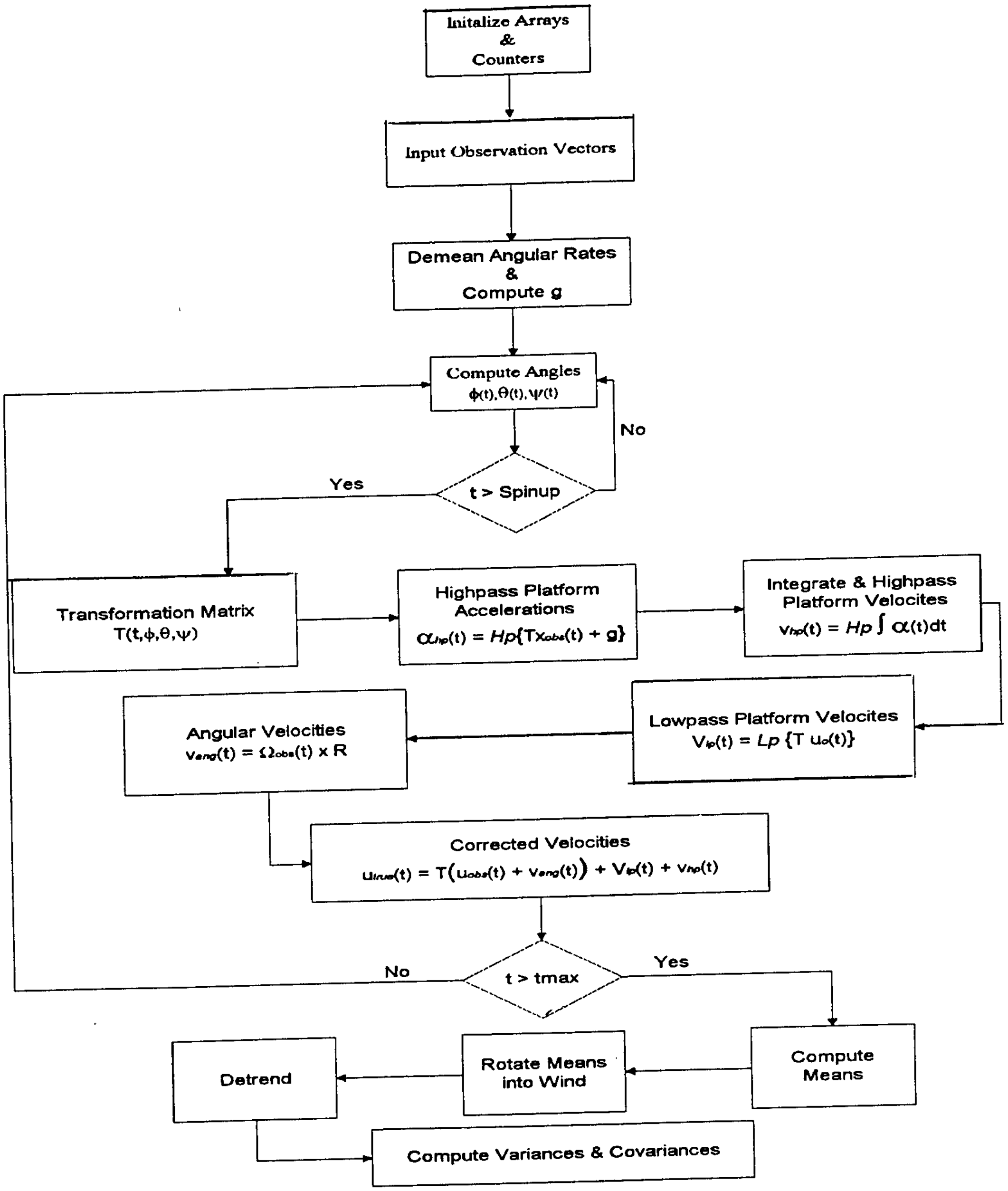

FIG. 2. A flowchart of the method used to postprocess the data. Spinup represents the time given to the complementary filters to provide the proper angles, while $t_{\max}$ represents the record length.

$$\mathbf{U}_{\mathrm{true}}^{\mathrm{earth}} = \mathbf{T}(\mathbf{U}_{\mathrm{obs}} + \mathbf{\Omega}_{\mathrm{obs}} \times \mathbf{R}) + \mathbf{V}_{\mathrm{hp}} + \mathrm{Lp}[\mathbf{V}_{\mathrm{GPS}}]. \tag{26}$$

The wind components relative to earth are then used to compute the wind direction by taking the four quadrant arctangents of the negative north (i.e., south) and west components to determine where the wind is coming from in earth coordinates. The velocity of the ship relative to water and the ship relative to earth are then combined to compute the actual value of the near-surface current.

The velocities in these two coordinates systems are generally rotated into the streamwise wind (i.e., $\overline{V} = \overline{W} = 0$ after rotation) and linearly detrended by removing a least squares fit to the rotated velocities. The fluxes are then computed in the along-wind and cross-wind directions. However, the north and west components of the fluxes are sometimes computed, particularly when we want to map the flux field over a survey cruise. For example, this approach would be desirable if we wished to examine the curl of the stress vector to study upwelling.

Finally, it is worth noting that our stress values tend to be invalidated by drastic platform maneuvers, which add low-frequency noise to the flux cospectra. In fact, our real-time stress estimates tend to be invalidated by even modest platform maneuvers because the low-pass filter in the real-time processing is essentially a 10-min block average. Therefore, the preferred mode of operation is to take measurements under way at a constant speed and heading whenever possible. In postprocessing the data, however, our algorithms are able to correct for heading changes. The data given in section 6 are taken from the postprocessed flux estimates, where the mean relative wind direction was limited to ±90° from the bow.

6. Discussion of results

In the discussion that follows, we will focus on measurements made using the WHOI flux system during the High Resolution and Marine Boundary Layers (MBLs) experiments. Results from the system deployed by NOAA's Environmental Technology Laboratory can be found in Fairall et al. (1997). The High Resolution program is an Office of Naval Research (ONR)-sponsored Accelerated Research Initiative that was designed to investigate surface signatures in radar backscatter measurements in and around the Gulf Stream. This region was selected because the gradients associated with sea surface temperature and current fronts often give rise to roughness contrasts that cause the features seen in remotely sensed images. In these regions it is especially important to compute the fluxes in a frame of reference moving with the ocean surface. This is because the momentum flux, at least in a bulk sense, is proportional to the relative difference between the wind and current velocities.

The MBL experiment was another ONR-sponsored research program that took place off the California coast. The experiment was conducted from research vessels, an aircraft, and the research platform *FLIP*. The R/P *FLIP* is a 110-m-long spar buoy that provides a relatively stable platform for ocean-going research (particularly when compared with research vessels). The meteorological measurements made aboard the *FLIP* used a low profile mast erected off its port boom. Comparisons between the *FLIP* data and flux estimates taken aboard the research vessel are used to investigate the influence of flow distortion on our measurements.

a. The WHOI direct covariance flux system

The WHOI Direct Covariance Flux System (DCFS) has been deployed in two recent field experiments on three platforms. Two ship-based systems have been on bow masts aboard the R/V *Columbus Iselin* during the High Resolution Main Experiment and from the R/V *Wecoma* during the MBL experiment. Additionally, a DCFS was deployed aboard the laser slope gauge, acoustic Doppler current profiler, Attitude measurement unit, sonic anemometer (*LADAS*) catamaran that was towed from the R/V *Columbus Iselin,* as shown in Fig. 3. The *LADAS* has been developed to allow us to study a wide range of microscale and mesoscale processes within the oceanic and atmospheric boundary layers by integrating several systems on a single platform. The catamaran is remotely "flown" outside of the wake of the research vessel, with power and signals going to and from the vessel by way of the towing cable. The platform is designed to collocate the probes as much as possible so as to study cause and effect on very fine spatial and temporal scales, while making the platform itself much less obtrusive to the environment than previous ocean-going platforms. The catamaran has additional advantages over buoys in that it is highly mobile and is not limited by power consumption restraints.

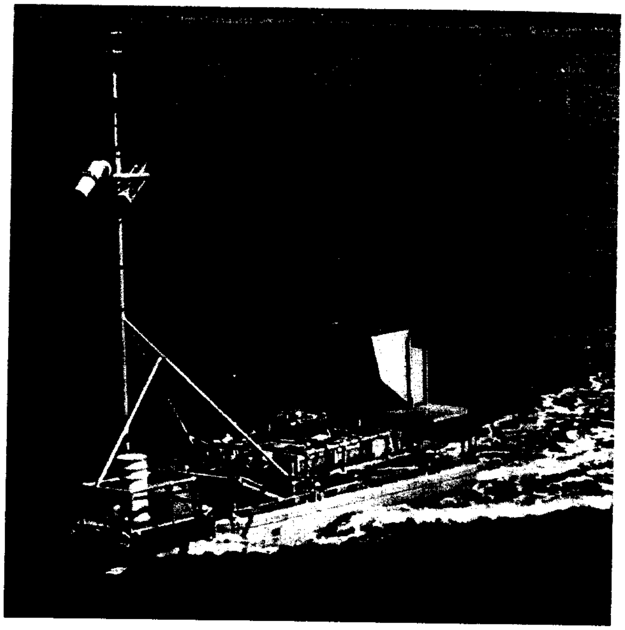

FIG. 3. The R/P *LADAS* catamaran. The sonic anemometer is mounted on the mast above the starboard pontoon. The Honeywell AMU was located in one of the splash-proof containers near the center of the catamaran.

The 1993 High Resolution Main Experiment was conducted off Cape Hatteras in and around the Gulf Stream. The primary objective of these experiments was to examine the relationship between microwave remote sensing, meteorological forcing, and oceanic surface processes. In this regard, the scientific team instrumenting the R/P *LADAS* was most interested in making accurate measurements of the meteorological forcing through wind stress and the short-wave component of the wave spectrum, which is the primary source for microwave backscatter from the ocean surface. The system used to measure the short-wave spectra is described in detail by Bock and Hara (1995).

The meteorological package aboard all three platforms consisted of a Solent three-axis sonic anemom-

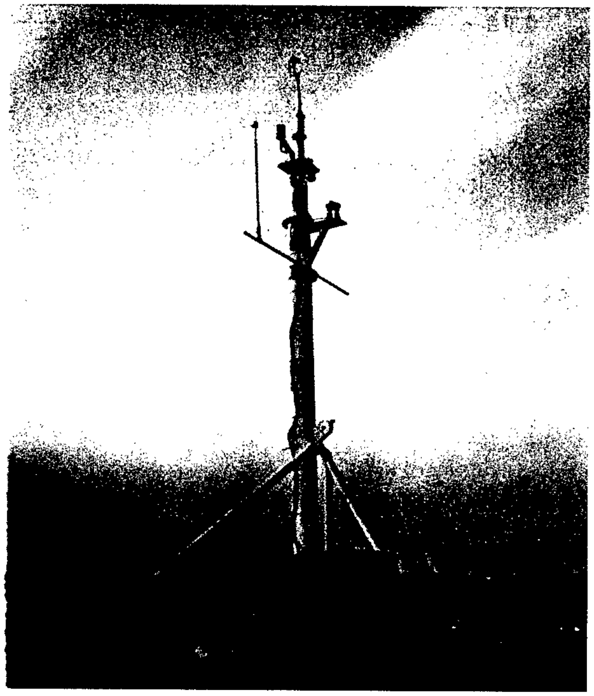

FIG. 4. The Direct Covariance Flux System used aboard the R/Vs lin and *Wecoma.* The anemometer is mounted directly above the tal canister that houses the MotionPAK AMU sensors. The sensor unted horizontally below the canister is an Ophir infrared hy- meter. The antenna for the GPS receiver integrated into the system visible on the horizontal crosspiece.

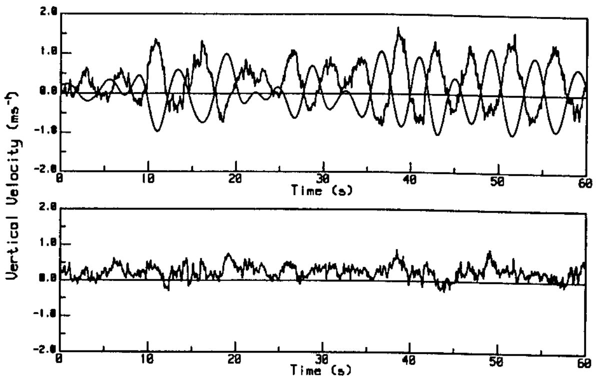

FIG. 5. The top panel shows a time series of the measured sonic vertical velocity (solid line) with the high-passed vertical velocity correction $W_{hp}(t)$. The bottom panel shows the true vertical velocity computed from Eq. (10).

er–thermometer and a Väisälä relative humidity–tem- rature sensor with a radiation shield. The sonic ane- ometer and Väisälä units were deployed 5.6, 11.5, and .3 m above the mean sea surface on the R/P *LADAS,* V *Iselin,* and R/V *Wecoma,* respectively. The ship- sed systems also included an Ophir infrared hygrom- er in order to make direct estimates of the latent heat x, as shown in Fig. 4.

The R/P *LADAS* used a Honeywell MK 50 Attitude easurement Unit (AMU) to provide the three axes gular rates and linear accelerations needed to correct various measurement systems onboard. The AMU strapped down near the center of mass of the cata- ran, which was 5.3 m away from the sonic sampling lume. The R/P *LADAS* computed the mean velocity ative to water using a SimTronix UCM 40 three-axis rrent meter provided by Johns Hopkins Applied Phys- Laboratory. The current meter also contained a com- ss to provide heading and a temperature probe for the ar sea surface temperature. The current meter was ployed approximately 1 m forward and between the amaran's pontoons at a depth of 1 m.

The ship-based DCFS used the three-axis acceler- eters and rate sensors provided by a Systron Donner otionPAK. The MotionPAK was mounted directly be- ath the sonic anemometer package, which decreased distance between the sensors and the sonic sampling lume to $|\mathbf{R}| \approx 1$ m in (10), as shown in Fig. 4. The R/V *Iselin* used the ship's gyrocompass to obtain heading, while the R/V *Wecoma* system incorporated a Precision Navigation compass. A hull-mounted ADCP provided the relative velocity for both ships using the uppermost bins of the ADCP data. A temperature probe was dragged off the side of the ships to provide the DCFS with a continuous record of near-surface temperature.

b. Platform contamination

A segment of a uncorrected sonic vertical velocity time series taken from the R/V *Iselin* is shown in Fig. 5 along with the computed velocity correction. Obviously most of the fluctuating signal seen by the anemometer in this time series is platform motion. This figure also indicated that a mean vertical velocity remains even after correction. The residual tilt varies from approximately 3° to 5° for relative wind directions from 0° (i.e., toward the bow) to ±90° (from port or starboard). The residual tilt on the R/P *LADAS* is always less than 1° for the relative wind directions used in this analysis. We believe that the larger residual tilt is due to flow distortion by the vessel's superstructure and provide evidence for this in section 5d.

The corresponding vertical velocity spectra are shown in Fig. 6, where the motion is apparent as a spike at about 0.25 Hz in the uncorrected spectrum. This figure shows that this spike is effectively removed after the correction procedure has been applied. The low-frequency changes in the velocity spectra are due to the instantaneous tilt corrections, which add components of the other two velocity measurements, as well as the low-frequency translational motion of the platform (only the mean was removed from the uncorrected time series).

The effect of motion contamination in our flux estimates can be examined in detail using the cospectral equivalent of (1). The cospectral estimates of the stress components are shown in Figs. 7 and 8. The uncorrected components are clearly contaminated by a spike in the

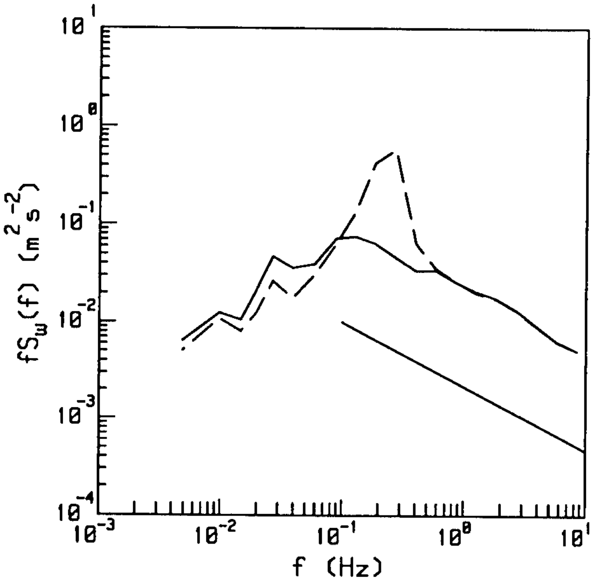

FIG. 6. The measured (broken line) and corrected (solid line) vertical velocity power spectra. The spectra are computed from the average of three 3-min time series within a 10-min record. The straight line in the figure represents the expected −2/3 slope in the inertial subrange.

cospectra occurring at the frequency f_m. This spike dominates the signal and results in a positive values of the longitudinal momentum fluxes when we integrate under the curve. However, when we remove the platform contamination from our signals we obtain cospectra that agree well with empirical predictions. An example of this is shown in Fig. 9 where we have plotted the corrected a *uw* cospectrum versus the empirical formula determined by Kaimal et al. (1972).

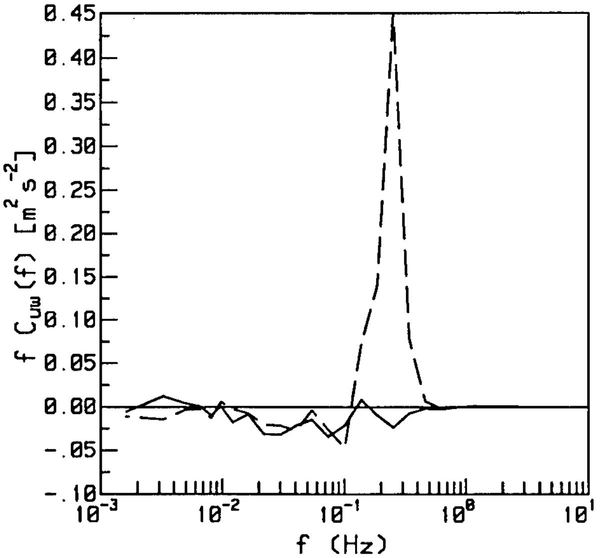

FIG. 7. The uncorrected (broken line) and corrected (solid line) covariance spectra for the longitudinal component of the momentum flux.

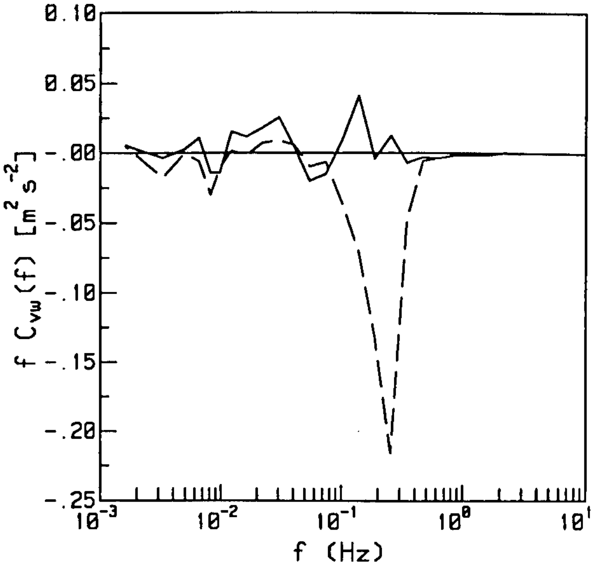

FIG. 8. The uncorrected (broken line) and corrected (solid line) covariance spectra for the lateral component of the momentum flux.

c. Flux comparisons

The mean instrumentation was used to compute the fluxes using the bulk aerodynamic method, which served as a useful means to compare our flux estimates. The bulk aerodynamic flux estimates are determined using an algorithm given in Fairall et al. (1996) that combines the surface roughness parameterization from Smith (1988) with the heat flux parameterizations described by Liu et al. (1979). In Figs. 10–13, the uncorrected and corrected covariance stress estimates are

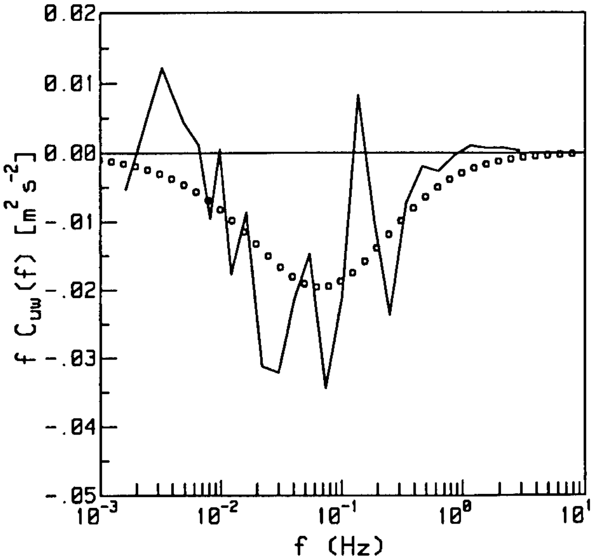

FIG. 9. The corrected (solid line) covariance spectra for the longitudinal component of the momentum flux plotted with a parameterization of this component (dotted line) reported in Kaimal et al. (1972).

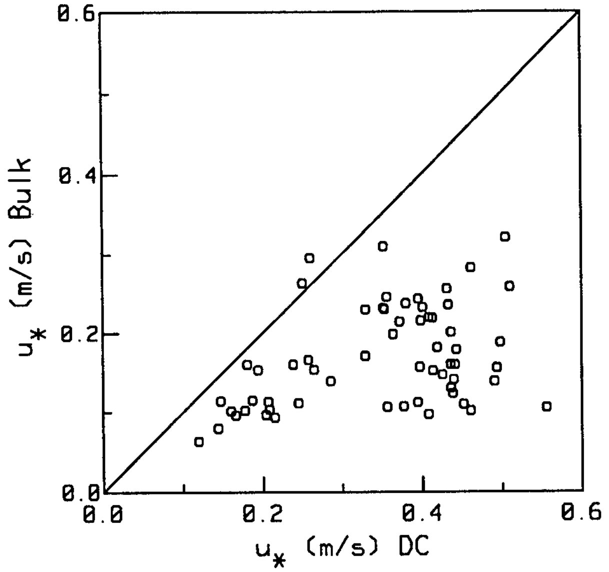

FIG. 10. A comparison of the uncorrected friction velocity estimates from the R/P *LADAS* computed from Eq. (27) vs our bulk aerodynamic estimates. The fluxes represent 30-min averages computed from three 10-min estimates.

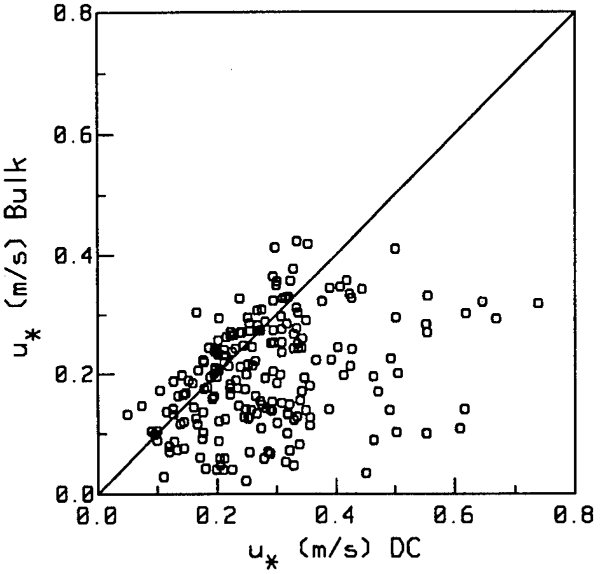

FIG. 12. A comparison of the uncorrected friction velocity estimates from the R/V *Iselin* computed from Eq. (27) vs our bulk aerodynamic estimates. The fluxes represent 30-min averages computed from three 10-min estimates.

compared against the bulk aerodynamic method where the velocity scaling parameter (i.e, the friction velocity) is defined as

$$u_* = [\langle u'w'\rangle^2 + \langle v'w'\rangle^2]^{1/4}. \tag{27}$$

Figures 10 and 11 show comparisons of the covariances computed before and after correction, respectively, using the strap-down system on the R/P *LADAS,* while Figs. 12 and 13 give the same comparisons for the R/V *Iselin.* Clearly, the agreement between the two methods is dramatically improved through correction, where the platform motion tends to cause an increase in the correlation between the signals that leads to an overestimation of the flux. There is very good agreement between the direct covariance and bulk estimates from the R/P *LADAS.* However, there appears to be some additional scatter and bias in the R/V *Iselin* comparison.

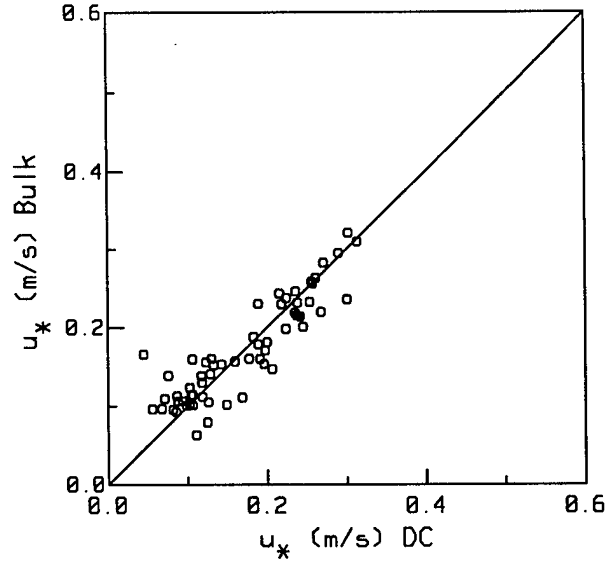

FIG. 11. A comparison of the corrected friction velocity estimates from the R/P *LADAS* computed from Eq. (27) vs our bulk aerodynamic estimates. The fluxes represent 30-min averages computed from three 10-min estimates.

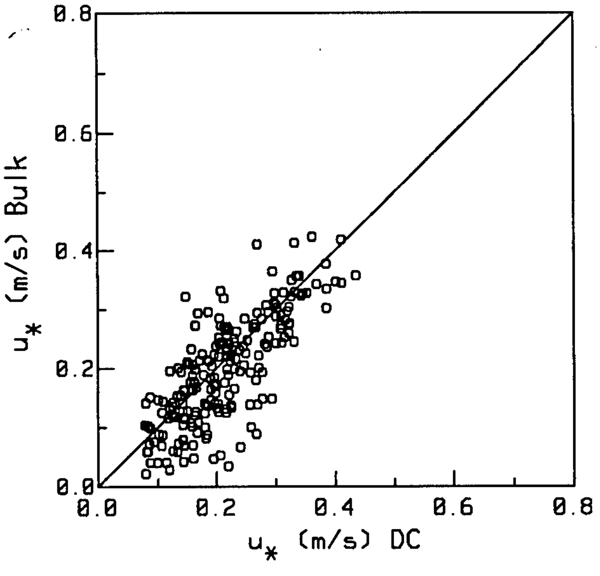

FIG. 13. A comparison of the corrected friction velocity estimates from the R/V *Iselin* computed from Eq. (27) vs our bulk aerodynamic estimates. The fluxes represent 30-min averages computed from three 10-min estimates.

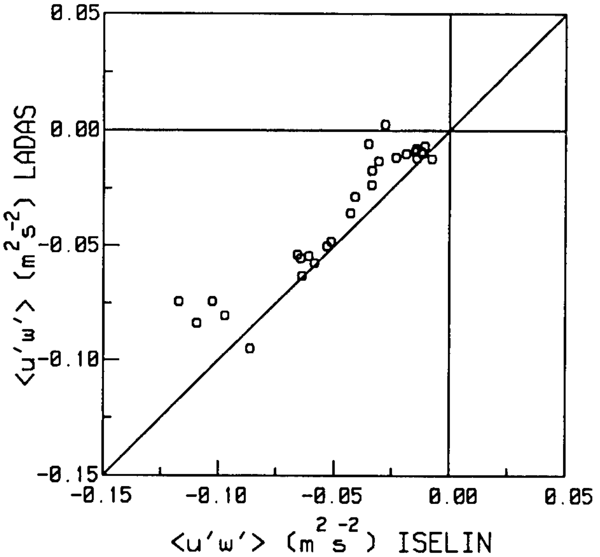

FIG. 14. A comparison of measurements of the longitudinal component ⟨$u'w'$⟩ of the momentum flux taken from the R/V *Iselin* and R/P *LADAS*. The data represent 30-min averages where there is at least 20 min of overlap between the estimates.

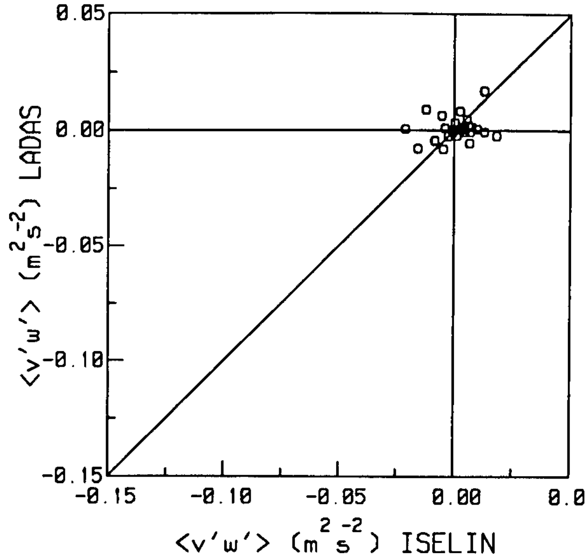

FIG. 15. A comparison of measurements of the lateral component ⟨$v'w'$⟩ of the momentum flux taken from the R/V *Iselin* and R/P *LADAS*. The data represent 30-min averages where there is at least 20 min of overlap between the estimates.

This bias is also evident in the comparison of the direct-covariance stress components computed from the R/P *LADAS* and R/V *Iselin*. These fluxes were computed by averaging together three 10-min estimates. We expect our 10-min averages to miss some of the turbulent flux that would result in an underestimation of the flux, particularly for the measurements under the low winds from the R/P *LADAS*. However, Mahrt et al. (1996) have shown that averaging together our 10-min fluxes reduces the random error in our estimates, which more than offsets the slight loss of covariance under most wind conditions.

Figures 14 and 15 compare all the 30-min averaged flux estimates where there was at least 20 min of overlap. As one would expect, the comparisons show that the lateral components are smaller in magnitude than the longitudinal components except perhaps at low wind speeds. However, the absolute values of the R/V *Iselin* fluxes are generally larger than the R/P *LADAS*, and a correlation between the lateral component of the flux is not readily apparent. While some of the discrepancy could be caused by the underestimation of the fluxes from the R/P *LADAS* at low wind speeds, we believe that we have additional evidence that points to flow distortion as the primary cause for the disagreement.

d. Flow distortion

Because of its size, the catamaran is a much better wave follower than the ship. This causes the magnitude of the motion correction required for the R/P *LADAS* to be larger than the correction required for the R/V *Iselin*. Therefore, the reduced scatter and better agreement found in Fig. 11 versus Fig. 13 (as well as the smaller residual tilt) lead us to believe that most of the difference between the various flux comparisons is due to the effects of flow distortion on our ship-based measurements. This flow distortion is expected to influence both the mean flow and the turbulence. A comparison of the wind speeds relative to the ocean surface is shown in Fig. 16, where the *LADAS* winds have been brought up to 11.5 m using the friction velocity and stability corrections obtained from the bulk algorithm. While this

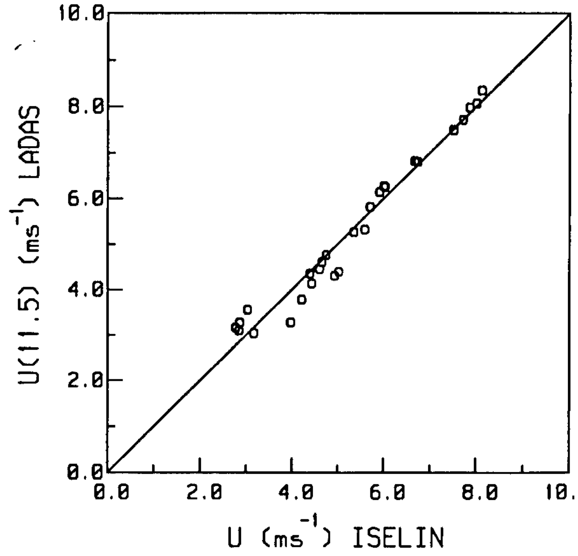

FIG. 16. A comparison of our relative wind speed measurements taken from the R/V *Iselin* and R/P *LADAS*. The R/P *LADAS* measurements have been adjusted to the height of the R/V *Iselin* measurements using the friction velocity and stability corrections computed using the bulk aerodynamic method of Fairall et al. (1996).

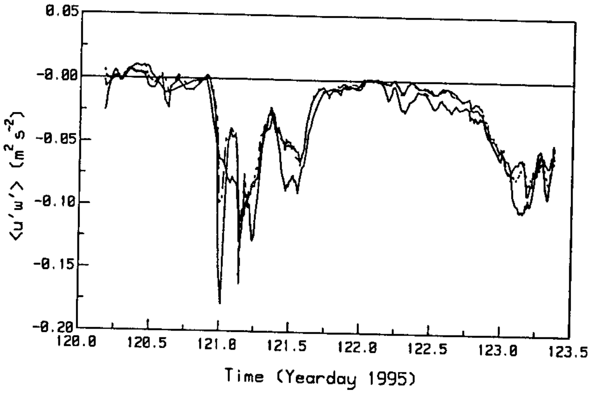

FIG. 17. A time series of the longitudinal component ⟨$u'w'$⟩ of the momentum flux measured aboard the R/P *FLIP* and R/V *Wecoma* during a 3-day period in May 1995. The dotted and dashed lines represent measurements taken at 8.7 and 13.8 m aboard the R/P *FLIP*, respectively. The solid line represents the R/V *Wecoma* data.

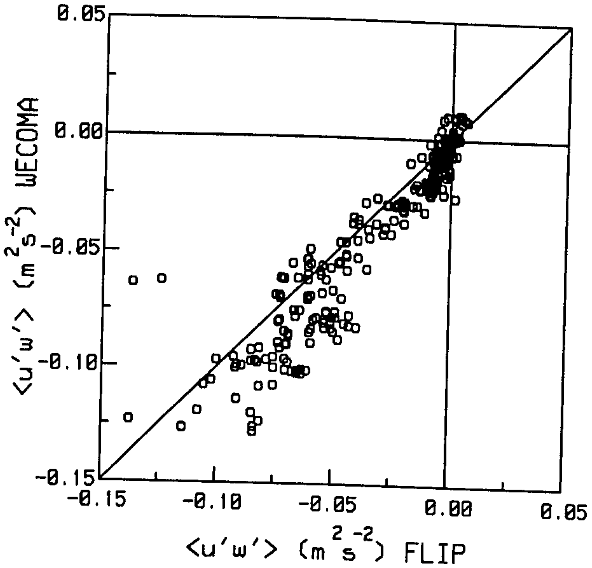

FIG. 18. A comparison of measurements of the longitudinal component ⟨$u'w'$⟩ of the momentum flux taken from the R/V *Wecoma* and R/P *FLIP*. The data represent 30-min averages computed when the R/V *Wecoma* was within 50 km of the R/P *FLIP*.

comparison exhibits some enhanced scatter at low wind speeds, any systematic difference between these velocity measurements is not readily apparent. As such, our suggestion that flow distortion causes the differences seen in the above figures remains speculative.

Fortunately, the MBL experiment provided us with the opportunity to compare our ship-based DCFS with the flux measurements made aboard the R/P *FLIP*. During the MBL experiment, the R/P *FLIP* was moored 40 km off the Monterey coast. A heavily instrumented 15-m mast was deployed at the end of the port boom by the first author and colleagues at the University of California, Irvine. This instrumentation was used to measure the momentum flux at three levels above the ocean surface. The velocity measurements from the *FLIP* also require motion correction before the fluxes were computed. However, because the corrections are typically an order of magnitude smaller than the ship-based system, we believe that this comparison provides a more quantitative evaluation of the DCFS.

Time series of the longitudinal component of the momentum flux measured at 8.7 m (dotted line) and 13.8 m (dashed line) aboard the R/P *FLIP* and at 11.3 m aboard the R/V *Wecoma* are shown in Fig. 17. This figure shows all of the flux estimates made when the ship was within 50 km of *FLIP* for relative wind directions between −120° and +120° of the bow. The time series shows that the fluxes follow each other very closely over the course of several frontal passages. However, this also indicates that the magnitude of the momentum fluxes from the ship are often higher than the R/P *FLIP*.

A direct comparison of these estimates is shown in Figs. 18 and 19, where the ship fluxes have been reduced by 15% in Fig. 19. The percentage was chosen based on a least squares fit to the data that gave a slope of 0.99 and intercept of −0.004. Correction of the R/V *Iselin* data by this same amount is shown in Fig. 20. The improved agreement in this figure provides further evidence, though indirect, that the bias is mainly due to flow distortion rather than inadequate motion correction.

We also attempted to quantify this increase as a function of relative wind direction. Unfortunately, there is not enough data to present a functional dependence of this increase on relative wind direction. However, it was clear that the magnitude of the required correction dramatically increased for directions beyond ±130° of the bow. This is why we limited our comparisons to ±120 in the comparisons shown in the above figures.

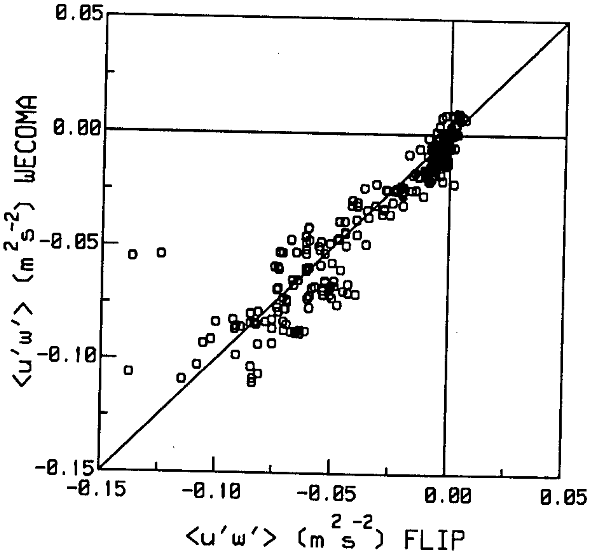

FIG. 19. As in Fig. 18 except that the R/V *Wecoma* estimates have been reduced by 15%.

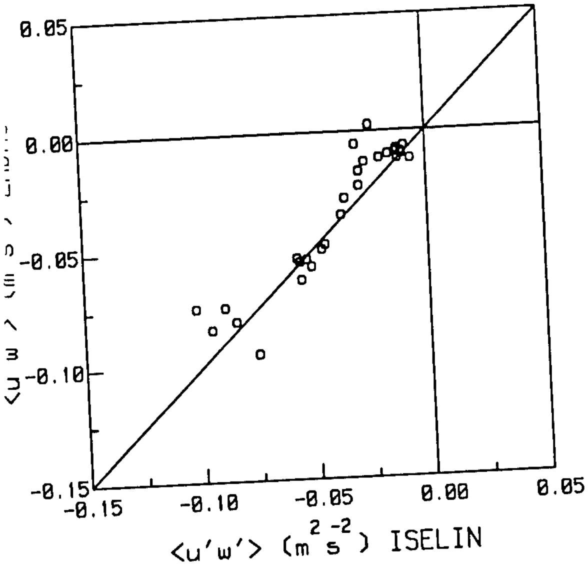

FIG. 20. As in Fig. 14 except that the R/V *Iselin* estimates have been reduced by 15%.

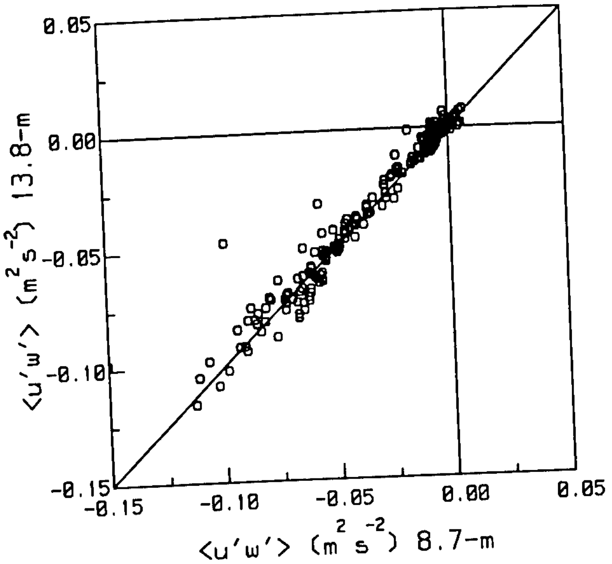

FIG. 21. A comparison of measurements of 30-min averaged longitudinal component $\langle u'w' \rangle$ of the momentum flux taken from the R/P *FLIP* at 8.7 and 13.8 m.

We believe that we have removed most of the bias n our flux estimates, reducing the flux by 15% and imiting our relative direction to within ±120° of the bow. The scatter that remains in these figures is a combination of naturally occurring spatial variability and any remaining flow distortion or incomplete motion correction. The rms difference divided by the mean of these points gives an uncertainty of approximately 18% in Fig. 19. A comparison of the momentum flux estimates measured on *FLIP* at two different heights is shown in Fig. 21. If we assume that the differences between these two heights are due primarily to atmospheric variability, then at least 9% (as calculated above) of the *Wecoma* versus *FLIP* difference is due to this variability. In fact, it is very likely that more of the difference is due to horizontal variability, particularly because the surface temperature field was very inhomogeneous in the coastal ocean off Monterey.

Perhaps the most interesting comparison between the R/V *Wecoma* and R/P *FLIP* is shown in Fig. 22. Our previous comparisons have shown that the lateral component of the momentum stress is generally small enough so that it is difficult to distinguish between the signal and noise. However, in Fig. 22 we find strong evidence of a meteorological event that causes a noticeable lateral component in both the R/P *FLIP* and R/V *Wecoma* time series. During this period the ship was cruising toward the platform at approximately 2 kt. Rawinsonde launched from the ship indicated large wind shear in the upper boundary layer indicative of strongly baroclinic conditions. A frontal passage coinciding with the oscillation in the stress vector seen in this figure passed the platforms at different times as the ship steamed toward the R/P *FLIP*. We postulate that the decrease in the separation between the two platforms is responsible for the decreasing phase lag evident in the time series.

7. Conclusions

This paper has shown that the flux systems deployed in a number of recent over-sea field programs are capable of accurately measuring a direct estimate of the flux after removing the contamination in the signal due to platform motion and flow distortion. The ability to make these estimates from a research vessel is very advantageous since the mobility of a ship makes it a very effective platform for open-ocean measurements. Additionally, deployment from a ship allows us to make flux measurements under much worse conditions than possible with the catamaran.

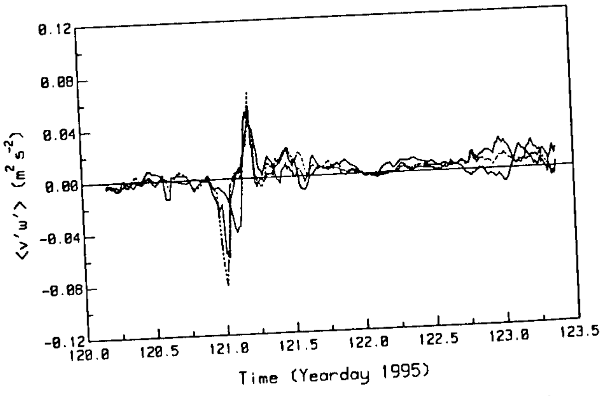

FIG. 22. A time series of the lateral component $\langle v'w' \rangle$ of the momentum flux measured aboard the R/P *FLIP* and R/V *Wecoma* during a 3-day period in May 1995. The dotted and dashed lines represent measurements taken at 8.7 and 13.8 m aboard the R/P *FLIP*, respectively. The solid line represents the R/V *Wecoma* data.

The comparisons shown in this paper indicate that the flow distortion causes an increase in the measured covariance of approximately 15% (or about 8% for the friction velocity). Though substantial, this correction is of a similar magnitude to the corrections for platform distortion applied to the HEXMAX dataset (Oost et al. 1994). Our evidence suggests that this correction is appropriate for the commonly used class of research vessels represented by the R/Vs *Wecoma* and *Iselin.* There is some evidence that this correction is a function of the direction of the relative wind vector. However, we do not have enough data processed from the R/P *FLIP* to make any definitive conclusions at this time.

Finally, some caution must be exercised when using ship-based measurements in studies examining the directional properties of marine surface layer turbulence (e.g., investigations of the influence of misaligned wind and waves on the stress vector). This caution is necessary because of the magnitude of the flow distortion and motion contamination relative to the magnitude of the lateral component of the flux. However, it appears that the fluxes can be used in case studies of directional processes under conditions where the cross-stream component of the vector stress is comparable with the along-wind component, as shown in Fig. 22. Additionally, many problems associated with flow distortion can be circumvented through use of smaller coastal vessels, low-profile towed vehicles, and moored platforms such as the R/P *LADAS,* surface buoys (e.g., Anctil et al. 1994), and the R/P *FLIP.* In fact, the time series showing the lateral component of the stress vector points out one advantage of having both mobile and moored platforms in studies investigating air–sea interactions.

Acknowledgments. The authors would like to thank Erik Bock and Fredrik Thwaites for their helpful discussions during the construction of both the system and processing algorithms, and Ditmar Bock for his suggestions on the use of complementary filtering. The engineering, technical, and scientific contributions of Nick Witzell, David Schroeder, Steve Murphy, Robert Handy, and John Boutillette at WHOI and Dave Gregg, Scott Abbott, Jesse Leach, Cat Russell, and Norbert Szczepczynski at NOAA/ETL are also acknowledged. The first author would like to thank Judy White for her assistance in preparing the manuscript. Special thanks go to Scott Miller and Carl Friehe of UC-Irvine for their help in collecting and processing the R/P *FLIP* data. The High Resolution and MBL components of this research has been supported by the Office of Naval Research (Grants N00014-92-J-1585, N00014-93-1-0274, and N00014-96-1-0012). Partial support for the NOAA/ETL component has been provided by the DOE Atmospheric Radiation Measurement program and the U.S. National Oceanic and Atmospheric Administration Climate and Global Change Program.

REFERENCES

Anctil, F., M. A. Donelan, W. M. Drennan, and H. C. Graber, 1994: Eddy-correlation measurements of air–sea fluxes from a discus buoy. *J. Atmos. Oceanic Technol.,* **11,** 1144–1150.

Anderson, R. J., 1993: A study of wind stress and heat flux over the open ocean by the inertial-dissipation method. *J. Phys. Oceanogr.,* **23,** 2153–2161.

Axford, D. N., 1968: On the accuracy of wind measurements using an inertial platform in an aircraft and an example of a measurement of the vertical mesostructure of the atmosphere. *J. Appl. Meteor.,* **7,** 645–666.

Bock, E. J., and T. Hara, 1995: Optical measurements of capillary–gravity wave spectra using a scanning laser slope gauge. *J. Atmos. Oceanic Technol.,* **12,** 395–403.

Davidson, K. L., C. E. Skupniewicz, D. Ross, R. G. Onstott, J. A. Johannessen, and O. Skagseth, 1991: Relationship between wind stress, backscatter, and the directional wave spectrum. *Proc. OCEANS '91,* Honolulu, HI, IEEE, 998–1005.

Dugan, J. P., S. L. Panichas, and R. L. DiMarco, 1991: Decontamination of wind measurements from buoys subject to motions in a seaway. *J. Atmos. Oceanic Technol.,* **8,** 85–95.

Edson, J. B., C. W. Fairall, S. E. Larsen, and P. G. Mestayer, 1991: A study of the inertial-dissipation technique for computing air–sea fluxes. *J. Geophys. Res.,* **96,** 10 689–10 711.

Fairall, C. W., and S. E. Larsen, 1986: Inertial dissipation methods and turbulent fluxes at the air ocean interface. *Bound.-Layer Meteor.,* **34,** 287–301.

——, and G. S. Young, 1991: A field evaluation of shipboard performance of an infrared hygrometer. Preprints, *Seventh Symp. on Meteorological Observations and Measurements,* New Orleans, LA, Amer. Meteor. Soc., 311–315.

——, ——, S. E. Larsen, and P. G. Mestayer, 1990: Inertial-dissipation air–sea flux measurements: A prototype system using real-time spectral computations. *J. Atmos. Oceanic Technol.,* **7,** 425–453.

——, E. F. Bradley, D. P. Rogers, J. B. Edson, and G. S. Young, 1996: Bulk parameterization of air–sea fluxes for TOGA COARE. *J. Geophys. Res.,* **101,** 3747–3764.

——, A. B. White, J. B. Edson, and J. E. Hare, 1997: Integrated shipboard measurements of the marine boundary layer. *J. Atmos. Oceanic Technol.,* **14,** 368–379.

Friehe, C. A., J. C. LaRue, F. H. Champagne, C. H. Gibson, and G. F. Dreyer, 1975: Effect of temperature and humidity fluctuations on the optical refractive index in the marine boundary layer. *J. Opt. Soc. Amer.,* **65,** 1502–1511.

Fujitani, T., 1981: Direct measurement of turbulent fluxes over the sea during AMTEX. *Pap. Meteor. Geophys.,* **32,** 119–134.

——, 1985: Method of turbulent flux measurement on a ship by using a stable platform system. *Pap. Meteor. Geophys.,* **36,** 157–170.

Geernaert, G. L., 1988: Measurements of the angle between the wind vector and wind stress vector in the surface layer over the North Sea. *J. Geophys. Res.,* **93,** 8215–8220.

——, F. Hansen, M. Courtney, and T. Herbers, 1993: Directional attributes of the ocean surface wind stress vector. *J. Geophys. Res.,* **98,** 16 571–16 582.

Goldstein, H., 1965: *Classical Mechanics.* Addison-Wesley, 398 pp.

Hamming, R. W., 1977: *Digital Filters.* Prentice-Hall, 297 pp.

Hare, J. E., J. B. Edson, E. J. Bock, and C. W. Fairall, 1992: Progress on direct covariance measurements of air–sea fluxes from ships and buoys. Preprints, *10th Symp. Turbulence and Diffusion,* Portland, OR, Amer. Meteor. Soc., 281–284.

Herr, F., C. Luther, G. Marmorino, R. Mied, and D. Thompson, 1991: Ocean surface remote sensing program planned. *Eos, Trans. Amer. Geophys. Union,* **72,** 214.

Kaimal, J. C., J. C. Wyngaard, Y. Izumi, and O. R. Cote, 1972: Spectral characteristics of surface layer turbulence. *Quart. J. Roy. Meteor. Soc.,* **98,** 563–589.

Large, W. G., and S. Pond, 1981: Open ocean momentum flux measurements in moderate to strong winds. *J. Phys. Oceanogr.*, **11**, 324–336.

——, and ——, 1982: Sensible and latent heat flux measurements over the ocean. *J. Phys. Oceanogr.*, **12**, 464–482.

Larsen, S. E., J. B. Edson, C. W. Fairall, and P. G. Mestayer, 1993: Measurement of temperature spectra by a sonic anemometer. *J. Atmos. Oceanic Technol.*, **10**, 345–354.

Lenschow, D. H., and P. Spyers-Duran, 1987: Measurement techniques: Air motion sensing. NCAR Bulletin 23, 361 pp. [Available from National Center for Atmospheric Research, P.O. Box 3000, Boulder, CO 80303.]

Liu, W. T., K. B. Katsaros, and J. A. Businger, 1979: Bulk parameterizations of the air–sea exchange of heat and water vapor including the molecular constraints at the interface. *J. Atmos. Sci.*, **36**, 1722–1735.

Oost, W. A., C. W. Fairall, J. B. Edson, S. D. Smith, R. J. Anderson, J. A. B. Wills, K. B. Katsaros, and J. DeCosmo, 1994: Flow distortion calculations and their application in HEXMAX. *J. Atmos. Oceanic Technol.*, **11**, 366–386.

Rieder, K. F., J. A. Smith, and R. A. Weller, 1994: Observed directional characteristics of the wind, wind stress, and surface waves on the open ocean. *J. Geophys. Res.*, **99**, 22 589–22 596.

Smith, S. D., 1988: Coefficients for sea surface wind stress, heat flux and wind profiles as a function of wind speed and temperature. *J. Geophys. Res.*, **93**, 15 467–15 472.

Twaites, F. T., 1995: Development of an acoustic vorticity meter to measure shear in ocean-boundary layers. Ph.D. thesis, Massachusetts Institute of Technology and Woods Hole Oceanographic Institution, 186 pp.

Yelland, M. J., P. K. Taylor, I. E. Consterdine, and M. H. Smith, 1994: The use of the inertial dissipation technique for shipboard wind stress determination. *J. Atmos. Oceanic Technol.*, **11**, 1093–1108.

Observation of Short Wind Waves in Coastal Waters*

TETSU HARA

Graduate School of Oceanography, University of Rhode Island, Narragansett, Rhode Island

ERIK J. BOCK, JAMES B. EDSON, AND WADE R. MCGILLIS

Department of Applied Ocean Physics and Engineering, Woods Hole Oceanographic Institution, Woods Hole, Massachusetts

(Manuscript received 24 February 1997, in final form 18 September 1997)

ABSTRACT

Observations of wind-generated gravity–capillary waves have been made during two recent field programs in coastal environments. The results of wave slope spectra on clean water show a well-defined correlation with the wind friction velocity. However, spectral values at higher wavenumbers (above 200 rad m^{-1}) are significantly higher than previous laboratory results. In the presence of surface films wave spectra may decrease by more than one order of magnitude at lower wind stresses. The dispersion characteristics of short waves vary markedly depending on the wavenumber, the wind stress, and the surface chemical condition. Some results in the presence of surface films at intermediate winds show much higher apparent phase speeds than the theoretical dispersion relation. This may be because of an enhanced near-surface current or because of the relative increase of wave energy that is phase-locked to longer steep gravity waves.

1. Introduction

It has been recognized that short wind waves (gravity–capillary waves) play important roles in various air–sea interaction processes, including air–sea momentum flux and air–sea gas transfer. While shorter wind waves support a significant part of the total wind stress (momentum flux from air to water), their contribution has been parameterized only empirically (e.g., Charnock 1955), without addressing the detailed physical mechanism of the momentum flux. As a result, our predictive capability of the effective ocean surface roughness (or the drag coefficient) is still far from satisfactory. Recent laboratory studies have suggested that short wind waves are closely correlated with the air–sea gas transfer velocity of slightly soluble gases (Jähne et al. 1987; Hara et al. 1995), and several theories have been proposed to explain such observations (e.g., Csanady 1990). Yet the exact mechanism of the air–sea gas transfer, including the role of short wind waves, is still a matter of contention. In order to improve our understanding of the influences of short wind waves on air–sea interaction processes, it is vital to obtain accurate measurements of short wind waves in a wide range of field conditions.

Direct observations of short wind waves are also important for the practical applications of microwave radar remote sensing of the ocean. For example, the interpretation of synthetic aperture radar (SAR) images requires a precise knowledge of the interaction between short wind waves (scatterer of microwaves) and other environmental parameters in the atmosphere (e.g., atmospheric turbulence, momentum flux, heat flux), at the air–sea interface (e.g., surface waves, wave breaking, air–sea gas flux), and in the ocean (e.g., near-surface turbulence, near-surface currents, internal waves).

Past direct observations of short wind waves have been carried out mostly in laboratory wind–wave flumes. Ebuchi et al. (1987) investigated fine structures of wind wave surfaces, such as rhombic patterns of gravity–capillary waves and parasitic capillaries. Jähne and Riemer (1990) measured spatial structures of short wind waves in a large wind–wave flume using an imaging optical technique. Their results have shown that the dynamics of gravity–capillary waves is very different from that of gravity waves and depends on the wind stress and the wavenumber in a quite complex manner. Further refinements of laboratory studies have been made by Hwang et al. (1993) and Zhang (1995); the latter has identified various features of parasitic capillary waves formed on the downwind faces of gravity waves. A laboratory study by Hara et al. (1997) has focused on the dispersion characteristics of short wind

---

* Woods Hole Oceanographic Institution Contribution No. 9562.

Corresponding author address: Dr. Tetsu Hara, Graduate School of Oceanography, University of Rhode Island, South Ferry Road, Narragansett, RI 02882.
E-mail: t.hara@gso.uri.edu

waves. They have shown that a significant part of short wind wave energy may be phase-locked to steep gravity waves—that is, propagate at the phase speed of the gravity waves. They have also suggested that nonlinear wave interactions may enhance the level of short wind waves in particular oblique directions relative to the mean wind.

Although recent laboratory studies have enhanced our knowledge of short wind waves in laboratory settings, in situ observations are still scarce. A field study by Hara et al. (1994), carried out in fetch-limited water, has shown that short wind wave spectra at low wind stresses are significantly higher than laboratory observations. A recent field observation by Hwang et al. (1996), obtained on open ocean, also shows marked difference between field and laboratory results. They attribute the difference to naturally occurring wind fluctuation in field conditions.

Here, we present the results of two recent field experiments on short wind waves using a scanning laser slope gauge. The instrument is capable of resolving the spatiotemporal structure of wind waves in the range of wavenumbers between 50 and 800 rad m^{-1}, and frequencies up to the Nyquist frequency of 52.1 Hz. In section 2, the overviews of the field programs and experimental methods are explained. The results and interpretations are presented in section 3. Our results demonstrate a strong influence of surface films, resulting in large variability of short wind wave spectra in a coastal environment. Our data also confirm the difference between field and laboratory wave conditions at lower wind stresses. Detailed investigations of the dispersion characteristics and directional spreading of short wind waves are also made. Finally in section 4, our observations are summarized and their implications to future studies are discussed.

2. Experimental overview

a. High-resolution remote sensing experiment

The main experiment of the High-Resolution Remote Sensing Accelerated Research Initiative (Hi-Res II) took place in June of 1993 and was sponsored by the Office of Naval Research and Naval Research Laboratory. The principal objective of the initiative was to perform an in-depth study of the relationship between radar backscatter and atmospheric, surface, and subsurface processes. To determine these relations, a research catamaran was deployed as a means of obtaining in situ measurements of gravity–capillary waves (using a scanning laser slope gauge), dominant gravity waves (using a capacitive wave wire and a motion detection package), and subsurface currents (using a three-axis acoustic Doppler current meter). The catamaran was equipped with an electric motor and a remotely controlled rudder, and was towed from the starboard side (about two-thirds of the total ship length from the bow) of the R/V *Iselin.* Its position was maintained at a distance of about 20 m to the side of the ship in order to minimize wind blockage and operate outside of the ship's wake. The tow speed was mostly between 0.5 and 1 m s^{-1}. The wind speed and the wind stress were obtained on the catamaran and at the bow of the ship using sonic anemometers (Edson et al. 1998). The locations of the experiment were near the coast of Cape Hatteras, North Carolina, and are shown in Fig. 1 by two large circles. Both sites were located in the vicinity of the Gulf Stream north wall. Therefore, data were collected both over coastal water and over Sargasso Sea water.

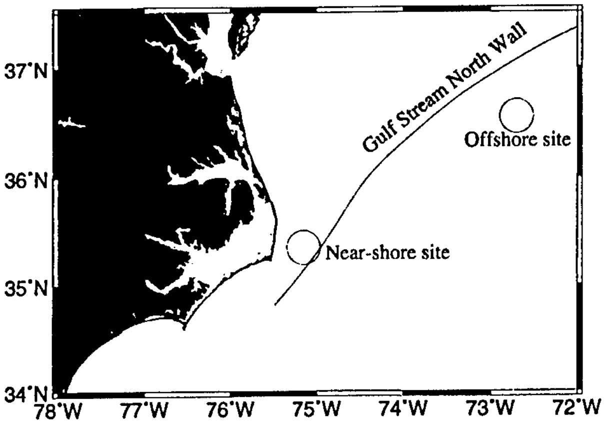

FIG. 1. Location of High-Resolution Remote Sensing Main Experiment (Hi-Res II).

b. Coastal ocean processes experiment

As part of the Coastal Ocean Processes (CoOP) program sponsored by the National Science Foundation, an experiment was carried out in April–May of 1995 to investigate the role of various ocean surface processes on the air–sea gas exchange. The research catamaran was towed to the side of the R/V *New Horizon.* Measurements of gravity–capillary waves, dominant gravity waves, subsurface currents/turbulence, and surface chemical enrichment were made possible with the instrument array aboard the catamaran. The array included a set of six capacitive wave wires, a motion detection package, a three-axis acoustic Doppler current meter, a hot film anemometer, and a surface skimmer. The measurement of the wind speed and the wind stress were made using a sonic anemometer at the bow of the ship. The locations of the experiment were off the coast of California and are shown in Fig. 2. They included both sites with low surface chemical enrichment values shown by diamonds and sites with high and variable enrichment values shown by crosses. Higher values of surface chemical enrichment are indicative of higher concentrations of surfactant (N. M. Frew 1995, personal communication).

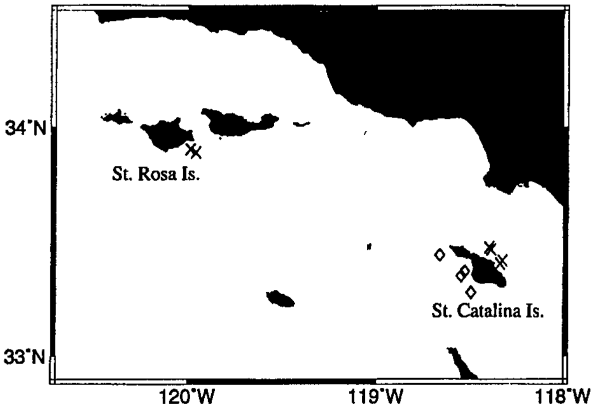

FIG. 2. Location of Coastal Ocean Processes Experiment (CoOP). Crosses, sites with high and variable surface enrichment values. Diamonds, sites with low surface enrichment values.

c. Wind stress measurements

Wind stress estimates were made using sonic anemometers mounted on the two research vessels and the catamaran. Direct covariance flux systems were deployed during the Hi-Res II experiment at 11.5 and 5.6 m above the mean sea surface aboard the R/V *Iselin* and the research catamaran, respectively. These measurements were corrected for platform motion as described by Edson et al. (1998) to compute the momentum and heat fluxes using the direct covariance (eddy correlation) method. Instrumentation to measure the mean temperature and humidity was included in both packages. These measurements were combined with the mean wind speed (relative to the water surface) to estimate the flux using the bulk aerodynamic method described by Fairall et al. (1996). The sonic anemometers were also used to compute dissipation estimates using the Kolmogorov relationship and spectral estimates in the inertial subrange (Kolmogorov 1941). The dissipation rates were used with the semiempirical functions found in Fairall and Edson (1994) to compute inertial-dissipation flux estimates.

A similar set of instrumentation was deployed at a height of 10 m on a bow mast aboard the R/V *New Horizon* during the CoOP experiment. Problems with the vertical accelerometers (required to correct for ship motion) prohibited direct covariance flux estimates. Therefore, the stress estimates used in this paper are derived from the bulk aerodynamic and inertial dissipation methods using the formulations described above.

d. Short wind wave measurements

The measurements of short wind waves were carried out using a scanning laser slope gauge developed by Bock and Hara (1995). The instrument was previously used in a field study (Hara et al. 1994) and a laboratory study (Hara et al. 1997). The data analysis scheme and the error analysis have been discussed in detail in earlier papers and are not repeated here. In short, the instrument yields three-dimensional wavenumber–frequency slope spectra of short wind waves for wavenumbers between 50 and 800 rad m^{-1} and frequencies up to the Nyquist frequency of 52.1 Hz during the CoOP (wavenumbers up to 400 rad m^{-1} and the Nyquist frequency 18.9 Hz during the Hi-Res II). Because of instrumental noise and sidelobes associated with our data analysis scheme, results near zero frequency may be contaminated. Therefore, care has been taken when the results are integrated in frequency to calculate wavenumber slope spectra [see Hara et al. (1997) for details]. During the CoOP experiment, the data were further contaminated by the vibration of the instrument. Fortunately, the noise from the vibration was almost uniform in space (concentrated near-zero wavenumber) and did not affect the real wave signal for wavenumbers above 50 rad m^{-1}. Further error analyses are summarized in the appendix.

e. Definitions

Let us define a coordinate system such that the x axis is in the mean wind direction, the z axis is vertically upward measured from the mean water surface, and the y axis is defined according to the right-hand rule. We denote the surface elevation by $z = \zeta(x, y, t)$, and the surface slope by $\nabla\zeta = (\partial\zeta/\partial x, \partial\zeta/\partial y)$. The autocorrelation function of the surface slope is defined as

$$R(\xi, \eta, \tau) = \overline{\nabla\zeta(x, y, t)\cdot\nabla\zeta(x + \xi, y + \eta, t + \tau)}, \quad (1)$$

where the overbar indicates the time average. Then, the three-dimensional one-sided frequency–wavenumber slope spectrum is calculated to be

$$S(k, \theta, \omega) = \frac{1}{4\pi^3}\int\int\int_{-\infty}^{\infty} R(\xi, \eta, \tau)e^{-i(k\xi\cos\theta + k\eta\sin\theta - \omega\tau)}\,d\xi\,d\eta\,d\tau, \quad (2)$$

where k is the wavenumber, ω is the angular frequency, and θ is the wave direction measured from the x axis in the counterclockwise direction. Here $\theta = 0$ corresponds to waves in the wind direction and $\theta = \pm\pi/2$ corresponds to waves in the crosswind directions. This three-dimensional spectrum is defined for $0 < k < \infty$, $-\infty < \omega < \infty$, and $-\pi/2 < \theta < \pi/2$. Note that a negative ω corresponds to waves propagating against the wind. By definition, the mean square slope is recovered by integrating $S(k, \theta, \omega)$ as

$$\overline{\nabla\zeta\cdot\nabla\zeta} = \int_{-\infty}^{\infty}\int_{-\pi/2}^{\pi/2}\int_{0}^{\infty} S(k, \theta, \omega)k\,dk\,d\theta\,d\omega. \quad (3)$$

The one-sided two-dimensional wavenumber spectrum is calculated by integrating $S(k, \theta, \omega)$ in frequency:

$$S(k, \theta) = \int_{-\infty}^{\infty} S(k, \theta, \omega)\,d\omega, \quad (4)$$

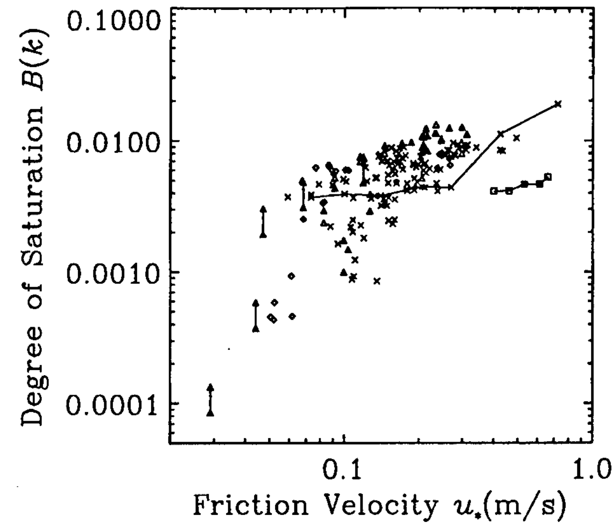

FIG. 3. Omnidirectional degree of saturation vs wind friction velocity at wavenumber 100 rad m^{-1}. Crosses: this study (CoOP); triangles: this study (Hi-Res II); pairs of triangles connected vertically by solid lines: Hwang et al. (1996); diamonds: Hara et al. (1994); crosses connected by solid lines: Jähne and Riemer (1990); and squares connected by solid lines: Zhang (1995).

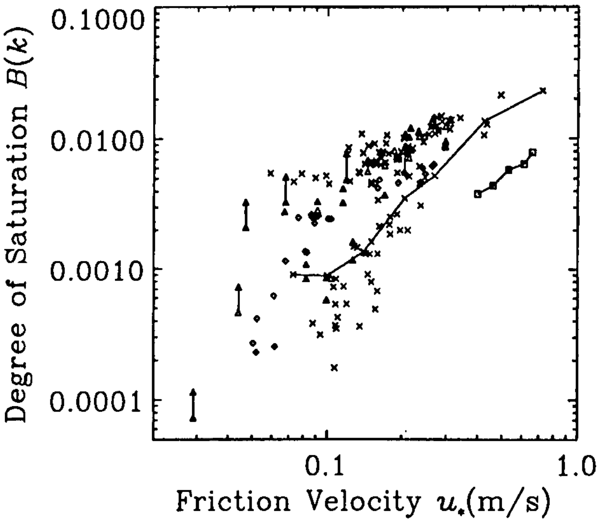

FIG. 4. Omnidirectional degree of saturation vs wind friction velocity at wavenumber 200 rad m^{-1}. Crosses: this study (CoOP); triangles: this study (Hi-Res II); pairs of triangles connected vertically by solid lines: Hwang et al. (1996); diamonds: Hara et al. (1994); crosses connected by solid lines: Jähne and Riemer (1990); squares connected by solid lines: Zhang (1995).

which is defined for $0 < k < \infty$ and $-\pi/2 < \theta < \pi/2$. The nondimensional degree of saturation is defined as

$$B(k, \theta) = k^2 S(k, \theta). \tag{5}$$

Finally, the omnidirectional (one-dimensional) wavenumber slope spectrum and the omnidirectional degree of saturation are defined as

$$S(k) = \int_{-\pi/2}^{\pi/2} S(k, \theta)\, d\theta \tag{6}$$

and

$$B(k) = k^2 S(k) \tag{7}$$

respectively.

3. Results and discussion

a. *Wavenumber slope spectrum from current and past studies*

We first summarize the results of the wavenumber slope spectrum from this study as well as from past studies. In Figs. 3–6 the omnidirectional degree of saturation, $B(k)$, is plotted against the wind friction velocity, u_*, from the bulk aerodynamic method, at four different wavenumbers k = 100, 200, 400, and 800 rad m^{-1}. Our results from the Hi-Res II and the CoOP experiments are shown by triangles and crosses, respectively. These results are averaged over 8 min so that the statistical scatter is negligibly small (Bock and Hara 1995). Therefore, the scatter in these figures must be due to real environmental variabilities. In addition to the results of this study, the figures contain data from two previous field studies. The results by Hara et al. (1994) (diamonds) were obtained at Martha's Vineyard Sound, Massachusetts, in November 1993. The wind fetch at the experimental location was limited to 7 km. The results of Hwang et al. (1996), shown as pairs of triangles connected vertically, were obtained during the same Hi-Res II experiment but using a scanning laser slope gauge of a very different design. Since they report

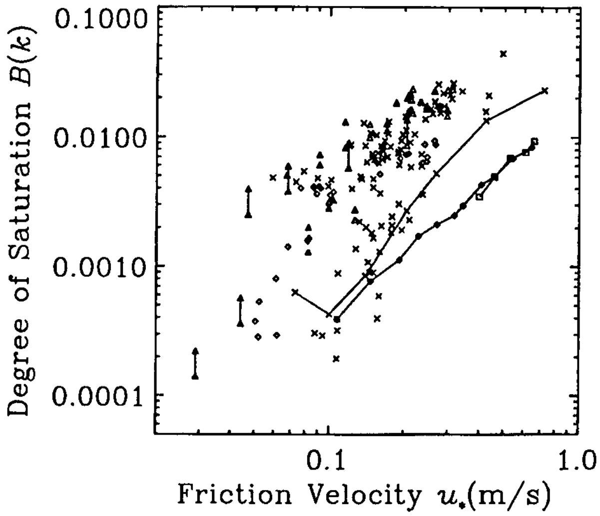

FIG. 5. Omnidirectional degree of saturation vs wind friction velocity at wavenumber 400 rad m^{-1}. Crosses: this study (CoOP); triangles: this study (Hi-Res II); pairs of triangles connected vertically by solid lines: Hwang et al. (1996); diamonds: Hara et al. (1994); crosses connected by solid lines: Jähne and Riemer (1990); squares connected by solid lines: Zhang (1995); diamonds connected by solid lines: Hara et al. (1997).

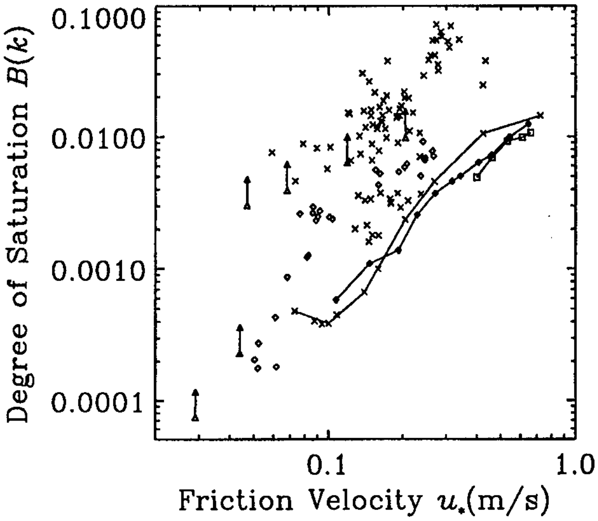

FIG. 6. Omnidirectional degree of saturation vs wind friction velocity at wavenumber 800 rad m^{-1}. Crosses: this study (CoOP); pairs of triangles connected vertically by solid lines: Hwang et al. (1996); diamonds: Hara et al. (1994); crosses connected by solid lines: Jähne and Riemer (1990); squares connected by solid lines: Zhang (1995); diamonds connected by solid lines: Hara et al. (1997).

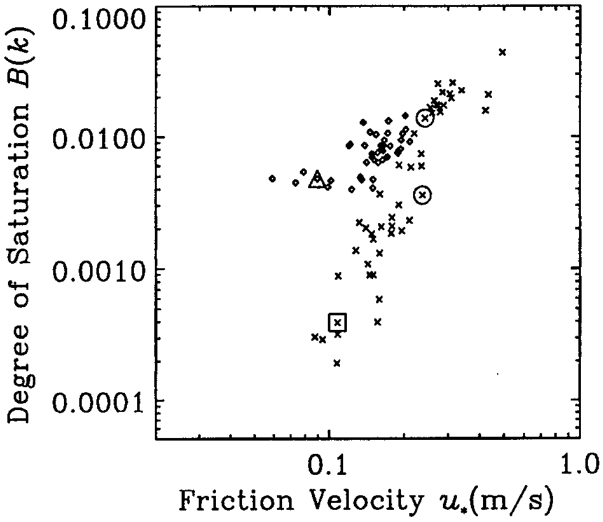

FIG. 7. Omnidirectional degree of saturation vs wind friction velocity at wavenumber 400 rad m^{-1} from CoOP. Crosses: sites with high and variable surface enrichment values; diamonds: sites with low surface enrichment values. Large symbols correspond to cases discussed in detail in the text.

the degree of saturation in the along-wind direction only, $B(k, \theta = 0)$, the omnidirectional value, $B(k)$, is estimated assuming two extreme directional spreading functions and are shown as upper and lower bounds. The upper bound corresponds to a uniform directional spreading, and the lower bound corresponds to a directional spreading of the form of $\cos\theta$. We have ascertained that most of the data from this study exhibit directional spreading, which falls between these two extreme spreading functions. Since our data from the Hi-Res II, shown by triangles, were obtained roughly at the same sites and at the same periods as those by Hwang et al. (1996), the reasonable agreement between the two datasets confirms the accuracy of both measurements. The laboratory results by Jähne and Riemer (1990), Zhang (1995), and Hara et al. (1997) were obtained at the fetch of roughly 100 m, 25 m, and 13 m, respectively. Since results with shorter fetches and at smaller wavenumbers are strongly fetch-dependent, such results are excluded from the figures.

At the lowest wavenumber k = 100 rad m^{-1}, most of the field results collapse rather tightly above u_* = 0.07 m s^{-1}, except some lower points from the Hi-Res II and the CoOP. The field results increase slowly and smoothly with wind stress. Although the laboratory results by Jähne and Riemer (1990) show two distinctive ranges, that is, $B(k)$ is constant below u_* = 0.3 m s^{-1} and increases with u_* above u_* = 0.3 m s^{-1}, their results fall within the scatter of the field results. As the wavenumber increases to k = 200–800 rad m^{-1}, a well-defined cluster of the field results is still observed near the upper edge of the overall distribution in each figure. However, the location of the cluster deviates upward from the laboratory results as k increases. At k = 200 and 400 rad m^{-1}, the discrepancy between the cluster and the laboratory result by Jähne and Riemer (1990) is large at lower wind stresses but decreases at higher wind stresses. At k = 800 rad m^{-1}, the cluster is higher than the laboratory result by roughly one order of magnitude throughout the entire wind stress range. At wavenumbers k = 200–800 rad m^{-1}, we also observe a larger scatter of field results below the cluster at lower wind stresses. Some points are lower than those in the cluster by more than one order of magnitude.

b. *Variability of slope spectrum from CoOP*

To investigate the reason for the large scatter of the field data at higher wavenumbers and at lower wind stresses, we focus on the results at k = 400 rad m^{-1} from the CoOP experiment only. In Fig. 7 we plot the same omnidirectional degree of saturation, $B(k)$, separated by the location of the measurement. The diamonds correspond to data obtained on the western side of St. Catalina Island, shown by diamonds in Fig. 2. The environmental conditions there are characterized by large to unlimited fetches, very low values of surface chemical enrichment suggesting clean water surfaces, and well-developed swells. The crosses are data collected on the eastern side of St. Catalina Island or near St. Rosa Island, shown by crosses in Fig. 2. These locations are characterized by limited fetches, high and variable surface enrichment values indicating the presence of surface films, and very low swells. It is clear that the diamonds show a well-defined correlation with the wind friction velocity. On the other hand, the crosses scatter widely and are lower than the diamonds for the friction

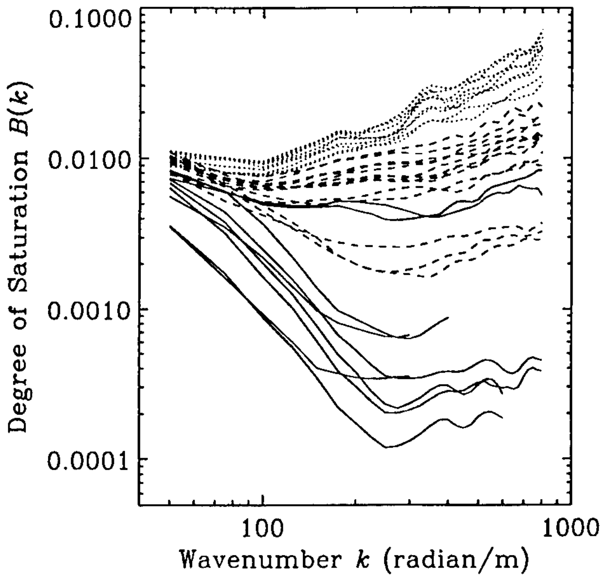

FIG. 8. Omnidirectional degree of saturation vs wavenumber. Dotted lines: near $u_* = 0.3$ m s^{-1}; dashed lines: near $u_* = 0.2$ m s^{-1}; solid lines: near $u_* = 0\ 1$ m s^{-1}.

velocity below 0.25 m s^{-1}. As the wind stress increases, the higher values of the crosses approach those of the diamonds. At high winds ($u_* > 0.25$ m s^{-1}), the crosses seem to be smoothly connected to the diamonds at lower winds. These observations suggest that short wind waves on clean water surfaces show a well-defined correlation with the wind stress and those on water surfaces with surfactant are highly variable and generally lower than clear water results at lower winds ($u_* < 0.25$ m s^{-1}). At higher winds the effect of surfactant seems to become insignificant. It is also possible that the difference in fetch and swell conditions may contribute to the variability of short wind wave spectra.

In Fig. 8, we show the omnidirectional degree of saturation, $B(k)$, against the wavenumber, k, near three different wind friction velocities of $u_* = 0.1$, 0.2, and 0.3 m s^{-1}. Except for the cases with surfactant (the lower three lines near $u_* = 0.2$ m s^{-1} and the lower seven lines near $u_* = 0.1$ m s^{-1}), the degree of saturation is quite uniform over the range of wavenumbers shown. At lower wavenumbers $B(k)$ depends on u_* very weakly, while $B(k)$ increases slowly with u_* at higher wavenumbers. With surfactant, the results near $u_* = 0.2$ m s^{-1} gradually deviate from the clean water results between $k = 100$ and 400 rad m^{-1}. At higher wavenumbers the ratio between clean and surfactant cases seem to be almost constant. The results near $u_* = 0.1$ m s^{-1} in the presence of surfactant show that some $B(k)$ values are lower than the clean water values, even at low wavenumbers ($k < 100$ rad m^{-1}). The difference increases rapidly between $k = 100$ and 300 rad m^{-1}. Above $k = 300$ rad m^{-1}, $B(k)$ is as small as 2% of the clean water values.

It is rather surprising that at $u_* = 0.3$ m s^{-1} the degree of saturation increases rapidly (almost linearly) with k and reaches as high as 0.07 at $k = 800$ rad m^{-1}. These results also look anomalously high in Fig. 6. However, our error analyses (see appendix) suggest that there are no significant error sources that may artificially increase the spectral estimate. It is of interest to see whether future wind wave measurements by other methods will yield similar high values in open ocean conditions.

c. Difference between field and laboratory results

As we have discussed in the previous subsection, lower values of the field results are probably attributable to the presence of surface films. Then, the major cluster of the field results near the upper edge in Figs. 3–6 can be considered as typical field values at clean water surfaces. However, this does not explain the large discrepancy between the field results and the laboratory results in these figures. Such discrepancy was also reported by Hwang et al. (1996). One might be tempted to suspect that the previous laboratory results were always contaminated by surface films. However, during the laboratory experiment reported by Hara et al. (1997), surface chemical conditions were carefully monitored and were found to be very clean. Mechanically generated capillary waves were found to dissipate at the predicted dissipation rate, and the measured surface tension was consistent with the clean water value. Furthermore, the reasonable agreement between the results by Hara et al. (1997) and those by Jähne and Riemer (1990) at higher wavenumbers suggests that the experiment by Jähne and Riemer (1990) was also conducted with clean water surfaces (the deviation at lower wavenumbers can be attributed to differences in fetch). Therefore, we need to provide different explanations for the discrepancy between laboratory and field results.

One possible reason is the influence of wind fluctuation as suggested by Hwang et al. (1996). The fluctuation of the wind friction velocity is always much larger in the field than in laboratories. Since the laboratory results of $B(k)$ increase faster than linearly with u_* at higher wavenumbers, a larger fluctuation of u_* may increase the mean value of $B(k)$ for a given mean u_*, if the statistical distribution of u_* values is symmetric above and below its mean. However, this bias due to wind fluctuation is not likely to account for the tenfold increase of $B(k)$ from laboratories to the field. Another possible reason for the higher short wind wave spectra in the field is the influence of nonlinear interactions among different wave modes. These may include the interaction among three or more free-propagating waves that satisfy the resonance condition. Evidences of such wave interactions have been reported by Zhang (1995) and Hara et al. (1997) in laboratory settings. In addition, observations by Hara et al. suggest a possibility that interactions take place among two symmetric oblique short waves and longer steep gravity waves when the sum frequency and the sum wavenumber vector of the two oblique modes match those of one of the higher harmonics of the gravity waves. Alternatively, this mechanism might be considered as small-scale short-crested roughness excited by, and phase-locked to, steep gravity waves. If longer gravity waves play an important role in exciting short waves, the difference between the field and laboratories can be attributed, at least in part, to the difference of gravity wave fields.

d. Frequency–wavenumber slope spectrum

In this section we examine the dispersion characteristics of short wind waves through their frequency–wavenumber spectrum obtained during the CoOP. We first remove the Doppler shift due to the tow speed of the catamaran, using the mean relative current measured by a shipboard acoustic Doppler current profiler (ADCP) and averaged over eight minutes. During limited deployments, collocated simultaneous mean current measurements were made at a 0.2-m depth using the acoustic current meter mounted on the catamaran. We have ascertained that the difference between the two current measurements is less than 10% of the ADCP current values (typically 0.5–1.0 m s^{-1}) in most cases. The results are still influenced by the Doppler shifts due to gravity wave orbital velocities and due to the fluctuation of the tow speed that depends on the dynamical response of the catamaran to the gravity wave motion. It has been found that, when large swells are present, the responding motion of the towed catamaran introduces a large Doppler shift that masks most of the dispersion characteristics of short waves. Therefore, we only present results obtained without significant swells—that is, cases corresponding to crosses in Fig. 7. We do not show the results at lower wavenumbers ($k < 50$ rad m^{-1}) because the data are contaminated by the instrument vibration.

In Figs. 9 and 10, we show the three-dimensional wavenumber–frequency slope spectrum $S(k, \theta, \omega)$ along the mean wind direction $\theta = 0$. The same slope spectra at two fixed wavenumbers, $k = 150$ and 300 rad m^{-1}, but in all directions are shown in Figs. 11 and 12. Note that the scale is relative and exaggerated in Figs. 11 and 12. These two sets of data were obtained 78-min apart during the same catamaran deployment, and correspond to the two large circles in Fig. 7. Although the wind stress remained almost constant over the period ($u_* =$ 0.24 m s^{-1} for both figures), the degree of saturation at $k = 400$ rad m^{-1} decreased by a factor of 4, corresponding to increasing surface enrichment values (indicative of increasing surface films). In these figures solid lines are added to indicate the theoretical dispersion relation of gravity–capillary waves:

$$\omega^2 = gk + \frac{\gamma k^3}{\rho}, \tag{8}$$

where g is the gravitational acceleration, γ is the surface tension ($\gamma = 0.073$ N m^{-2} is used), and ρ is the density of water. The positive and negative solutions of (8) correspond to the waves propagating in the wind direction (alongwind waves) and those propagating against the wind, respectively.

In Figs. 9 and 11, the peak of the spectrum is located slightly below the dispersion relation of alongwind waves (upper solid line), and the wave energy spreads widely in frequency above and below the peak. Relatively high spectral values are observed at negative frequencies corresponding to waves (apparently) propagating against the wind. These observed spectra cannot be attributed solely to alongwind gravity–capillary waves that are Doppler shifted by longer gravity waves. Although large negative orbital velocities of longer gravity waves can temporarily Doppler shift the spectrum into negative frequencies, they cannot shift the entire spectrum in the negative direction, as in Figs. 9 and 11, unless most of the short wind waves are concentrated near the troughs of the longer gravity waves, which is not likely. It is possible that the entire spectrum is shifted to lower frequencies by a strong adverse near-surface mean current. However, there are no reasonable physical explanations why a near-surface current may develop against the wind relative to the bulk current measured by the ADCP. We therefore suspect that some of the short waves are literally propagating against the wind. With our limited observations we cannot completely rule out a possibility that upwind-traveling waves were generated by the towed platform itself. Further observational studies are needed to clarify the source of the upwind-traveling waves. The directional spreading of the wave energy becomes more uniform as the wavenumber increases. The slope spectrum of the crosswind waves is lower than that of alongwind waves by 25%–30% at $k = 150$ rad m^{-1} and by 15%–20% at $k = 300$ rad m^{-1} if integrated over all frequencies.

After 78 min the slope spectrum decreases significantly at higher wavenumbers. At the same time, the dispersion characteristics change as is shown in Fig. 10. Now the wave energy is distributed more narrowly in frequency indicating less Doppler shifting. The phase speed of the waves is much larger than the previous results and is high above the theoretical dispersion relation shown by the upper solid line. There is no appreciable wave energy in negative frequencies. The directional frequency spectra in Fig. 12 also differ from those in Fig. 11. At $k = 150$ rad m^{-1} the spectral level (integrated in all frequencies) in the crosswind direction is lower than that in the alongwind direction by 15%–20%; that is, the directional spreading is more uniform than in Fig. 11a. At the higher wavenumber of $k = 300$ rad m^{-1}, the crosswind value is 25%–30% lower than the peak value—that is, the distribution is more peaked than in Fig. 11b.

One possible explanation of the large change of the dispersion characteristics from Fig. 9 to Fig. 10 is that a strong near-surface current developed over the 78-min period. If we add a near-surface current of 0.27 m s^{-1}

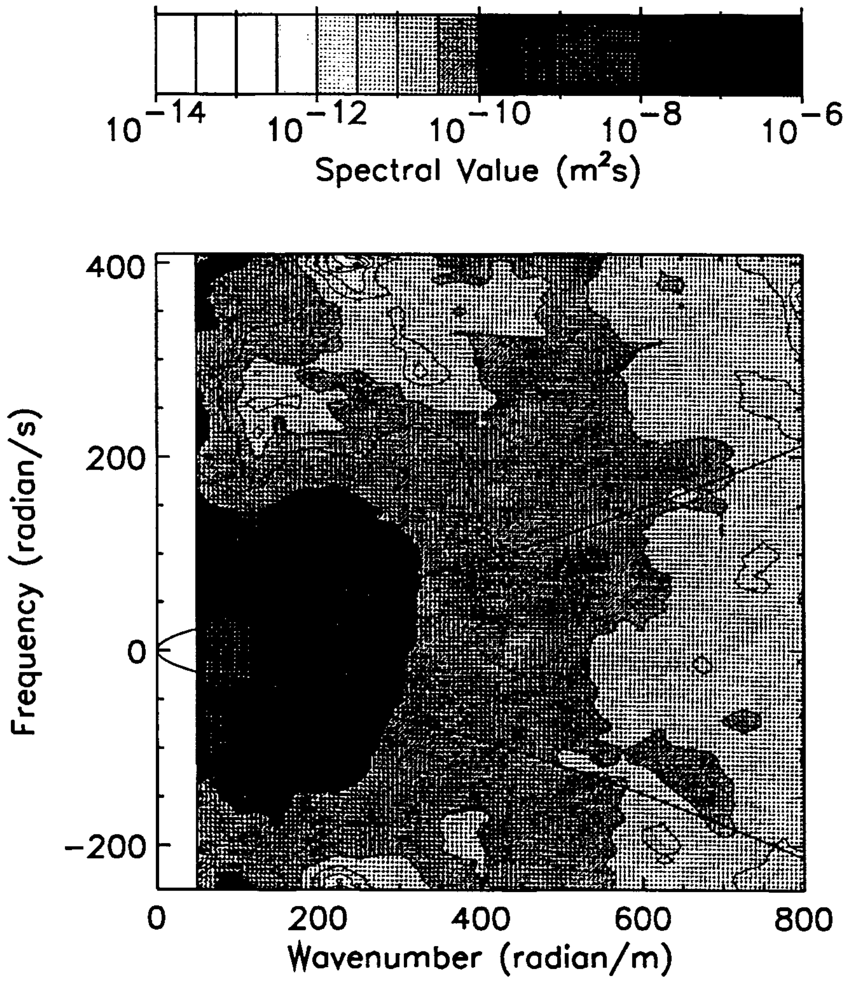

FIG. 9. Three-dimensional wavenumber–frequency slope spectrum corresponding to upper large circle in Fig. 7 for alongwind direction. Here $u_* = 0.24$ m s^{-1}. Solid line: dispersion relation. Contours are at every 2.5 dB.

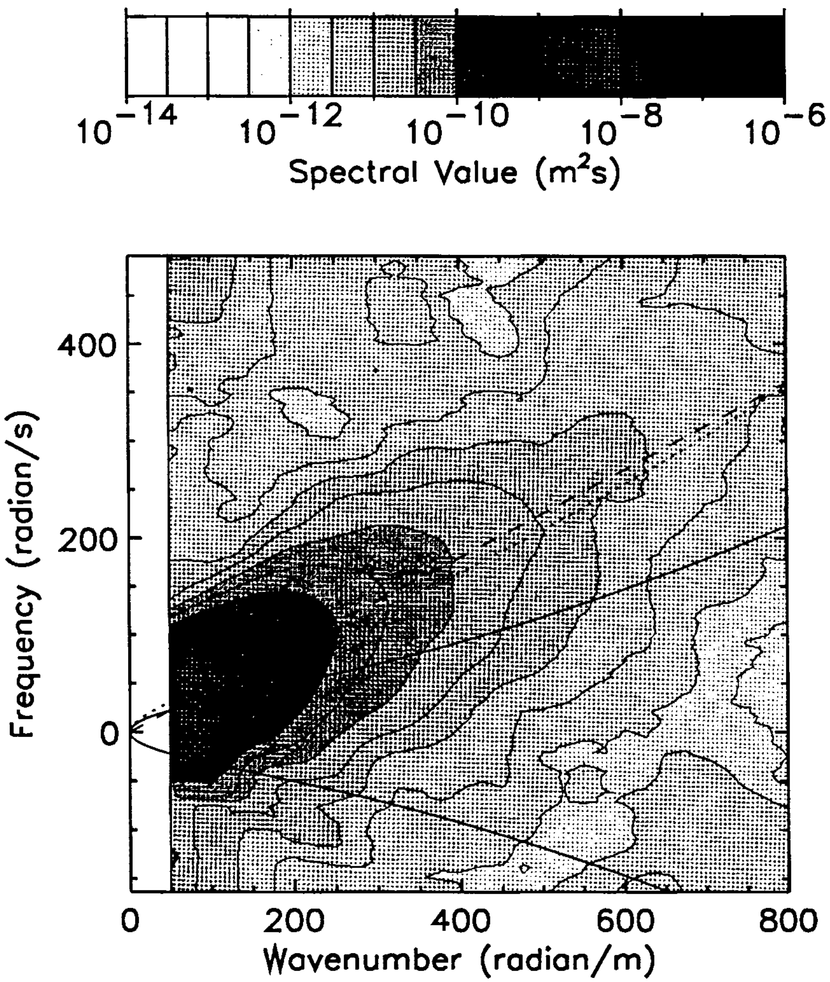

FIG. 10. Three-dimensional wavenumber–frequency slope spectrum corresponding to lower large circle in Fig. 7 for alongwind direction. Here $u_* = 0.24$ m s^{-1}. Solid line: dispersion relation; dotted line: dispersion relation with surface drift 0.27 m s^{-1}; dashed line: phase speed of gravity waves of $k = 49$ rad m^{-1}. Contours are at every 2.5 dB.

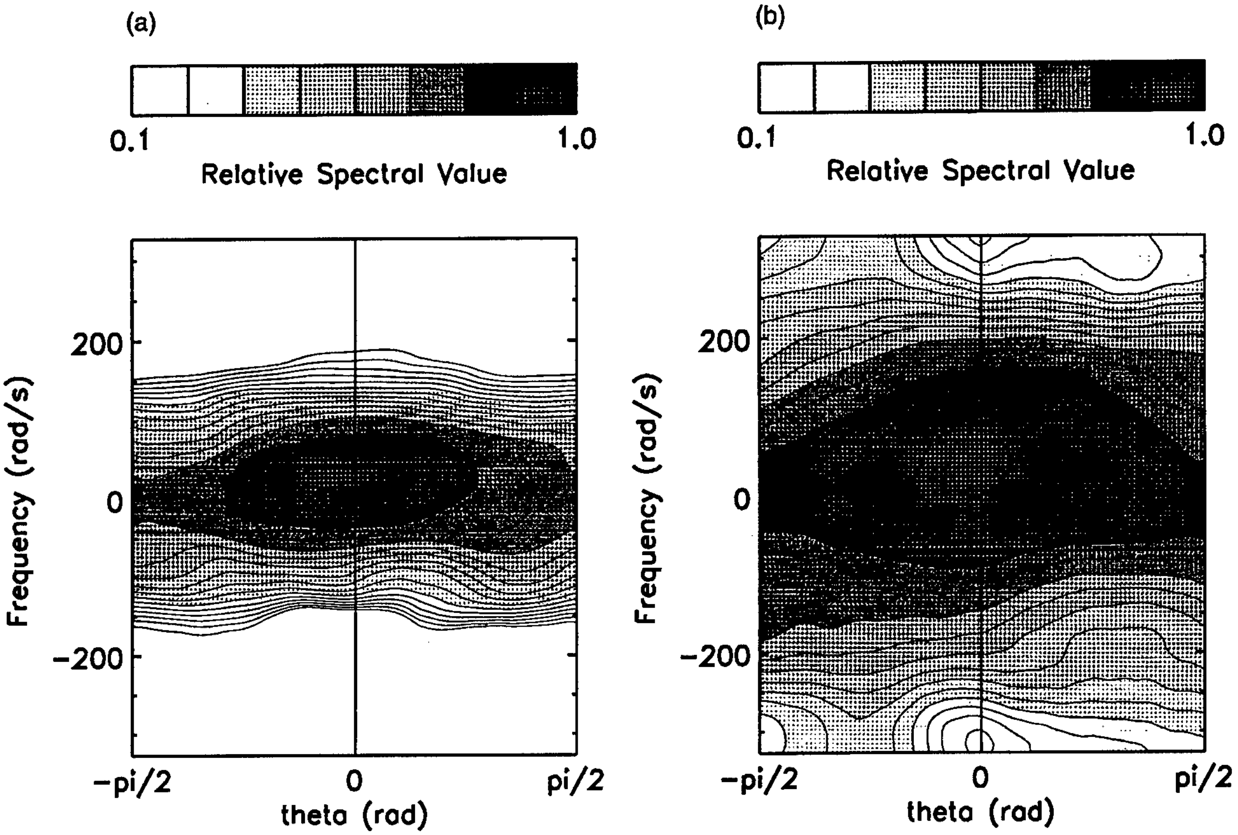

FIG. 11. Three-dimensional directional frequency slope spectrum (relative to maximum) corresponding to upper large circle in Fig. 7 for (a) k = 150 rad m^{-1} and (b) k = 300 rad m^{-1}. Here u_* = 0.24 m s^{-1}. Solid line: dispersion relation. Contours are at every 0.625 dB.

in the wind direction relative to the bulk current measured by the ADCP, the theoretical dispersion relation is shifted to the dotted lines in Figs. 10 and 12 and becomes quite consistent with the observed wave spectrum. Here, the Doppler-shifted frequency ω_D is given as

$$\omega_D = \omega + uk\cos\theta, \qquad (9)$$

where u is the assumed near-surface current velocity and ω is given by (8). This explanation, however, does not provide the reason why the waves propagating against the wind are preferentially damped by surface films, nor the reason why the Doppler shift by longer gravity waves of alongwind waves is reduced in the presence of surface films (since longer gravity waves are not expected to be influenced by surface films). Note that a possible change of the dispersion relation due to a modified surface tension (γ) by surface films is negligibly small compared to the Doppler shift of this magnitude.

An alternative explanation is that the short wind waves in Figs. 10 and 12 are not propagating freely but are bound to steep gravity waves. Then the shorter waves in the wind direction (i.e., the higher harmonics of the gravity waves) should appear to propagate at the same phase speed as the steep gravity waves rather than at their own phase speeds. Furthermore, if there is short-crested (i.e., two-dimensional) small-scale surface roughness that propagates with the gravity waves, its frequency–wavenumber spectrum should be concentrated near the apparent frequency of

$$\omega_B = kC\cos\theta, \qquad (10)$$

where C is the phase speed of the gravity waves. In Figs. 10 and 12, we have added ω_B (dashed lines) for a chosen phase speed of $C = 0.45$ m s^{-1} that corresponds to gravity waves of k = 49 rad m^{-1} or the wavelength of 0.13 m. The observed spectrum seems to follow the dashed lines as closely as it follows the dotted lines. Therefore, it may be interpreted that surface films have almost eliminated freely propagating shorter wind waves and that only the higher harmonics of steep gravity waves are measurable. This explanation is also consistent with the disappearance of the waves propagating against the wind and the reduction of the Doppler shift of alongwind waves. Note that the spectral level in Fig. 9 is higher everywhere in the k–ω plane than that in Fig. 10. Therefore, it is possible that the higher harmonics of steep gravity waves are also present in Fig. 9 but are concealed by much higher freely propagating waves.

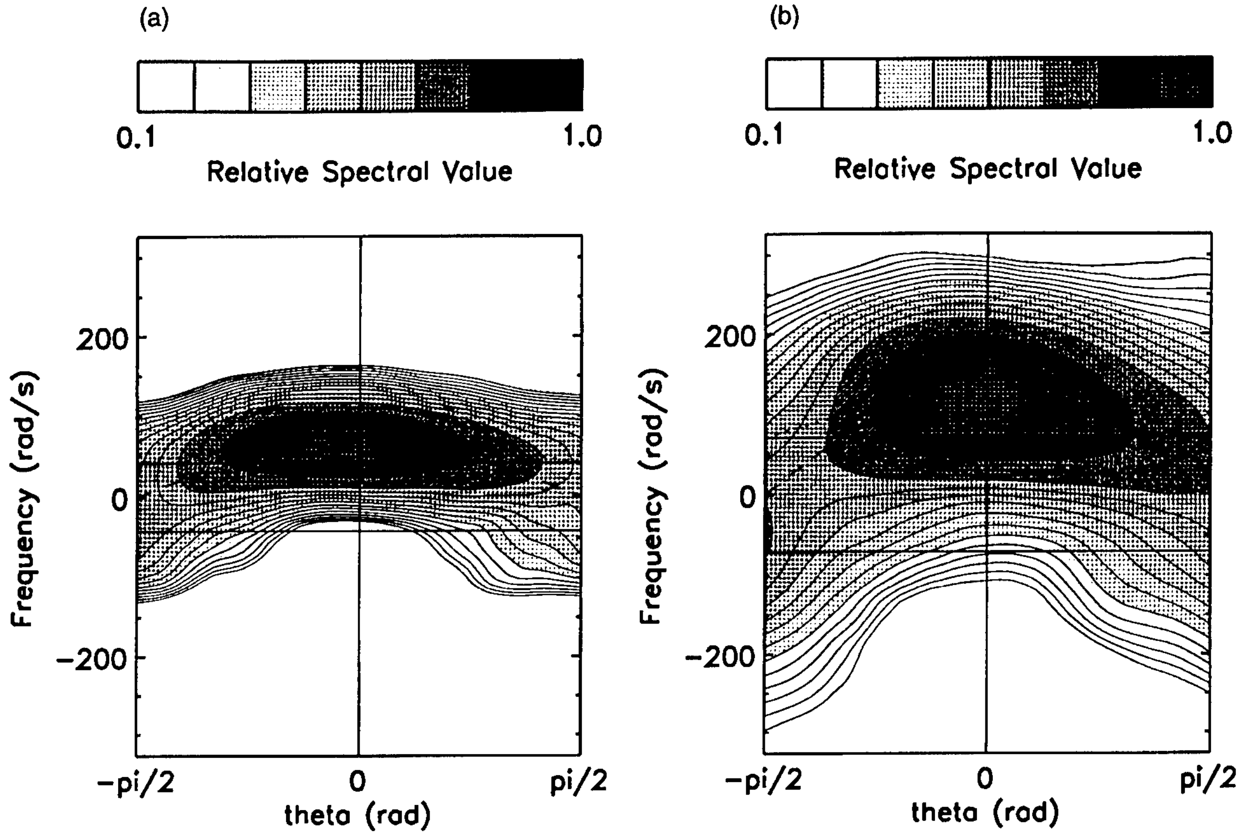

FIG. 12. Three-dimensional directional frequency slope spectrum (relative to maximum) corresponding to lower large circle in Fig. 7 for (a) $k = 150$ rad m^{-1} and (b) $k = 300$ rad m^{-1}. Here $u_* = 0.24$ m s^{-1}. Solid line: dispersion relation; dotted line: dispersion relation with surface drift 0.27 m s^{-1}; dashed line: phase speed of gravity waves of $k = 49$ rad m^{-1}. Contours are at every 0.625 dB.

One weakness of the second explanation is that there are no obvious reasons why a single component of gravity waves near $k = 49$ rad m^{-1} has to be so dominant in Fig. 10. The comparison of the integrated wavenumber slope spectra of both cases indicates that $k = 49$ rad m^{-1} roughly corresponds to a threshold wavenumber above which the spectrum is reduced by surface films (the spectral values corresponding to Fig. 10 are 98%, 69%, and 33% of those corresponding to Fig. 9 at wavenumbers 50, 100, and 200 rad m^{-1}, respectively). While this may explain why we do not see any bound harmonics of gravity waves above $k = 49$ rad m^{-1}, it is still not clear why no bound harmonics of longer gravity waves are observed.

In our recent laboratory studies of wind waves reported by Hara et al. (1997), we have found that a significant part of shortwave energy may be bound to dominant gravity waves in the wind–wave flume, depending on the wind and fetch conditions. Although simple extrapolations of laboratory results to field conditions cannot be made, it is noteworthy that certain common dispersion characteristics of short wind waves are observed both in laboratory studies and in field observations. Of course, without further independent physical measurements to augment these observations, we cannot reject the first explanation nor justify the second explanation.

At lower wind stresses between 0.15 and 0.25 m s^{-1} and with varying surface chemical enrichment levels, we have observed similar transitions of wave spectra between those characterized by broader Doppler shifting and significant levels of waves at negative frequencies such as Figs. 9 and 11 and those characterized by narrower Doppler shifting, negligible spectral levels at negative frequencies, and larger phase speeds than the theoretical dispersion relation such as Figs. 10 and 12. At very low wind stresses, however, wave spectra seem to follow the theoretical dispersion relation even in the presence of surface films. Such an example is shown in Fig. 13, which corresponds to the large square in Fig. 7. This may be simply due to the disappearance of the near-surface drift current, or because the longer gravity waves are not steep enough to generate higher bound harmonics at such low winds.

e. Directional wavenumber spectrum

Another way to observe the wave characteristics is to integrate the three-dimensional spectrum in frequency

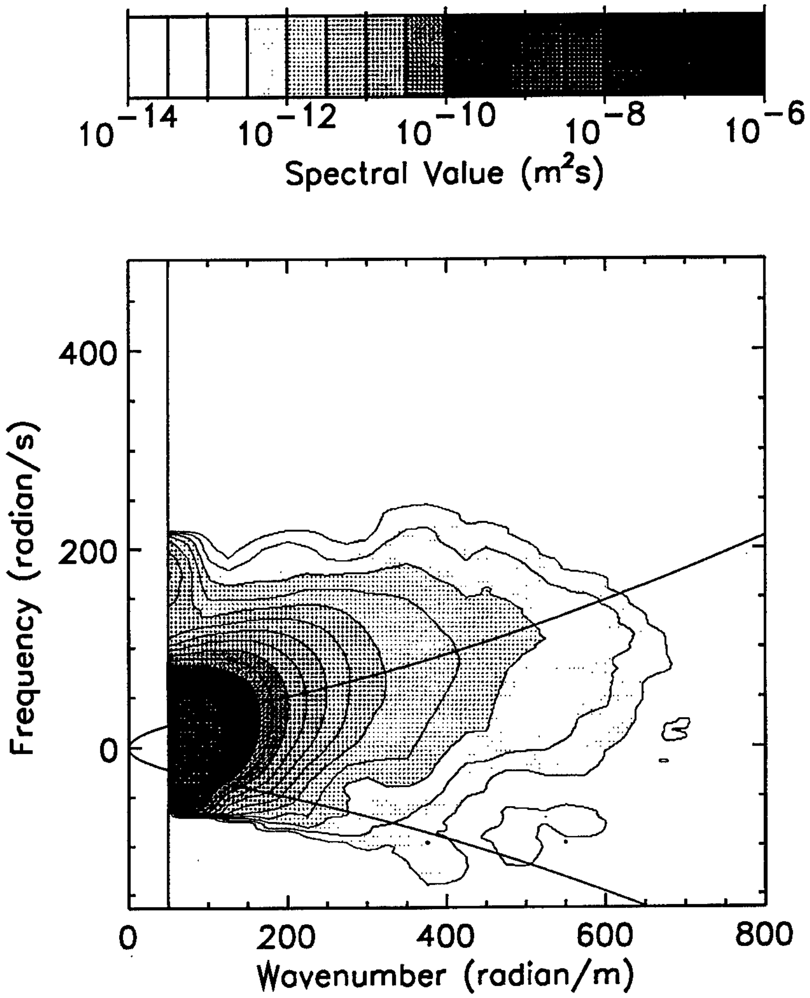

FIG. 13. Three-dimensional wavenumber–frequency slope spectrum corresponding to large square in Fig. 7 for alongwind direction. Here $u_* = 0.108$ m s^{-1}. Solid line: dispersion relation. Contours are at every 2.5 dB.

to obtain the two-dimensional (directional) wavenumber slope spectrum $S(k, \theta)$ or the directional degree of saturation $B(k, \theta)$. In Figs. 14 and 15, $B(k, \theta)$ is shown for the two cases corresponding to Figs. 9 and 10, respectively. At an earlier stage (Fig. 14), the directional spreading is quite uniform at higher wavenumbers. After 78 min in Fig. 15, shorter wind waves ($k > 300$ rad m^{-1}) show a more distinctive peak along the wind di-

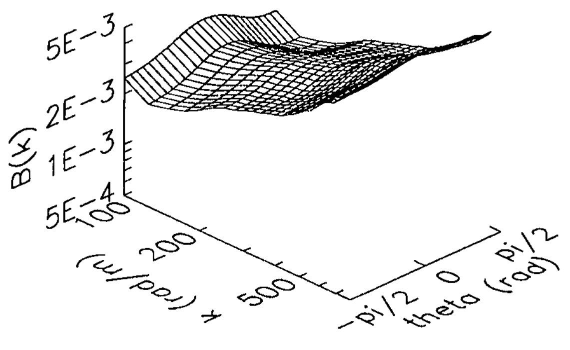

FIG. 14. Two-dimensional degree of saturation corresponding to upper large circle in Fig. 7. Here $u_* = 0.24$ m s^{-1}.

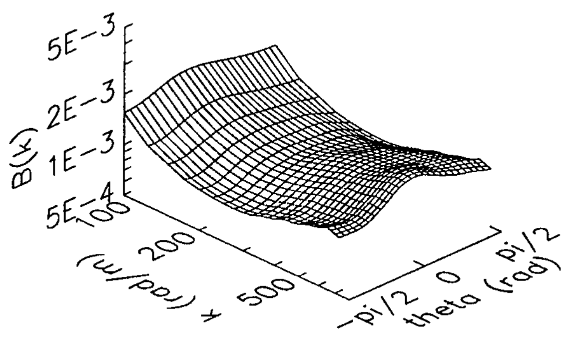

FIG. 15. Two-dimensional degree of saturation corresponding to lower large circle in Fig. 7. Here $u_* = 0.24$ m s^{-1}.

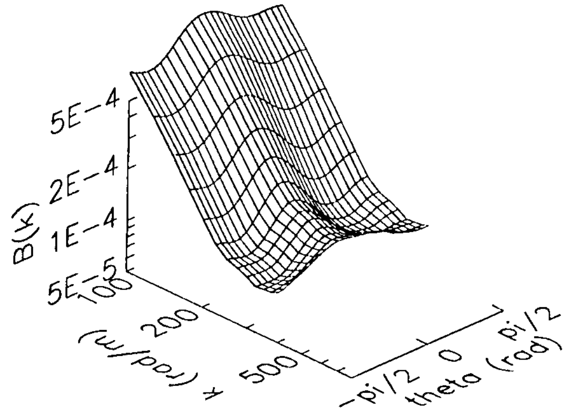

FIG. 16. Two-dimensional degree of saturation corresponding to large square in Fig. 7. Here $u_* = 0.108$ m s^{-1}.

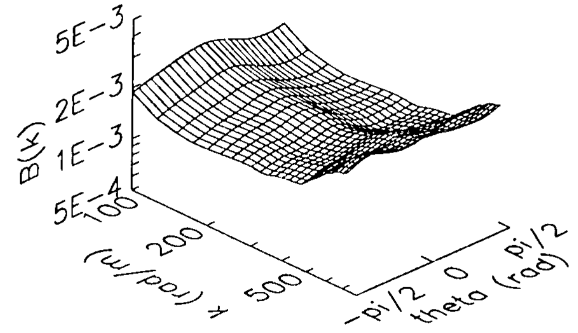

FIG. 17. Two-dimensional degree of saturation corresponding to large triangle in Fig. 7. Here $u_* = 0.090$ m s^{-1}.

rection, and the crosswind values are lower than the alongwind values by roughly 30%–40%. On the other hand, at lower wavenumbers ($k < 200$ rad m^{-1}) the directional spreading is quite broad. These are consistent with Figs. 11 and 12. The result at a very low wind friction velocity in Fig. 16 (corresponding to Fig. 13 and the large square in Fig. 7) shows a clear peak along the wind direction for the entire wavenumber range up to $k = 400$ rad m^{-1}, beyond which the wave signal becomes too noisy to resolve its directionality. On the other hand, the result at a similar low wind friction velocity but over a clean water surface in Fig. 17 (corresponding to the big triangle in Fig. 7) shows more uniform directional spreading.

4. Concluding remarks

Field observations have been made of wind-generated gravity–capillary waves during the Hi-Res II and the CoOP programs. Our results of short wind wave spectra over clean water compare reasonably with past field observations and show much higher values than laboratory results at lower winds and at higher wavenumbers. The results also show large variability in the presence of surface films; some results are lower than clean water values by more than one order of magnitude at higher wavenumbers. Our detailed investigations of the wavenumber–frequency spectra of short wind waves show that the dispersion characteristics vary significantly depending on the wavenumber, the wind stress, and the surface chemical conditions. On clean water, a significant part of the wave energy seems to belong to waves propagating against the wind. The apparent phase speed of short wind waves may increase in the presence of surface films, either by the enhancement of near-surface currents or by the relative increase of the wave energy that is bound to steep gravity waves.

With our limited observations, many questions remain unanswered. The large discrepancy between laboratory and field conditions does not seem to be attributable to the wind-fluctuation alone. Interactions between gravity–capillary waves and longer gravity waves may play an important role in determining the level of the slope spectrum. Although some of our observations may be suggestive of such interactions, they are far from comprehensive to draw any conclusions. Further progress on these issues may require simultaneous observations of waves in wide spatial and temporal ranges including capillary, gravity–capillary, and gravity waves. Many of our observations indicate that the dynamics of short wind waves are significantly nonlinear. Therefore, higher-order data analyses that explicitly account for the nonlinearity may be desirable.

Our observations imply that use of laboratory results requires much care for the study of air–sea interaction processes and for the application to microwave radar remote sensing. The large variability of short wind waves in coastal environments suggests the importance of surface chemistry in the study of small-scale air–sea interaction processes.

Acknowledgments. We thank Dr. Nelson M. Frew for providing surface film information, and Mr. B. Mete Uz for his assistance in spectral calculations. We also thank two anonymous reviewers for their helpful comments. This research was supported by NSF Grants OCE-9409222 (TH) and OCE-9410537 (EJB, JBE) and ONR Grants N00014-95-1-0116, N00014-96-1-0510 (TH), and N00014-90-J-1717, N00014-96-0516 (EJB, JBE).

APPENDIX

Error Analysis

Here, we summarize the error analyses of the scanning laser slope gauge. We have identified six possible sources of errors in Bock and Hara (1995); these are bias due to pitch/roll of the instrument, bias due to calibration, effect of a finite scan speed, statistical random errors, data dropouts, and numerical sidelobes. Here, we focus on the last two sources, since the first four are expected to be very small (less than ±1 dB).

a. Data dropouts

Data dropouts occur for two reasons: one being locally large surface slope that is outside the resolvable range of the instrument and the other being large gravity waves that yield water surface levels either below the top of the laser pod or above the bottom of the head unit.

The maximum resolvable surface slope is between 0.62 and 2.41, depending on the direction of the surface slope and the location of the laser beam. The most conservative estimate of the data dropout rate would be the probability of the surface slope exceeding 0.62. We have found that this probability is 2.9% and that the actual observed data dropout rate is only 0.7% at the friction velocity of $u_* = 0.3$ m s^{-1}. Therefore, this is not likely to be a major source of errors in the slope spectral estimate.

Data dropouts due to large gravity waves can be easily identified since the surface slope becomes either unmeasurable (when the top of the laser pod is above water) or zero (when the bottom of the head unit is below water). In order to avoid any possible data contaminations, we discard data for several seconds after each dropout. At the friction velocity $u_* = 0.3$ m s^{-1}, up to 50% of the data are discarded for this reason. It is possible that a high data dropout rate may bias the spectral estimate if dropouts occur at a particular phase of long waves and the spectral calculation excludes the gravity–capillary wave information from the vicinity of the particular phase of the long waves. Our visual observations, however, indicate that dropouts occur erratically because of the complicated dynamical response of the towed catamaran to waves. Therefore, we do not suspect that data dropouts due to large gravity waves introduce any significant bias to the spectral estimate.

b. Numerical sidelobes

The estimated two-dimensional wavenumber slope spectrum $\hat{S}(\mathbf{k})$ is a convolution integral of the real spectrum $S(\mathbf{k})$ and a convolution function $R(\mathbf{k})$ centered around the wavenumber of interest:

$$\hat{S}(\mathbf{k}) = \int_{-\infty}^{\infty}\int_{-\infty}^{\infty} S(\mathbf{k}')R(\mathbf{k}' - \mathbf{k})\,d\mathbf{k}'. \qquad \text{(A1)}$$

The shape of the convolution function R is determined by the spatial sampling rate and a chosen windowing function. In our spectral calculation, the convolution function has a narrow sharp peak at the origin and decreases rapidly away from the origin to about 10^{-4} relative to the peak, but increases again near the radius of 2000 rad m^{-1}. For example, the spectral estimate at $k = 800$ rad m^{-1} in the wind direction can be affected by waves at $k = 2800$ rad m^{-1} in the wind direction, at $k = 1833$ rad m^{-1} in the cross-wind directions, or at $k = 1200$ rad m^{-1} in the direction opposite to the wind. These effects are comparable to the aliasing (spectral foldover) in one-dimensional spectral analyses. In addition, the spectral estimate can be affected by waves near $k = 0$ rad m^{-1}, if the spectral level there is higher than that at $k = 800$ rad m^{-1} by more than four decades. It has been found that the leakage from the spectrum near $k = 0$ rad m^{-1} is so serious in field conditions that it sets a practical upper limit of the wavenumber resolution to be 800 rad m^{-1}. On the other hand, the aliasing from higher wavenumbers are expected to be small at this wavenumber since the slope spectrum always falls faster than k^{-1}.

c. Platform effect

In addition to the errors associated with the instrument, the platform (catamaran) may introduce systematic errors by disturbing the wind field, the wave field, and/or the near-surface current field. Although it is very difficult to quantify such effects, our visual observations suggest that the platform does not influence the wind–wave field as long as the catamaran is towed into the wind.

REFERENCES

Bock, E. J., and T. Hara, 1995: Optical measurements of capillary–gravity wave spectra using a scanning laser slope gauge. *J. Atmos. Oceanic Technol.,* **12,** 395–403.

Charnock, H., 1955: Wind stress on a water surface. *Quart. J. Roy. Meteor. Soc.,* **81,** 639.

Csanady, G. T., 1990: The role of breaking wavelets in air–sea gas-transfer. *J. Geophys. Res.,* **95,** 749–759.

Ebuchi N., H. Kawamura, and Y. Toba, 1987: Fine structure of laboratory wind–wave surfaces studied using an optical method. *Bound.-Layer Meteor.,* **39,** 133–151.

Edson, J. B., J. E. Hare, and C. W. Fairall, 1998: Direct covariance flux estimates from mobile platforms at sea. *J. Atmos. Oceanic Technol.,* **15,** 547–562.

Fairall, C. W., and J. B. Edson, 1994: Recent measurements of the dimensionless turbulent kinetic energy dissipation function over the ocean. Preprints, *Second Int. Conf. on Air–Sea Interaction and on Meteorology and Oceanography of the Coastal Zone,* Lisbon, Portugal, Amer. Meteor. Soc., 224–225.

——, E. F. Bradley, D. P. Rodgers, J. B. Edson, and G. S. Young, 1996: Bulk parameterization of air–sea fluxes for Tropical Ocean Global Atmosphere Coupled Ocean–Atmosphere Response Experiment. *J. Geophys. Res.,* **101,** 3747–3764.

Hara, T., E. J. Bock, and D. Lyzenga, 1994: In situ measurements of capillary–gravity wave spectra using a scanning laser slope gauge and microwave radars. *J. Geophys, Res.,* **99,** 12 593–12 602.

——, ——, N. M. Frew, and W. R. McGillis, 1995: Relationship between air–sea gas transfer velocity and surface roughness. *Air–Water Gas Transfer,* B. Jähne and E. C. Monahan, Eds., AEON Verlag, 611–616.

——, ——, and M. Donelan, 1997: Frequency–wavenumber spectrum of wind-generated gravity-capillary waves. *J. Geophys, Res.,* **102,** 1061–1072.

Hwang, P. A., D. B. Trizna, and J. Wu, 1993: Spatial measurements of short wind waves using a scanning slope sensor. *Dyn. Atmos. Oceans,* **20,** 1–23.

——, S. Atakturk, M. A. Sletten, and D. B. Trizna, 1996: A study of the wavenumber spectra of short water waves in the ocean. *J. Phys. Oceanogr.,* **26,** 1266–1285.

Jähne, B. K., and K. S. Riemer, 1990: Two-dimensional wave number spectra of small-scale water surface waves. *J. Geophys. Res.*, **95,** 11 531–11 546.

——, O. Münnich, R. Bösinger, A. Dutzi, W. Huber, and P. Libner, 1987: On the parameters influencing air–water gas exchange. *J. Geophys. Res.*, **92,** 1937–1949.

Kolmogorov, A. N., 1941: Energy dissipation in locally isotropic turbulence. *Dokl. AN SSSR,* **32,** 19–21.

Zhang, X., 1995: Capillary–gravity and capillary waves generated in a wind wave tank: Observations and theories. *J. Fluid Mech.,* **289,** 51–82.

Similarity Relationships in the Marine Atmospheric Surface Layer for Terms in the TKE and Scalar Variance Budgets*

J. B. EDSON

Woods Hole Oceanographic Institution, Woods Hole, Massachusetts

C. W. FAIRALL

NOAA/Environmental Technologies Laboratory, Boulder, Colorado

(Manuscript received 3 September 1996, in final form 25 October 1997)

ABSTRACT

Measurements of the momentum, heat, moisture, energy, and scalar variance fluxes are combined with dissipation estimates to investigate the behavior of marine surface layer turbulence. These measurements span a wide range of atmospheric stability conditions and provide estimates of z/L between -8 and 1. Second- and third-order velocity differences are first used to provide an estimate of the Kolmogorov constant equal to 0.53 ± 0.04. The fluxes and dissipation estimates are then used to provide Monin–Obukhov (MO) similarity relationships of the various terms in the turbulent kinetic energy (TKE) and scalar variance (SV) budgets. These relationships are formulated to have the correct limiting forms in extremely stable and convective conditions. The analyses concludes with a determination of updated dimensionless structure function parameters for use with the inertial–dissipation flux method.

The production of TKE is found to balance its dissipation in convective conditions and to exceed dissipation by up to 17% in near-neutral conditions. This imbalance is investigated using the authors' measurements of the energy flux and results in parameterizations for the energy flux and energy transport term in the TKE budget. The form of the dimensionless energy transport and dimensionless dissipation functions are very similar to previous parameterizations. From these measurements, it is concluded that the magnitude of energy transport (a loss of energy) is larger than the pressure transport (a gain of energy) in slightly unstable conditions.

The dissipation of SV is found to closely balance production in near-neutral conditions. However, the SV budget can only be balanced in convective conditions by inclusion of the transport term. The SV transport term is derived using our estimates of the flux of SV and the derivative approach. The behavior of the derived function represents a slight loss of SV in near-neutral conditions and a gain in very unstable conditions. This finding is consistent with previous investigations.

The similarity between these functions and recent overland results further suggests that experiments are generally above the region where wave-induced fluctuations influence the flow. The authors conclude that MO similarity theory is valid in the marine surface layer as long as it is applied to turbulence statistics taken above the wave boundary layer.

. Introduction

Our understanding of the behavior of turbulence in ne atmospheric surface layer was vastly improved by number of overland field experiments conducted durng the late 1960s and 1970s. These include the landnark 1968 Kansas (Izumi 1971) experiment, the 1973 innesota (Champagne et al. 1977) experiment, and the 976 International Turbulence Comparison Experiment Dyer and Bradley 1982). These experiments led to the validation of a powerful set of statistical tools derived from Monin–Obukhov similarity theory. The semiempirical relationships derived from their carefully conducted measurements are now used extensively in the lower boundary conditions of numerical forecast models where one must derive turbulent quantities from the mean variables available from the model. Similarly, these relationships are often used to estimate the desired turbulent quantities from mean measurements over the ocean where direct measurement of the fluxes is very difficult. However, the use of overland measurements to infer surface fluxes over the open ocean raises questions about the universality of these relationships.

There have been a number of experiments to investigate the structure of atmospheric turbulence in the marine boundary layer (Smith et al. 1996). These include the 1969 Barbados Oceanographic and Meteorological

---

* WHOI Contribution Number 9316.

Corresponding author address: Dr. James B. Edson, WHOI 1S#10, 98 Water Street, Woods Hole, MA 02543.
-mail: jedson@whoi.edu

Experiment (Keuttner and Holland 1969) and the 1974 North Pacific Experiment (Schmitt et al. 1979). Both of these experiments were conducted aboard the Floating Instrument Platform (R/P *FLIP*), which allows researchers to make flux measurements over the open ocean from a stable platform. Though these experiment were successful on many fronts, they both suffered from the now well-known (but still difficult to overcome) problem of sea salt contamination of their temperature probes (Schmitt et al. 1978). Large and Pond (1981, 1982) used the Bedford Institute of Oceanography spar buoy plus ship data in a landmark study of fluxes and transfer coefficients over a broad range of wind speeds.

The 1986 Humidity Exchange Over the Sea (HEXOS) (Katsaros et al. 1987) main experiment deployed instrumentation designed to avoid environmental contamination problems. This effort included a number of instruments designed to remove the effects of sea spray (Katsaros et al. 1994), as well as the use of sonic thermometers to compute the temperature fluctuations (Larsen et al. 1993). The HEXOS investigations were conducted from a platform located 10 km off the Dutch coast. The results from this experiment confirmed a number of earlier results, for example, that the production of turbulence kinetic energy (TKE) is closely balanced by its dissipation (Edson et al. 1991) and that the drag coefficient is a function of wave age at a given wind speed (Smith et al. 1992; Maat et al. 1991). The experiment also demonstrated that the transfer coefficients for temperature and humidity were only weakly dependent on wind speed (DeCosmo et al. 1996), although the significance of these results remains a hotly debated topic (e.g., Katsaros and de Leeuw 1994; Andreas 1994; Andreas et al. 1995).

In recent years, a number of researchers have made a great deal of progress in computing direct covariance flux estimates from ocean-going platforms (e.g., Fujitani 1981, 1985; Tsukamoto et al. 1990; Bradley et al. 1991; Fairall et al. 1997; Edson et al. 1998). In the case of moving platforms, this requires systems that are capable of removing platform motion from our velocity measurements before computing the fluxes (Fujitani 1985). This generally involves the integration of linear accelerometers and angular rate sensors to compute the high-frequency motion of the platform that are combined with the low-frequency velocity measurements from global positioning systems and/or current meters (e.g., Edson et al. 1998). Similar measurements from buoy mounted instrumentation can be found in Anctil et al. (1994). For example, direct covariance flux estimates were collected from ship-mounted systems during the Tropical Ocean Global Atmosphere (TOGA) Coupled Ocean–Atmosphere Response Experiment (COARE) in the equatorial Pacific Ocean (Webster and Lukas 1992). These flux estimates have been used to develop a bulk algorithm based on the parameterizations proposed by Liu et al. (1979), Smith (1988), and Godfrey and Beljaars (1991). The hybrid model includes new semiempirical formulas that improve the performance of the code in very convective conditions as reported by Fairall et al. (1996a) and Fairall et al. (1996b).

Despite the emergence of covariance flux measurements from ships, interest remains high in the inertial–dissipation flux estimation method (Large and Pond 1982; Fairall and Larsen 1986). Papers frequently appear in the literature using this method (e.g., Anderson 1993; Yelland and Taylor 1996; Fairall et al. 1996a; Frederickson et al. 1997), which is now being used extensively on buoy-based systems (Skupneiwicz and Davidson 1991; Yelland et al. 1994). It is clear that inertial–dissipation stress data give much lower scatter than covariance estimates (Fairall et al. 1996a) and there is substantial evidence that covariance stresses are much more influenced by flow distortion (Edson et al. 1991; Oost et al. 1994).

Inertial–dissipation measurements still represent the vast majority of data used to determine the drag coefficient over the open ocean at wind speeds greater than 20 m s^{-1}. The disadvantage of this method is that it relies on Monin–Obukhov similarity and requires specification of the dimensionless structure function parameters. These are empirical functions and the method is uncertain to the extent that these functions are uncertain. Forms of these functions determined over Kansas are still being used (Wyngaard and Cote 1971; Wyngaard et al. 1971a,b), but demands for ever-increasing accuracy in flux estimates and bulk transfer coefficients require us to continually refine these functions.

In this paper we present an analysis of data recently taken in the marine surface layer aboard the R/P *FLIP* and the R/V *Columbus Iselin*. These new measurements feature direct eddy correlation stress and heat flux estimates, and TKE and scalar variance (SV) dissipation computed from the inertial subrange of the velocity, temperature, and specific humidity spectra. The high-frequency velocity and temperature measurements were made using sonic anemometers–thermometers, while the specific humidity measurements were made using infrared hygrometers. The data collected during these two experiments cover a much wider stability range than any of the above mentioned datasets. In particular, the extremely unstable data will allow us to examine the behavior of the turbulence statistics in the free convective limit.

The focus of this investigation is the evaluation of the components of the TKE and SV budgets and their relationship to the inertial subrange variables. Our goal is to verify and extend the overland results for application over the oceans including a closer look at the relative balance of turbulent and pressure transport in the TKE budget. In the sections that follow we begin with a brief overview of Monin–Obukhov similarity theory. This is followed by a description of the field programs, the instruments, and the data processing techniques in section 3. Dissipation estimates and evaluation of the Kolmogorov constant using the skewness relaons of Kolmogorov (1941) are discussed in section 4. 'he TKE budget is evaluated in section 5; the SV budets in section 6; and the dimensionless structure funcon parameters are given in section 7.

. Similarity theory

The structure of the turbulent flow in the surface layer influenced by both mechanical and thermal forcing. 'bukhov (1946) and Monin and Obukhov (1954) were ie first to describe a similarity hypothesis about the atistical nature of the turbulent flow based on the rel-ive strength of these two forcing mechanisms. Monin–'bukhov (hereafter MO) similarity theory states that ie structure of turbulence is determined by the height ove the surface z, the buoyancy parameter $g/\overline{\Theta}_v$, the iction velocity u_*, and the surface buoyancy flux $\overline{w\theta_v}_0$, here $\overline{\Theta}_v$ is the virtual potential temperature and g is ie acceleration of gravity (e.g., Wyngaard 1973). These st two terms are defined from the surface stress and eat fluxes as

$$u_* = \left[\frac{|\boldsymbol{\tau}_0|}{\rho}\right]^{1/2}, \qquad (1)$$

$$\overline{w\theta_{v_0}} = \frac{Q_0}{\rho c_p} + 0.61T_0\frac{E_0}{\rho L_e}, \qquad (2)$$

here $\boldsymbol{\tau}_0$ is the surface stress vector (the surface value the momentum flux), Q_0 is the surface value of the nsible heat flux, E_0 is the surface value of the latent at flux, ρ is the density of air, c_p is the specific heat constant pressure, and L_e is the latent heat of vapor-ation of water.

One of the basic assumptions of MO similarity theory that these fluxes are constant with height in the surface yer. In reality, this constant flux assumption is never lly valid in the atmospheric boundary layer. However, good approximation to this constant flux assumption obtained if we define the top of the surface layer as at height where the momentum flux is 90% of its rface value. Since the momentum flux generally de-eases linearly with height, this definition results in a rface layer that occupies the lowest 10% of the at-ospheric boundary layer.

The unstable marine boundary layers studied in this per were typically 500–700 m in height, which results a surface layer height of approximately 60 m. This ows us to estimate the surface fluxes from our co-riance measurements (made at about 12 m height) as

$$\frac{\boldsymbol{\tau}_0}{\rho} \approx \frac{\boldsymbol{\tau}}{\rho} = -\mathbf{i}\overline{uw} - \mathbf{j}\overline{vw}, \qquad (3)$$

$$Q_0 \approx Q = \rho c_p\overline{w\theta}, \qquad (4)$$

$$E_0 \approx E = \rho L_e\overline{wq}, \qquad (5)$$

iere u, v, and w are longitudinal, lateral, and vertical velocity fluctuations, respectively; θ are temperature fluctuations; and q are specific humidity fluctuations.

a. The marine surface layer

In addition to the constant flux layer constraint, the application of MO similarity theory to the marine surface layer requires some caution because the scaling parameters are only meant to account for the influence of mechanical and thermal forcing on the turbulence. Many investigations such as those by Geernaert et al. (1986), Rieder et al. (1994), Donelan et al. (1993), and Hare et al. (1997) have demonstrated that additional scaling parameters are required to describe turbulent variables within the wave boundary layer (WBL). The WBL is defined in this paper as the layer where the total momentum flux, even if assumed to be constant with height, has appreciable turbulent and wave-induced components. That is, within the WBL the momentum equation can be written as

$$\frac{\partial}{\partial z}\left(-\overline{\tilde{u}\tilde{w}} - \overline{u'w'} + \nu\frac{\partial\overline{U}}{\partial z}\right) \approx 0, \qquad (6)$$

where primes denote turbulent fluctuations, tildes denote the wave-induced fluctuations, $\overline{U}$ is the mean wind [i.e., $U(t) = \overline{U} + u'(t) + \tilde{u}(t) = \overline{U} + u(t)$], and the last term on the right-hand side represents the viscous stress where ν is the kinematic viscosity.

To examine the applicability of MO similarity theory in the marine surface layer, we are limiting our analyses to observations where the flow is not expected to be influenced by wave-induced fluctuations. We believe that we are meeting this constraint based on the fact that the measurement heights for the R/P *FLIP* (12 m) and R/V *Iselin* (11.5 m) are generally larger than the reciprocal wavenumber of the dominant wind waves, k_w^{-1}, observed during our respective cruises (i.e., in general, $k_wz > 1$). Therefore, although we have reason to believe that we are experiencing wave-induced effects at our highest winds (see section 8), we believe that most of our dataset is characteristic of a surface layer where the turbulent fluxes dominate the total flux and MO similarity theory is applicable.

b. Monin–Obukhov scaling

Monin–Obukhov similarity theory is covered in detail in a number of texts, including Lumley and Panofsky (1963) and Wyngaard (1973). For the purposes of this paper we briefly describe the basis MO similarity theory by first combining the four governing parameters to form an additional velocity scale defined as

$$u_f = \left(\frac{zg}{\overline{\Theta}_v}\overline{w\theta_{v_0}}\right)^{1/3}, \qquad (7)$$

whose use is restricted to positive values of the heat flux (i.e., convective conditions). The two velocity scales, u_* and u_f, are then used to define two temperature and moisture scales,

$$T_* = -\frac{\overline{w\theta_0}}{u_*}, \qquad T_f = -\frac{\overline{w\theta_0}}{u_f}, \tag{8}$$

$$q_* = -\frac{\overline{wq_0}}{u_*}, \qquad q_f = -\frac{\overline{wq_0}}{u_f}, \tag{9}$$

and a length scale now known as the Monin–Obukhov length,

$$L = -\frac{\overline{\theta}_v}{g\kappa}\frac{u_*^3}{\overline{w\theta_0}}, \tag{10}$$

where κ is the von Kármán constant. The magnitude of the MO length is determined by the relative strength of the mechanical versus thermal forcing, while its sign is determined by the sign of the buoyancy flux; that is, it is negative in convective (unstable) conditions and positive in stratified (stable) conditions.

The various scales are not independent (Wyngaard 1973) as they can be combined to obtain

$$\frac{u_f}{u_*} = \left(-\frac{z}{\kappa L}\right)^{1/3} \tag{11}$$

and

$$\frac{T_f}{T_*} = \frac{q_f}{q_*} = \left(-\frac{z}{\kappa L}\right)^{-1/3} \tag{12}$$

in convective conditions. Therefore, it is common practice to select u_*, T_*, and q_* as the velocity, temperature, and moisture scales for both stable and unstable flows. The similarity hypothesis then states that various turbulent statistics, when normalized by these scaling parameters, are a universal function of z/L. This hypothesis has been validated by a number of studies in the atmospheric boundary layer over land. Notable examples include the studies by Dyer and Hicks (1970), Wyngaard and Coté (1971), Kaimal et al. (1972), Champagne et al. (1977), and Dyer and Bradley (1982).

In light winds conditions with appreciable heat flux, MO similarity theory requires that the surface stress (i.e., u_*) is no longer a relevant scaling parameter and that the small-scale turbulence variables approach the convective limits. In this limit the structure of the marine atmospheric surface layer in the region between $-L < z < 0.1\,z_i$ should approach that of local free convection and depend only on z, $g/\overline{\Theta}_v$, and $\overline{w\theta_{v0}}$ (Tennekes 1970). Under these conditions it is more appropriate to use the convective scaling parameters denoted by the subscript f. Additionally, above the surface layer (i.e., $z > 0.1\,z_i$), studies of the mixed layer have shown that many turbulent processes scale with the height of the boundary layer, z_i. In this region, z_i replaces z as the appropriate length scale and one uses the free-convective velocity scale proposed by Deardorff (1970):

$$w_* = \left(\frac{z_i g}{\overline{\Theta}_v}\overline{w\theta_{v0}}\right)^{1/3}. \tag{13}$$

Overland studies involving this type are scaling analysis have been reported by Wyngaard et al. (1978), Wyngaard and LeMone (1980), and Højstrup (1982).

3. Field programs and data processing

In this paper we present analyses of data taken in two recent experiments in the marine surface layer aboard the R/P *FLIP* and the R/V *Columbus Iselin.* These two experiments used similar instruments, data acquisition systems, and processing techniques to estimate the turbulent statistics. One experiment was an open ocean location just outside the islands off Los Angeles, California; the other was in the vicinity of the Gulf Stream edge off Cape Hatteras. Details about the instruments and basic processing are provided in this section. The overall quality of the covariance fluxes is illustrated by comparison with bulk flux estimates.

The R/P *FLIP* was deployed off the west coast of southern California for a 2-week period during the second half of September 1993 as part of the San Clemente Ocean Probing Experiment described in Kropfli and Clifford (1994). The R/P *FLIP* was positioned off San Clemente Island, California (33°N, 118°W). Data were obtained in the wind-speed range from 0.5 to 12 m s^{-1}, with sea–air temperature differences from 0° to 4°C. The Environmental Technologies Laboratory's ship flux measurement system was used. This system is described in detail by Fairall et al. (1997), so only a brief sketch will be given here.

A sonic anemometer–thermometer is used to make measurements of the stress and buoyancy flux, and a fast-response infrared hygrometer is used with the sonic anemometer to obtain the latent heat flux. A dual inertial navigation system is used to correct for ship motions (Edson et al. 1998). Fluxes were computed using covariance, inertial–dissipation, and bulk techniques. Sea surface temperature is derived from bulk water measurements at a depth of 5 cm with a floating thermistor and the corrections for the cool skin effect described in Fairall et al. (1996b). Mean air temperature and humidity are derived from a conventional aspirated T/RH sensor; the infrared hygrometer provided redundant information. The instruments were deployed at the end of *FLIP*'s 20-m-long port boom. Editing for radio interference and fog contamination yielded 180 usable 50-min averages.

The second dataset was taken aboard the R/V *Columbus Iselin* in June 1993 as part of the Office of Naval Research's (ONR) High Resolution Program. The experiment was designed to investigate the cause of the surface features seen in remotely sensed images of the sea surface around the northern edge of the Gulf Stream. Sea surface temperatures in this region ranged between 22° and 29°C and often resulted in a change in the sign

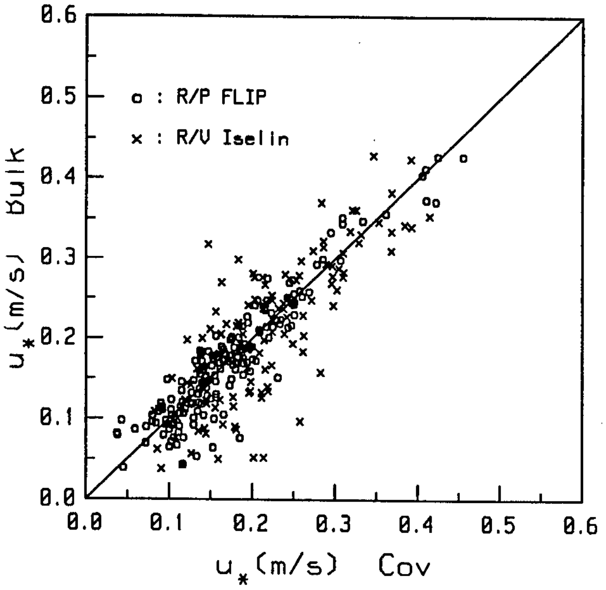

FIG. 1. A comparison of the friction velocities, u_*, estimated using ne bulk aerodynamic vs direct covariance methods. The friction veocity estimates for the R/P *FLIP* are computed from 50-min averages, hile the R/V *Iselin* estimates are taken from 30-min averages.

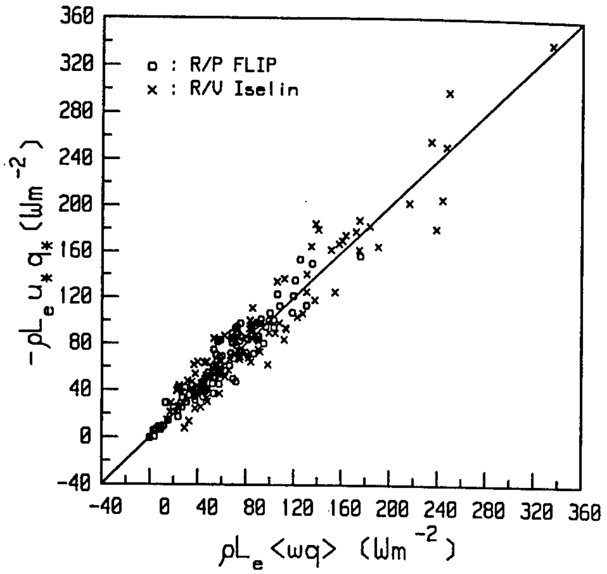

FIG. 2. A comparison of the latent heat fluxes estimated using the bulk aerodynamic vs direct covariance methods. The averaging times are as in Fig. 1.

f the stability as the ship crossed the Gulf Stream edge. he advection of warm air over cooler water during a ortion of the experiment resulted in a number of meaurements made under stable conditions. As a result, the ombined datasets cover a stability range $-8 < z/L <$, which allows us to investigate the scaling laws in the imits of both local free convection and extremely stable tratification.

Our estimates of the surface stress, and therefore u_*, re computed using the eddy correlation technique. Our stimates of the dissipation rate of TKE are determined rom the sonic velocity spectra as described in the folowing section. Our estimates of the dissipation rate of emperature and humidity variance are computed from e sonic temperature and infrared hygrometer humidity pectra, respectively. The Monin–Obukhov lengths were etermined using the buoyancy flux from the sonic anmometer and a von Kármán constant of 0.4.

The R/P *FLIP* and the R/V *Iselin* data were corrected r contamination due to platform motion using strapown accelerometers and rate sensors as described in Edn et al. (1998). The corrections on *FLIP* were much maller than on the *Iselin,* resulting in somewhat more ncertainty in the *Iselin* measurements. Additionally, the *elin* data exhibit more scatter near neutral stratification ecause these conditions are usually the result of being ear the Gulf Stream edge where conditions are inhoogeneous. In fact, we have found that the removal of a w data points where the sign of the heat flux does not atch the sign of the sea–air temperature greatly reduces e scatter in our comparisons. Therefore, we have taken is approach in the following analysis to remove data llected during very inhomogeneous conditions.

We compare our direct covariance estimates of the scaling parameters with bulk estimates calculated using the TOGA COARE algorithm (Fairall et al. 1996a) in Figs. 1–3. The present data are comparable to the COARE results, with *FLIP* data being significantly better for u_*, where motion corrections and flow distortion play a smaller role than in the ship-based measurements. Thus, the greater scatter in the *Iselin* estimates is most obvious in the u_* comparison given in Fig. 1. In this figure, the *Iselin* momentum flux estimates have been reduced by 15% (a 7% reduction in u_*) based on the R/P *FLIP* versus ship comparison presented in Edson et al. (1998), which accounts for the effect of flow distortion by the ship's superstructure. Once we have applied this correction we obtain very good agreement between the direct covariance and bulk momentum and heat flux estimates over a wide range of conditions. This is particularly true of the latent heat flux estimates shown in Fig. 2, which has been a difficult variable to measure directly (or even indirectly) over the open ocean.

4. Inertial–dissipation and third-order structure function estimates

a. *Inertial–dissipation estimates*

The dissipation rate of turbulent kinetic energy is one of the most widely used variables in investigations of both atmospheric and oceanic boundary layers. Direct measurements of the dissipation rate are usually accomplished by taking the spatial or time derivative of hotwire anemometers signals. The use of hot wires is necessary because the anemometers must be fast enough to measure fluctuations with a spatial resolution that

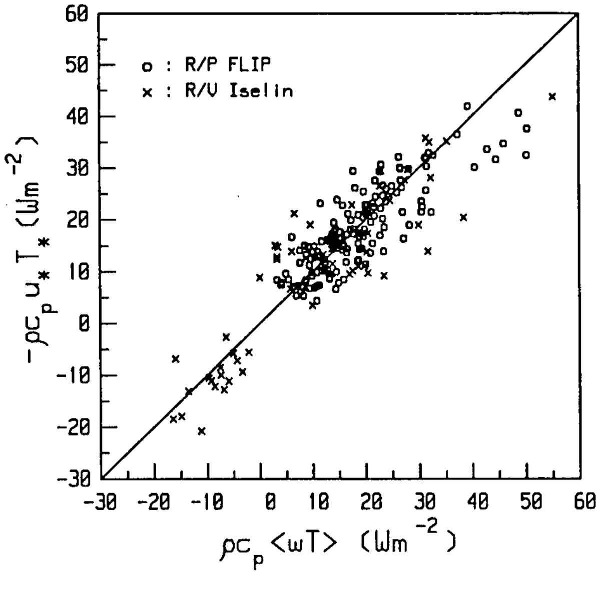

FIG. 3. A comparison of the sensible heat fluxes estimated using the bulk aerodynamic vs direct covariance methods. The averaging times are as in Fig. 1.

approaches the Kolmogorov microscale, $\eta = (\nu^3/\epsilon)^{1/4}$, which is typically 1 mm in atmospheric flows.

Unfortunately, the use of hot-wire anemometry over the ocean is severely limited by the contamination and frequent destruction of the wires by sea spray. As a result, dissipation rates in the atmospheric marine surface layer are usually computed from one-dimensional variance spectra measured with sonic anemometers. In the inertial subrange of isotropic turbulence, the one-dimensional velocity variance spectrum Φ_u can be expressed as a function of wavenumber magnitude,

$$\Phi_u(k) = \alpha_u \epsilon^{2/3} k^{-5/3}, \tag{14}$$

where ϵ is the dissipation of TKE into heat, k is the wavenumber, and α_u is the one-dimensional Kolmogorov constant. These spectra can be related to the frequency spectra S_u, commonly measured in the field using Taylor's hypothesis (here, $k = 2\pi f/\overline{U}$) as

$$k\Phi_u(k) = \frac{fS_u(f)}{T_{uu}} = \alpha_u \epsilon^{2/3} \left(\frac{2\pi f}{\overline{U}}\right)^{-2/3}, \tag{15}$$

where T_{uu} is a factor that corrects for inaccuracies in using Taylor's hypothesis to estimate the magnitude of wavenumber spectra in the inertial subrange. We use the form given by Wyngaard and Clifford (1977),

$$T_{uu} = 1 - \frac{1}{9}\frac{\sigma_u^2}{(\overline{U})^2} + \frac{2}{3}\frac{(\sigma_v^2 + \sigma_w^2)}{(\overline{U})^2}, \tag{16}$$

where the standard deviations are computed from the same time series that produced the spectral estimate (Hill 1996). This correction reduces our spectral estimates by an average of 2%. Therefore, (15) can be used to find estimates of the dissipation rates from our longitudinal velocity spectra if we know the value of the Kolmogorov constant. Estimate of this constant have been determined from direct measurement of ϵ using hot-wire anemometry in several overland experiments. A review of these measurements by Högström (1996) suggested a value of 0.52.

b. Third-order structure function dissipation estimates

Another method that can be use to measure ϵ and determine the Kolmogorov constants relies on the skewness coefficient for the distribution of velocity differences as described by Kolmogorov (1941). The skewness

$$S = \frac{B_{uuu}(r)}{[B_{uu}(r)]^{3/2}} \tag{17}$$

is computed using the ratio of the second- and third-order velocity differences,

$$B_{uu}(r) = \overline{[U(x) - U(x + r)]^2}, \tag{18}$$

$$B_{uuu}(r) = \overline{[U(x) - U(x + r)]^3}, \tag{19}$$

where $U(x)$ and $U(x + r)$ are instantaneous longitudinal velocity measurements separated by a distance, r, in the direction of the longitudinal wind. In the inertial subrange these parameters are related to the structure function parameter C_u^2 and the dissipation rates by

$$\frac{B_{uu}(r)}{r^{2/3}} = C_u^2 = 4.0\alpha_u \epsilon^{2/3} \tag{20}$$

and

$$\frac{B_{uuu}(r)}{r} = -\frac{4}{5}\epsilon. \tag{21}$$

Based on these expressions, Kolmogorov (1941) hypothesized that in the inertial subrange the skewness should remain constant. Using this hypothesis and the above equations, Kolmogorov obtained an expression that can be used to compute the one-dimensional Kolmogorov constant as

$$\alpha_u = \left(-\frac{1}{10S}\right)^{2/3}. \tag{22}$$

The skewness of the longitudinal velocity fluctuations has been reported by a number of researchers (e.g., see the review by van Atta and Chen 1970). In general, these researchers have relied on hot-wire anemometry to compute these statistics. A notable exception involves the work of Paquin and Pond (1971), who produced estimates of the Kolmogorov constants using sonic anemometer measurements by invoking Taylor's hypothesis; for example, $r = \overline{U}\Delta t$.

Paquin and Pond (1971) describe in some detail the constraints that restrict the choice of the appropriate spatial separations for determination of the Kolmogorov constants. The two constraints required of all such measurements are that r be much smaller than the scale of the energy-containing eddies and much larger than the Kolmogorov microscale in order to be in the inertial subrange. The first constraint is generally met if we confine our measurements to separation distances that are smaller than our measurement heights, that is, $r/z < 1$. The second constraint is never an issue because $r \gg \eta$, even at our lowest recorded wind speed.

Additionally, the use of a sonic anemometer requires to be much larger than the size of the instrument. This constraint, which arises because of the spatial averaging associated with sonic anemometers (Kaimal et al. 1968; Larsen et al. 1993), requires us to limit our analysis to separation distances much larger than the distance between the sonic transducers, L. While the effect of spatial averaging on $B_{uuu}(r)$ is negligible in the inertial subrange (Stewart 1963; Hill 1996), its effect on $B_{uu}(r)$ can be substantial. Stewart (1963) and Hill (1996) have derived expressions to account for the effect of spatial averaging on second-order statistics. They have shown hat for $r/L \gg 1$,

$$\begin{aligned} B_{uu}(r) &= C_u^2 r^{2/3}\left[1 - \frac{1}{54}\left(\frac{L}{r}\right)^2 - \frac{9}{20}\left(\frac{L}{r}\right)^{2/3}\right] \\ &= C_u^2 r^{2/3} V_{uu}\left(\frac{L}{r}\right), \end{aligned} \tag{23}$$

uch that the structure function requires an additional orrection,

$$C_u^2 = \frac{\overline{[U(t) - U(t + \Delta t)]^2}}{(\overline{U}\Delta t)^{2/3} T_{uu} V_{uu}(L/r)}. \tag{24}$$

Ve note that $\Phi_u(k)$ forms a transform pair with $B_{uu}(r)$ Tatarskii 1971), which results in the relationship given by (20). However, this also means that $\Phi_u(k)$ requires correction for spatial averaging. This correction is obtained from the Fourier transform of (23) iven by

$$\begin{aligned} \Phi_u(k) &= \frac{1}{\pi}\Gamma\left(\frac{5}{3}\right)\sin\left(\frac{\pi}{3}\right)C_u^2 k^{-5/3} - \frac{L^2}{54\pi}\Gamma\left(-\frac{1}{3}\right) \\ &\quad \times \sin\left(-\frac{2\pi}{3}\right)C_u^2 k^{1/3} \\ &\approx 0.25 C_u^2 k^{-5/3}[1 - 0.083(kL)^2], \end{aligned} \tag{25}$$

here the first term is responsible for the constant in 20). The correction term hardly affects our inertial subrange estimates of ϵ over the wavenumber range used our analyses, namely, $kL < 1$.

Finally, interpretation of our measurements is simplified if we confine our investigations to look at the orrelation between signals with zero lags, that is, to riances and covariances that are computed from correlations between variables measured at the same instant in time. The second constraint avoids the complications that arise from spatial displacements caused by the platform that cannot be handled by Taylor's hypothesis (e.g., Lumley and Terray 1983). Nonetheless, it appears that the *FLIP* data are usable to examine the lagged quantities much better than the shipboard measurements owing to its small horizontal and vertical displacements. Therefore, we confine our investigation of the skewness to the *FLIP* dataset.

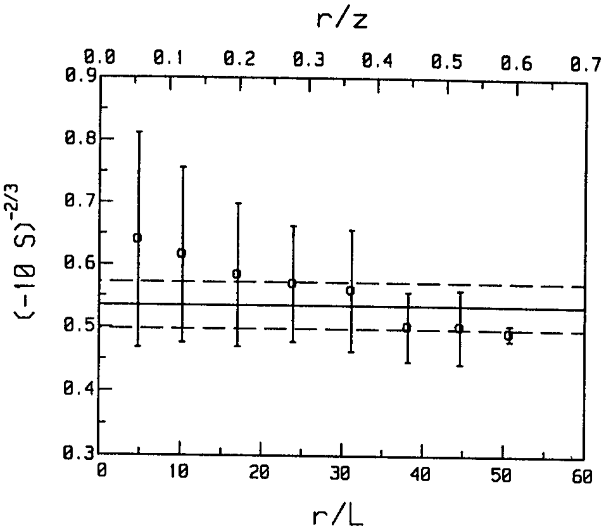

FIG. 4. Estimates of the Kolmogorov constant computed using (22) as a function of the dimensionless length r/z. The lines in the figure denotes a value of 0.53 (solid lines) ± 0.04 (broken lines).

The average of all of the individual *FLIP* measurements of (22) that met the constraints $r/L > 10$ and $r/z < 1$ gives a Kolmogorov constant of 0.57 ± 0.10. Additionally, if we first compute the average skewness using these same constraints and then use the average skewness in (22), we obtain a value of 0.55. These values are in remarkably good agreement with those determined by Paquin and Pond (1971), who derived a value of 0.57 ± 0.10 using individual estimates of (22) and a value of 0.54 using the average skewness.

The dependence of our estimates of the Kolmogorov constant on the constraints given above can be examined by averaging estimates of (22) in bins of r/L. These bin-averaged estimates are shown in Fig. 4 along with the equivalent values of r/z. It is interesting to note that these estimates span the range of estimates reported in the literature and approach a value of 0.50 at large values of r/L. This suggests that the various constraints considered above are responsible for much of the experimental uncertainty. We feel that we can reduce some of the uncertainty in our estimate by using the bin-averaged results. This approach gives more even weight to our estimates over the entire range of r/L. The mean of bin-averaged data between $r/L > 10$ and $r/z < 1$ gives a Kolmogorov constant of 0.53 ± 0.04. Therefore, we use

0.53 in the analysis that follows and recognize that the difference between this value and 0.57 (or 0.49) introduces an uncertainty of approximately 10% in our estimates of the dissipation rate.

5. The TKE budget

The TKE budget equation for stationary and horizontally homogeneous conditions in the surface layer above the wave boundary layer is

$$-\overline{uw}\frac{\partial \overline{U}}{\partial z} - \overline{vw}\frac{\partial \overline{V}}{\partial z} + \frac{g}{\Theta_v}\overline{w\theta_v} - \frac{1}{\rho}\frac{\partial \overline{wp}}{\partial z} - \frac{\partial \overline{we}}{\partial z} - \epsilon = 0, \tag{26}$$

where p denotes pressure fluctuations and e is the turbulent kinetic energy defined as $e = 0.5\,[u^2 + v^2 + w^2]$. The first two terms on the left-hand side of (26) represent the generation of mechanical turbulence through shear, while the third term represents the production (suppression) of turbulence through convection (stratification). The final two terms neither produce nor consume TKE; instead they act to redistribute TKE within the atmospheric boundary layer through pressure and energy transport.

According to MO similarity theory, the various terms in the TKE budget are expected to be universal functions of z/L after normalization by the appropriate scaling parameters, kz/u_*^3,

$$\frac{\epsilon\kappa z}{u_*^3} = \phi_\epsilon(\zeta) = \phi_m(\zeta) - \zeta - \phi_{tp}(\zeta) - \phi_{te}(\zeta), \tag{27}$$

where $\zeta = z/L$, ϕ_ϵ is the dimensionless dissipation function, ϕ_{tp} and ϕ_{te} are the dimensionless transport terms, and the dimensionless shear is defined as

$$\phi_m(\zeta) = \frac{\kappa z}{u_*}\left[\left(\frac{\partial \overline{U}}{\partial z}\right)^2 + \left(\frac{\partial \overline{V}}{\partial z}\right)^2\right]^{1/2}. \tag{28}$$

Equation (28) is consistent with our definition of u_* and the following parameterizations for the momentum flux components:

$$-\overline{uw} = \frac{u_*\kappa z}{\phi_m(\zeta)}\frac{\partial \overline{U}}{\partial z} \tag{29}$$

and

$$-\overline{vw} = \frac{u_*\kappa z}{\phi_m(\zeta)}\frac{\partial \overline{V}}{\partial z}. \tag{30}$$

These parameterizations are common applications of MO similarity theory in first-order closure models. They offer a good example of why we are limiting our analysis to heights above the WBL, since we would not expect these expressions to be valid in a region where the waves, in addition to the stability, can effect the velocity field and thereby modify the wind profiles.

In the sections that follow we determine the form of the dimensionless functions in (27) using our combined datasets. The wide range of stabilities present in this dataset allows us to examine the limiting forms of these functions in both the convective and stable limits. The behavior of the various terms in the TKE budget in these limits are predicted using the approach outlined by Wyngaard (1973).

a. Dimensionless dissipation function

The function that describes the stability dependence of the dimensionless rate of dissipation is a key ingredient in the inertial–dissipation method of estimating air–sea fluxes (Fairall and Larsen 1986). A number of observation studies conducted over the sea (e.g., Large and Pond 1981; Edson et al. 1991) have found that the dissipation of TKE is very nearly in balance with its production, which reduces (27) to

$$\phi_\epsilon(\zeta) \approx \phi_m(\zeta) - \zeta. \tag{31}$$

It is easy to show that this form of the dimensionless dissipation function is consistent with its predicted form in local free convection. In this limit we expect the dissipation rate to be proportional to u_f^3/z. This prediction can be combined with (11) to find its form in the local free-convective limit as

$$\phi_\epsilon(\zeta) = \frac{\epsilon\kappa z}{u_*^3} = \frac{\epsilon\kappa z}{u_f^3}\frac{u_f^3}{u_*^3} = -a\zeta, \qquad \zeta < -1, \tag{32}$$

where a is a constant of proportionality. Since shear production and therefore ϕ_m become negligible in this limit, (31) and (32) are identical if the constant of proportionality is equal to one, which is the expected result if production truly equals dissipation. The value of this constant can be determined from our measurements by setting $\phi_m(\zeta) - \phi_{te}(\zeta) - \phi_{tp}(\zeta) = 0$ in (27), which results in

$$a = \epsilon\left(\frac{g}{\Theta_v}\overline{w\theta_v}\right)^{-1}. \tag{33}$$

The average value of this constant from all estimates of a found for $-\zeta > 1.5$ is 0.99 ± 0.28. Although the scatter is fairly large, this implies that production balances dissipation in the local free-convective limit.

We now compare this result with our measurements of $\phi_\epsilon(\zeta)$ in Fig. 5. In this figure, the solid line is drawn using (31), and the broken line is drawn using $a = 1$ in (32). Since we are not able to compute an estimate of the dimensionless shear with the present dataset, we have opted for consistency and used a function that has the correct form in the convective limit,

$$\phi_m(\zeta) = (1 - 15\zeta)^{-1/3}, \qquad \zeta < 0, \tag{34}$$

as given by Carl et al. (1973) and more recently by Frenzen and Vogel (1992). This function agrees very well with the commonly used Businger–Dyer formulation in forced convection.

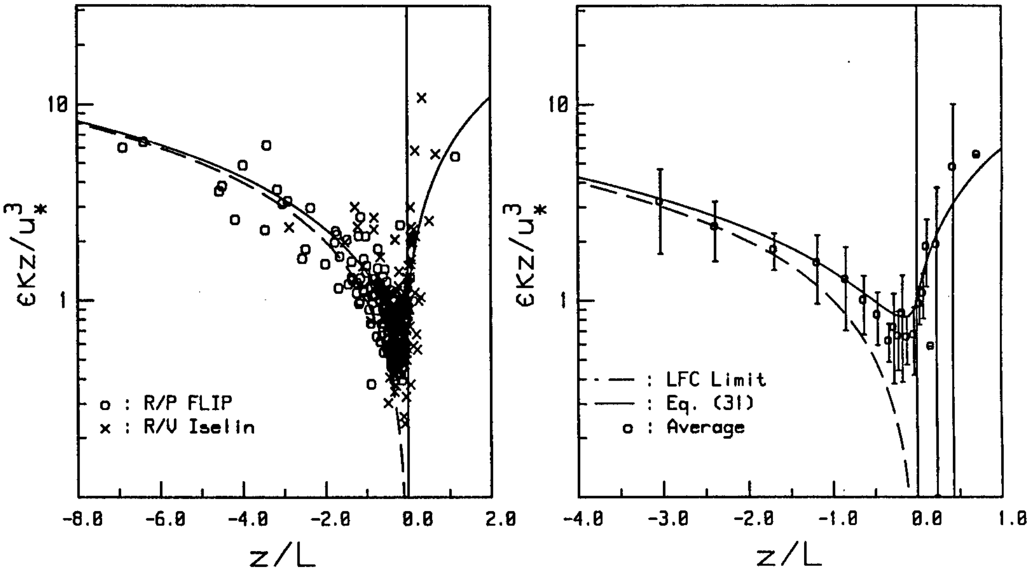

FIG. 5. Estimates of the dimensionless dissipation rate of TKE as a function of *z/L*. The left-hand panel displays the raw data, while the right-hand panel shows the bin-averaged results. The error bars denote the standard error (standard deviation divided by the number of points). The lines drawn in the figure are identified by the equation numbers as given in the text.

As one would expect, the measurements are in excellent agreement with (31) in very unstable conditions since $a \approx 1$. However, it is clear that this simple parameterization is not accurate for slightly unstable and near-neutral conditions where our data indicate that production exceeds dissipation. This finding is consistent with recent measurements reported by Thiermann and Grassl (1992), Vogel and Frenzen (1992), and Frenzen and Vogel (1992), who also found that production exceeds dissipation in the slightly unstable regime. Their dimensionless dissipation functions are shown in Fig. 6.

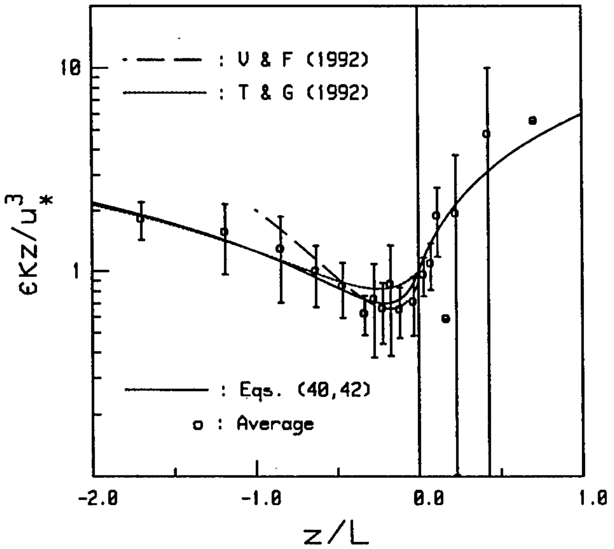

FIG. 6. Functional forms of the dimensionless dissipation functions that include two recently published parameterizations as well as our own functions. The symbols denote bin-averaged results shown in Fig. 5. The solid line drawn in the figure are identified by the equation numbers as given in the text.

The average value of $\phi_\epsilon(\zeta)$ for this dataset is equal to 0.70 over the stability range $-0.1 < \zeta < 0$. This value is in good agreement with the results reported by Garratt (1972), who obtained an average value of $\overline{\phi}_\epsilon = 0.78$ for measurements within the range $-0.1 < \zeta < 0$ using a Kolmogorov constant of 0.50. This value would be reduced to 0.71 using a Kolmogorov constant of 0.53. This slightly unstable estimate is also in agreement with the neutral values of dimensionless dissipation, $\phi_\epsilon(0)$, given by Frenzen and Vogel (1992) and Vogel and Frenzen (1992) in two separate experiments. Their neutral values ranged from 0.84 to 0.89.

b. Dimensionless transport terms

The balance between production and dissipation in free-convective conditions implies that we are using the correct value for the Kolmogorov constant. This assumption further implies that the imbalance at near-neutral conditions is due to the exclusion of the transport terms in our simple parameterization. The direct determination of the energy transport terms in (26) requires flux estimates at multiple levels that are not available in our datasets. However, we can use the wide range of stability in our datasets to our advantage by estimating these terms using the derivative method described in Wyngaard and Coté (1971) and Wilczak et al. (1995). In this method the normalized fluxes are plotted as a

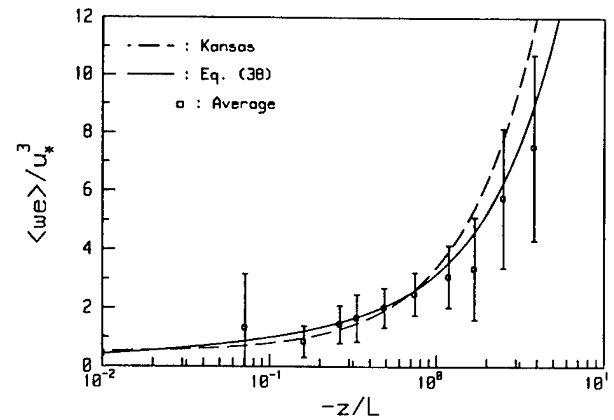

FIG. 7. Estimates of the dimensionless energy flux as a function of z/L. The symbols represent our bin-averaged results. The error bars denote the standard error. The lines drawn in the figure are identified by the equation numbers as given in the text.

function of ζ to determine the dimensionless energy flux function,

$$\phi_e(\zeta) = \frac{\overline{we}}{u_*^3}. \tag{35}$$

This flux should scale with u_f^3 in the convective limit, which leads to the prediction

$$\frac{\overline{we}}{u_*^3} = \frac{\overline{we}}{u_f^3}\frac{u_f^3}{u_*^3} = -\frac{c}{\kappa}, \qquad \zeta < -1, \tag{36}$$

where c is another numerical constant. The derivative of this function is then combined with the definition of the dimensionless energy transport to obtain a prediction for local free convection,

$$\phi_{te}(\zeta) = \frac{\kappa z}{u_*^3}\frac{\partial \overline{we}}{\partial z} = \kappa\zeta\frac{\partial}{\partial\zeta}\left(\frac{\overline{we}}{u_*^3}\right) = -c\zeta, \qquad \zeta < -1, \tag{37}$$

where we see that the constant is only modified by removal of the von Kármán constant.

The dimensionless energy fluxes are plotted in Fig. 7. The broken line in this figure is drawn using the Kansas results reported by Wyngaard and Coté (1971). Wyngaard and Coté (1971) obtained a value of $c \approx 1.0$ using a von Kármán constant of 0.35 such that $c/\kappa \approx 2.9$. Note that we have added an offset of 0.5 to this line [i.e., (37) becomes $-2.9\zeta + 0.5$] and that our definition of the kinetic energy is related to Wyngaard and Coté's as $q = 2e$. Our near-neutral to moderately unstable results are also in good agreement with the data reported by Garratt (1972), Banke and Smith (1973), and Vogel and Frenzen (1992) over a similar stability range.

To include the behavior of this flux over the entire range of unstable conditions we introduce the function given by

$$\phi_e(\zeta) = 2(-\zeta)^{1/3}(1 - \zeta)^{2/3}, \qquad \zeta < 0, \tag{38}$$

as shown by the solid line in Fig. 7. It provides a good fit to the rapid rise exhibited by the data in near-neutral conditions, as well as the tendency toward a smaller slope as $-\zeta$ increases while retaining the correct local free-convective limit. This function is easily differentiated to obtain the dimensionless energy transport function in unstable conditions as

$$\phi_{te}(\zeta) = \frac{\kappa}{3}[4(-\zeta)^{4/3}(1 - \zeta)^{-1/3} + \phi_e(\zeta)], \qquad \zeta < 0. \tag{39}$$

The results from this study and previous investigations show that the turbulent transport of TKE is a nonnegligible term in the budget equation. Therefore, the observed near-balance between production and dissipation in the free-convective limit suggests that the pressure transport term must be nearly equal in magnitude but opposite in sign to the energy transport. This is in agreement with the findings of McBean and Elliot (1975). Under slightly unstable conditions our results indicate that production significantly exceeds dissipation. This suggests that the magnitude of the TKE transport term (a loss of TKE) is greater than the magnitude of the pressure transport term (a gain of TKE).

Although we believe that the observed deficit is a result of a local imbalance in the transport terms, we recognize that the actual mechanisms responsible for the imbalance are debatable. A recent investigation by Edson et al. (1997) using measurements from the 1995 marine boundary layer (MBL) experiment aboard the R/P *FLIP* indicate that this dissipation deficit is a strong function of sea state, implying that MO similarity theory is not valid even well above the surface under high-wind conditions (see section 8). However, although there is some evidence for this effect under the highest wind conditions, the agreement between our data and recent overland results suggests that the measurements are generally above the WBL. Therefore, we believe that we are in a region of the marine surface layer where MO similarity is a valid hypothesis. As such, we recommend the following dimensionless dissipation function for use in ship-based inertial–dissipation systems:

$$\phi_\epsilon(\zeta) = \frac{(1 - \zeta)}{(1 - 7\zeta)} - \zeta, \qquad \zeta < 0. \tag{40}$$

This function represents a slightly modified form of the function given by Thiermann and Grassl (1992), which retains their function's simplicity while providing better agreement with our data, as shown in Fig. 6.

c. Stable regime

As we move away from neutral conditions into the stable regime, the buoyancy force begins to restrict the

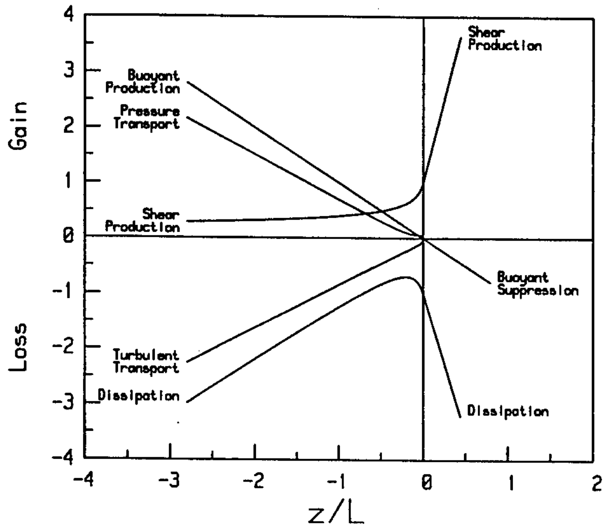

FIG. 8. The dimensionless TKE budget terms proposed in this paper. The buoyant production terms is simply *z/L,* the shear production is given by (34) and (41); the turbulent transport by (39); and the dissipation by (40) and (42). The pressure transport is the residual of these functions.

production TKE through shear by limiting the size of the energy-containing eddies (i.e., their velocity fluctuations). This is a result of the restoring forces that limits the displacement of the parcels from their equilibrium position. In extremely stable conditions, the size of the eddies are completely limited by the stability (Wyngaard 1973) and they become "unaware" of their distance from the surface. The scaling becomes height-independent under these conditions and the MO length becomes the only length scale. As a result, we often refer to such conditions as *z*-less stratification. This also means that u_* is the only velocity scale because we cannot form another from the three remaining governing parameters.

Under these conditions the variance terms in the TKE budget should go asymptotically as ζ (Wyngaard 1973). Our dimensionless energy flux analysis and the Kansas results indicate that the transport terms are truly negligible in stable conditions such that (31) is an appropriate form of the dimensionless dissipation function. Additionally, the limiting form of the dimensionless shear in very stable conditions suggest that it should go as

$$\phi_m(\zeta) = 1 + e\zeta, \qquad \zeta > 0. \tag{41}$$

This results in a form of the dimensionless dissipation function given by

$$\Phi_\epsilon(\zeta) = 1 + (e - 1)\zeta, \qquad \zeta > 0, \tag{42}$$

where a value of $e = 6$ gives good agreement between our data, as shown in Fig. 6. The form of all of the proposed functions in the TKE budget equation is summarized in Fig. 8, where the pressure transport is derived by subtracting (39), (40), and ζ from (34). These functions are in good agreement with the consensus functions presented by Wyngaard (1992).

6. The scalar variance budgets

The scalar equivalents of the TKE budget equation are the potential temperature and specific humidity variance budgets. In homogeneous and steady-state conditions, these budgets are as follows:

$$\overline{w\theta}\frac{\partial\overline{\Theta}}{\partial z} - \frac{1}{2}\frac{\partial\overline{w\theta^2}}{\partial z} - N_\theta = 0, \tag{43}$$

$$\overline{wq}\frac{\partial\overline{Q}}{\partial z} - \frac{1}{2}\frac{\partial\overline{wq^2}}{\partial z} - N_q = 0, \tag{44}$$

where the first terms represents the production of SV, the flux divergence terms again act to redistribute the variance, and N_θ and N_q are one-half the dissipation rate of potential temperature variance and specific humidity variance, respectively. These terms are made dimensionless by dividing these terms by $\kappa z/u_* x_*^2$ where $x = \theta$, q. Rearrangement of the dimensionless expressions results in the SV dissipation functions

$$\phi_{N_\theta}(\zeta) = \frac{N_\theta \kappa z}{u_* T_*^2} = \phi_h(\zeta) - \phi_{t\theta}(\zeta) \tag{45}$$

and

$$\phi_{N_q}(\zeta) = \frac{n_q \kappa z}{u_* q_*^2} = \phi_w(\zeta) - \phi_{tq}(\zeta). \tag{46}$$

The dissipation, production, and transport terms in each of these equations are expected to go as $\zeta^{-1/3}$ in the local free-convective limit (Wyngaard 1973).

The SV dissipation rates are computed using our estimates of the SV spectra in the inertial subrange. In this subrange, the Kolmogorov variance spectrum for temperature and humidity is

$$k\Phi_x(k) = \frac{fS_x(f)}{T_{xx}} = \alpha_x \epsilon^{-1/3} N_x \left(\frac{2\pi f}{\overline{U}}\right)^{-2/3}, \tag{47}$$

where α_x is the Obukhov–Corrsin constant and

$$T_{xx} = 1 - \frac{1}{9}\frac{\sigma_u^2}{(\overline{U})^2} + \frac{1}{3}\frac{(\sigma_v^2 + \sigma_w^2)}{(\overline{U})^2}, \tag{48}$$

as given by Wyngaard and Clifford (1977). The investigations provided by Hill (1989a,b) and Andreas (1987) have shown that the temperature and humidity functions are equal and must share the same value of the Obukhov–Corrsin constant within the constraints of MO similarity theory. In this investigation we have used value of $\alpha_x = 0.80$ reported by Wyngaard and Coté (1971), Paquin and Pond (1971), Champagne et al. (1977), and Högström (1996).

Our plots of the dimensionless scalar dissipation functions are shown in Fig. 9. The dotted line drawn in the

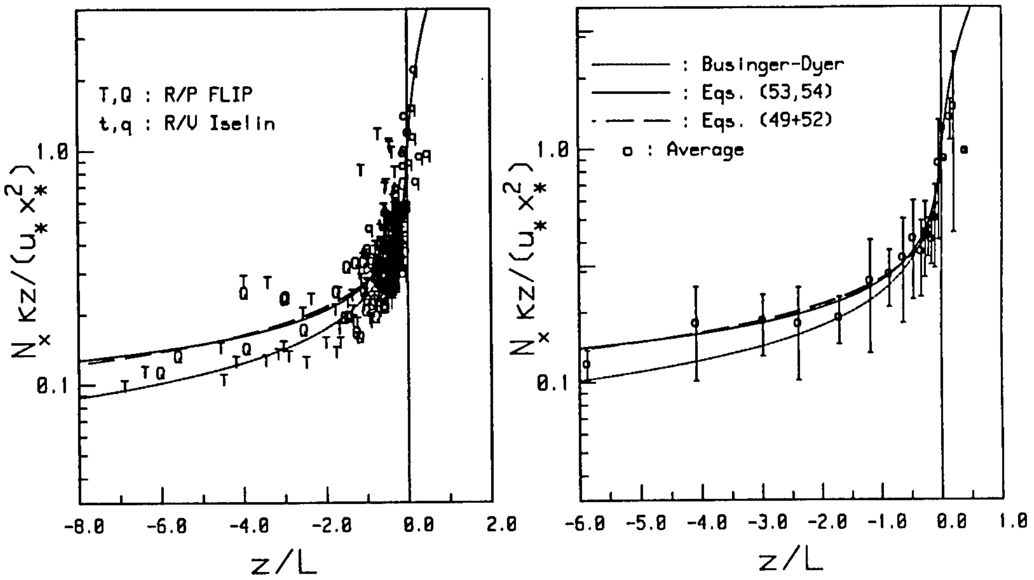

FIG. 9. Estimates of one-half the dimensionless dissipation rate of temperature variance, N_θ, and specific humidity variance, N_q, as a function of z/L. The left-hand panel displays the raw data, while the right-hand panel shows the the bin-averaged results. The error bars denote the standard error. The dotted line represents the Businger–Dyer formulation of the dimensionless scalar gradient function given by (49). The other lines drawn in the figure are identified by the equation numbers as given in the text.

figure represents the Businger–Dyer formulation for the dimensionless scalar profiles,

$$\phi_y(\zeta) = (1 - 16\zeta)^{-1/2}, \qquad \zeta < 0, \tag{49}$$

where $y = h, w$. Although the exponent used in this function does not agree with our prediction in the convective limit, a number of field experiments (Businger et al. 1971; Dyer 1974; Dyer and Bradley 1982) have shown that it provides a better fit to the data in near-neutral conditions than a function with a $(-\zeta)^{-1/3}$ dependency. Our data also exhibit good agreement with this function in near-neutral conditions. However, the agreement between our averaged data and the Businger–Dyer formulation clearly worsens as the conditions become more convective. This suggests that the transport terms are no longer negligible in convective conditions.

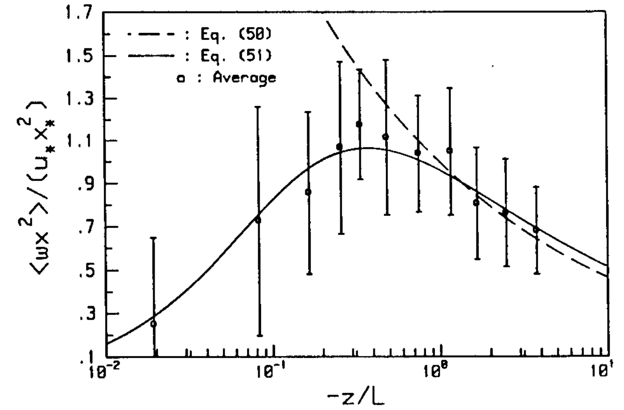

FIG. 10. Estimates of the dimensionless temperature variance flux, $\overline{w\theta^2}$, and specific humidity variance flux, $\overline{wq^2}$, as a function of z/L. The symbols denote our bin-averaged results. The error bars denote the standard error. The lines drawn in the figure are identified by the equation numbers as given in the text.

We can infer something about the dimensionless form of the transport terms by using our SV flux estimates with the derivative approach explained above. In the local free convective limit we have

$$\phi_x(\zeta) = \frac{\overline{wx^2}}{u_* x_*^2} = \frac{\overline{wx^2}}{u_f x_f^2}\frac{u_f x_f^2}{u_* x_*^2} = B(-\zeta)^{-1/3}, \qquad \zeta < -1, \tag{50}$$

where the numerical constant includes the vón Kármán constant as $B = b\kappa^{1/3}$. The plot of this function is shown in Fig. 10, where the broken line in this figure is our convective limit prediction. The constant that gives the best agreement between our data and the prediction is given by $B = 1$. The averaged data in this figure follow the free-convective prediction to about $-\zeta = 0.5$ and then abruptly returns to the origin. This behavior is consistent with the results reported by Wyngaard and Coté (1971). We can parameterize this behavior with a fairly simple function shown by the solid line in this figure, which is given by

$$\phi_x(\zeta) = -18\zeta(1 - 8\zeta)^{-4/3}, \qquad \zeta < 0. \tag{51}$$

This function provides good agreement with the data in unstable conditions and has the proper form in the free-convective limit. The function is easily differentiated to

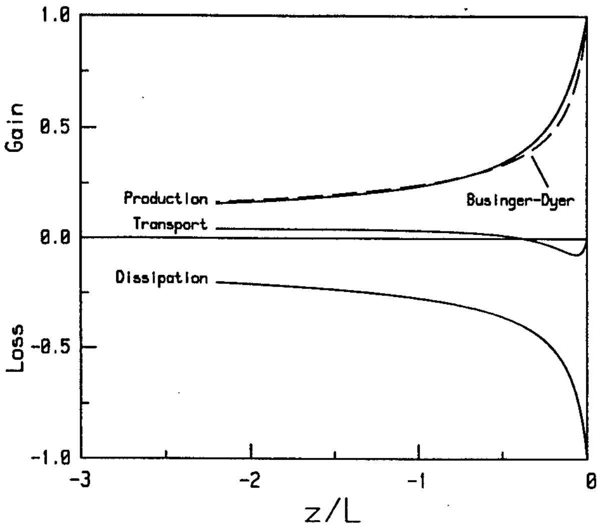

FIG. 11. The dimensionless scalar variance budget terms proposed in this paper. The turbulent transport is given by (52) and the dissipation by (53). The production term is the sum of these two functions. The broken line is the Businger–Dyer formulation for the production term.

obtain a form of the dimensionless transport function given by

$$\phi_{tx}(\zeta) = -\frac{\kappa}{6}[(24\zeta)^2(1-8\zeta)^{-7/3} - 3\phi_x(\zeta)], \qquad \zeta < 0. \tag{52}$$

The behavior of this transport term is consistent with the observations of Deardorff (1966) and Wyngaard and Coté (1971). It represents a loss of SV in near-neutral conditions and a slight gain in very unstable conditions, as shown in Fig. 11.

The dimensionless dissipation function can then be parameterized by inserting (49) and (52) in (45) and (46). The sum of these two functions agrees very well with our averaged data, as shown by the broken line in Fig. 9. Unfortunately, besides being rather cumbersome, this function does not strictly have the proper convective form. However, we can use the good agreement between the Businger–Dyer formulation and our near-neutral data to determine an estimate of the dimensionless SV dissipation function that has the correct convective limit form and is in good agreement with the measurements over the entire range of data. This function is represented by the solid line in Fig. 9 and is given by

$$\phi_{N_x}(\zeta) = (1-\zeta)^{1/6}(1-16\zeta)^{-1/2}, \qquad \zeta < 0. \tag{53}$$

The production curve in Fig. 11 represents the sum of (52) and (53).

Finally, our results have shown no clear trend in the dimensionless SV fluxes under stable conditions. This suggests that the derivative of this function (and therefore the turbulent transport) is negligible under these conditions, such that production equals dissipation. Although we have a limited amount of data in stable conditions, we obtain good agreement using the same constant that we have used for the dimensionless shear such that

$$\phi_{N_x}(\zeta) = \phi_h(\zeta) = 1 + 6\zeta, \qquad \zeta > 0. \tag{54}$$

This is consistent with the findings that the dimensionless shear and profile functions are identical under stable conditions (e.g., Panofsky and Dutton 1984).

7. The structure functions

The method used above to compute the dissipation rates of temperature and humidity variance requires us to combine TKE dissipation rates (computed from our velocity spectra) with our scalar spectra. This approach can become problematic when the instruments used to measure the velocity and scalar quantities are not collocated. Additionally, because we used inertial subrange techniques to determine the dissipation rates, our results on the TKE and SV budgets depend on the choice of Kolmogorov constants.

An approach that can be used to avoid these problems is to use the structure function parameter to investigate some of the characteristics of the turbulence. The dimensionless structure function parameters are known to obey MO similarity theory (Wyngaard et al. 1971b; Wyngaard et al. 1978; Friehe et al. 1975; Fairall et al. 1980; Edson et al. 1991). In fact, the relationship between the structure function parameters and the dissipation rates given by

$$C_x^2 = 4.0\alpha_x\epsilon^{-1/3}N_x \tag{55}$$

results in a form of the dimensionless structure function parameter given as

$$\frac{C_x^2 z^{2/3}}{x_*^2} = f_x(\zeta) = 4.0\alpha_x\kappa^{-2/3}\phi_{N_x}(\zeta)\phi_\epsilon(\zeta)^{-1/3}, \tag{56}$$

where x is now equal to u, θ, and q. Using the Kolmogorov and von Kármán constants used in this investigation and (40) and (42) for the dimensionless dissipation function, the dimensionless velocity structure function parameter becomes

$$f_u(\zeta) = 3.9\left[\frac{(1-\zeta)}{(1-7\zeta)} - \zeta\right]^{2/3}, \qquad \zeta < 0 \tag{57}$$

and

$$f_u(\zeta) = 3.9(1+5\zeta)^{2/3}, \qquad \zeta \geq 0. \tag{58}$$

The agreement between this function and our data is very similar to that shown in Fig. 6.

Our dimensionless scalar structure function parameter estimates are shown in Fig. 12. In this figure, the solid line is drawn using (56) with Eqs. (53) and (54) for $\phi_{N_x}(\zeta)$ and (40) and (42) for $\phi_\epsilon(\zeta)$. Alternatively, the limiting forms of the dimensionless dissipation functions predict that this function should be proportional

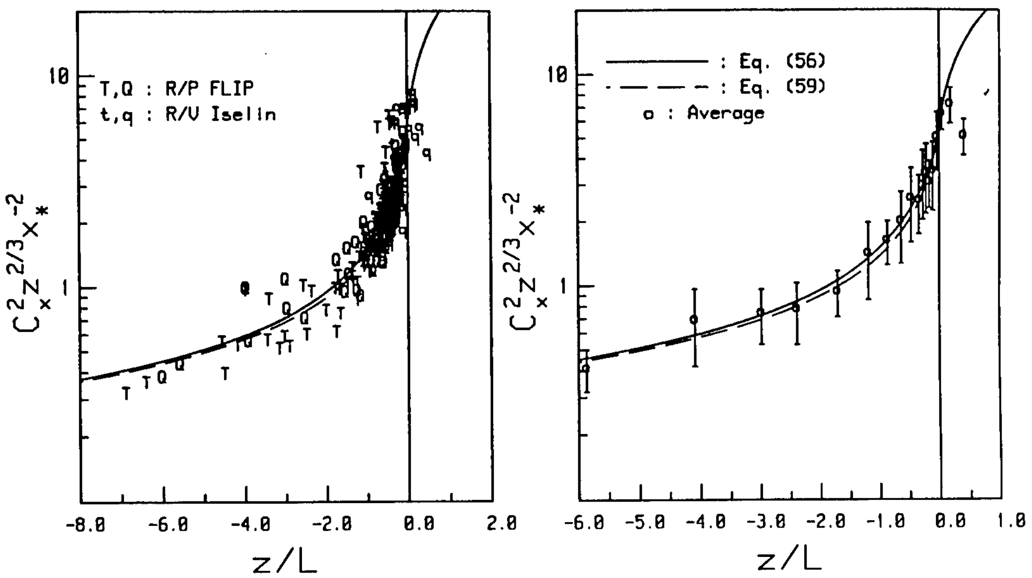

FIG. 12. Estimates of the dimensionless structure function parameter for temperature, C_θ^2, and specific humidity, C_q^2, as a function of z/L. The left-hand panel displays the raw data, while the right-hand panel shows the the bin-averaged results. The error bars denote the standard error. The lines drawn in the figure are identified by the equation numbers as given in the text.

to $-\zeta^{-2/3}$ in the convective limit. Therefore, another common approach is to use the limiting forms to simplify (56) to read

$$f_{\theta,q}(\zeta) = E(1 - F\zeta)^{-2/3}, \qquad \zeta < 0 \qquad (59)$$

in convective conditions, where E and F are another set of numerical constants. The neutral value of the dimensionless structure function parameter that agrees with both our data and our choice of the Kolmogorov and von Kármán constants is $E = 5.9$, while a value of $F = 8$ provides a good fit to our data, as shown by the broken line in Fig. 12. Our results are in close agreement with the original Kansas data (Wyngaard et al. 1971b). The closeness of these two experimental results taken more than 25 years apart with different instruments over both land and ocean is a tribute to the universality of MO similarity theory.

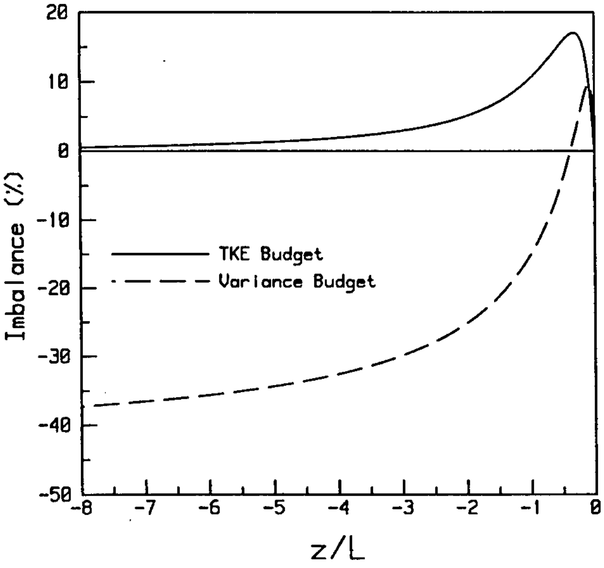

FIG. 13. The percent difference between the production and dissipation of TKE (solid line) and scalar variance (broken line) as a function of z/L. Positive values are a result of production exceeding dissipation, while negative values are a result of dissipation exceeding production.

8. Discussion

Although there is some uncertainty depending on the particular form of the dimensionless shear term, our study found that the TKE budget is well described by a balance between production and dissipation except for slightly unstable conditions where production exceeds dissipation by as much as 17% (see Fig. 13). We have argued that this is due to a local imbalance between the pressure and energy transport. Additionally, we have argued that the good agreement between our results and the overland results of Vogel and Frenzen (1992) and Frenzen and Vogel (1992) suggest that our measurements are generally taken above the WBL.

However, because the mechanisms responsible for this imbalance are still under active investigation, we recognize that part of the imbalance observed in our measurements, particularly under high wind conditions, may be due to mechanisms that do not obey MO similarity theory. For example, there have been a number of studies (e.g., Högström 1990; Wilczak et al. 1995) that have found that TKE dissipation exceeds production in near-neutral conditions. Högström (1990) concluded hat the excess of local dissipation over local production vas a result of inactive turbulence (Bradshaw 1967). Ie argued that inactive turbulence is imported to the urface layer from the upper boundary layer through ressure transport. This extra energy is then dissipated n the surface layer, thereby creating an excess of local issipation.

In the marine surface layer there is another plausible xplanation to explain the findings of this paper, that is, nat production exceeds dissipation. Over developing urface waves, part of the energy flux entering the surace layer is not dissipated into thermal energy but rather s transported to the surface to generate and sustain vaves and currents. This energy flux is expected to reult in a "dissipation deficit" in the volume-averaged issipation rate that would result in local production xceeding dissipation. It should be noted that such a ituation is not limited to the ocean; for example, a imilar situation might exist over a forest canopy.

Over the ocean this deficit is expected to be a function f sea state and, as such, is not expected to obey traitional MO similarity theory. As mentioned above, preminary results from ONR's MBL program presented y Edson et al. (1997) provides evidence for this sea tate–dependent dissipation deficit. This mechanism is lso consistent with the findings of Yelland and Taylor 1996), who derived an imbalance term that was a funcon of both stability and wind speed. Yelland and Taylor 1996) found that local production generally exceeded issipation and that the imbalance increased with inreasing wind speed.

The good agreement between our derived energy ansport term and previous parameterizations sugests that some fraction of our observed dissipation eficit may be due to an additional pressure transport rm that is sea state dependent. This proposition ems reasonable since the pressure flux evaluated at ie surface, $\overline{wp}_0$, represents the energy flux into the aves. It might also explain differences between reılts taken from the open ocean (e.g., Yelland and aylor 1996) versus coastal studies (e.g., Edson et al. 991; Wilczak et al. 1997) due to differences in sea ate at a given wind speed. For example, we expect ie coastal wave field to saturate at some point due the influence of the bottom. This would result in ss energy going into the wave field as well as a ugher surface compared to the open ocean for a ven wind speed. It could also explain differences etween results taken from ship-based versus buoy stems due to their relative proximity to the surface.

We are now investigating these and other hypotheses ing the data taken during the MBL program (e.g., iller et al. 1997). This program is providing extensive easurements of the coupled boundary layers and wave ld that allow us to compute all the terms in the KE idget. This is providing investigators with information out the sea state and has allowed us to isolate the ave-induced pressure and velocity fluctuations in the wave boundary layer (Wetzel 1996; Hare et al. 1997; Hristov et al. 1997). The main objective of this program is to improve the parameterizations provided here and to provide us with a means to extend similarity theory into the WBL.

9. Conclusions

In this paper we have examined several aspects of MO similarity theory in the surface layer over the ocean, including the various terms of the TKE budget and the SV budget equations, the Kolmogorov constant, and the dimensionless structure function parameters. These functions all have the appropriate behavior in the convective limit. In estimating these functions we opted for simple parameterizations, which seemed more appropriate because we were inferring a number of these terms through the derivative approach.

The form of the various terms in the TKE budget presented in this study closely resembled those derived from several recent overland experiments. Likewise, the form of the dimensionless SV dissipation functions and structure function parameters are in close agreement with the Kansas formulations given by Wyngaard and Coté (1971) and Wyngaard et al. (1971b). Although our measurements may be slightly influenced by wave-induced effects under high wind conditions, the good agreement between our results and previously published functions implies that MO similarity theory is valid in the marine surface layer above the WBL.

Our results agree with the theoretical requirement that the same functions be used for temperature and humidity. The parameterization for the SV transport terms were obtained using our measurements of the SV flux with the derivative approach. Our results have shown that transport terms are a slight loss of SV in near-neutral conditions and a source of SV in convective conditions, which again agrees with the Kansas observations. Our results indicate that the production of SV exceeds its dissipation by 9% in near-neutral conditions and that dissipation exceeds production by up to 13% in convective conditions as shown in Fig. 13.

In their review of the inertial–dissipation method, Fairall and Larsen (1986) noted uncertainties in the dimensionless function, the TKE, and variance budget balances, and doubts about the similarity of the temperature and moisture functions. These new results show that temperature and moisture are similar, to the accuracy of our measurements, and the uncertainties have been significantly reduced. The dimensionless structure function parameters and dissipation functions presented here are essentially complete and can be used for up-to-date applications in the inertial–dissipation flux estimation method as long as the measurements are taken above the WBL. The dimensionless structure function parameters given by (57) through (59) can be used in these algorithms without assumptions about the Kolmogorov constants, the dimensionless gradients, or the transport functions.

Acknowledgments. This work was supported by the ONR's Remote Sensing (Grants N00014-92-J-1585 and N00014-96-1-0516) and Marine Boundary Layers (Grant N00014-93-1-0274) Programs. Support was also received from the NOAA Climate and Global Change Program and the Department of Defense Advanced Sensor Applications Program. The authors wish to thank George Young of the Pennsylvania State University and Jeffrey Hare of NOAA/ETL for their help in collecting the data and the crews of the R/V *Iselin* and the R/P *FLIP* for their outstanding efforts. We would also like to thank Reginald Hill of NOAA/ETL for his thoughtful review of this article.

REFERENCES

Anctil, F., M. A. Donelan, W. M. Drennan, and H. C. Graber, 1994: Eddy-correlation measurements of air-sea fluxes from a discus buoy. *J. Atmos. Oceanic Technol.*, **11**, 1144–1150.

Anderson, R. J., 1993: A study of wind stress and heat flux over the open ocean by the inertial-dissipation method. *J. Phys. Oceanogr.*, **23**, 2153–2161.

Andreas, E. L, 1987: On the Kolmogorov constants for the temperature–humidity cospectrum and the refractive index spectrum. *J. Atmos. Sci.*, **44**, 2399–2406.

——, 1994: Reply to "Comment on 'Sea spray and the turbulent air–sea heat fluxes' by E. L Andreas" by K. B. Katsaros and G. de Leeuw. *J. Geophys. Res.*, **99**, 14 345–14 350.

——, J. B. Edson, E. C. Monahan, M. P. Rouault, and S. D. Smith, 1995: The spray contribution to net evaporation from the sea. *Bound.-Layer Meteor.*, **72**, 3–52.

Banke, E. G., and S. D. Smith, 1973: Wind stress on arctic sea ice. *J. Geophys. Res.*, **78**, 7871–7883.

Bradley, E. F., P. A. Coppin, and J. S. Godfrey, 1991: Measurements of sensible and latent heat flux in the western equatorial Pacific Ocean. *J. Geophys. Res.*, **96**, 3375–3389.

Bradshaw, P., 1967: Inactive motion and pressure fluctuations in the turbulent boundary layer. *J. Fluid Mech.*, **30**, 241–258.

Businger, J. A., J. C. Wyngaard, and Y. Izumi, 1971: Flux profile relationships in the atmospheric surface layer. *J. Atmos. Sci.*, **28**, 181–189.

Carl, D. M., T. C. Tarbell, and H. A. Panofsky, 1973: Profiles of wind and temperature from towers over homogeneous terrain. *J. Atmos. Sci.*, **30**, 788–794.

Champagne, F. H., C. A. Friehe, J. C. LaRue, and J. C. Wyngaard, 1977: Flux measurements, flux estimation techniques, and fine scale turbulence measurements in the unstable surface layer over land. *J. Atmos. Sci.*, **34**, 515–530.

Deardorff, J. W., 1966: The counter-gradient heat flux in the lower atmosphere and in the laboratory. *J. Atmos. Sci.*, **23**, 503–506.

——, 1970: Convective velocity and temperature scales for the unstable planetary boundary layer and for Rayleigh convection. *J. Atmos. Sci.*, **27**, 1211–1213.

DeCosmo, J., K. B. Katsaros, S. D. Smith, R. J. Anderson, W. A. Oost, K. Bumke, and A. L. M. Grant, 1996: Air-sea exchange of sensible heat and water vapor over whitecap sea states. *J. Geophys. Res.*, **101**, 12 001–12 016.

Donelan, M. A., F. W. Dobson, S. D. Smith, and R. J. Anderson, 1993: On the dependence of sea surface roughness on wave development. *J. Phys. Oceanogr.*, **23**, 2143–2149.

Dyer, A. J., 1974: A review of flux profile relationships. *Bound.-Layer Meteor.*, **7**, 363–372.

——, and B. B. Hicks, 1970: Flux-gradient relationships in the constant flux layer. *Quart. J. Roy. Meteor. Soc.*, **96**, 715–721.

——, and E. F. Bradley, 1982: An alternative analysis of the flux-gradient relationships at the 1976 ITCE. *Bound.-Layer Meteor.*, **22**, 3–19.

——, and B. B. Hicks, 1982: Kolmogoroff constants at the 1976 ITCE. *Bound.-Layer Meteor.*, **22**, 137–150.

Edson, J. B., C. W. Fairall, S. E. Larsen, and P. G. Mestayer, 1991: A study of the inertial-dissipation technique for computing air–sea fluxes. *J. Geophys. Res.*, **96**, 10 689–10 711.

——, S. Wetzel, C. Friehe, S. Miller, and T. Hristov, 1997: Energy flux and dissipation profiles in the marine surface layer. *Proc. 12th Symp. on Boundary Layers and Turbulence*, Vancouver, BC, Canada, Amer. Meteor. Soc., 314–315.

——, A. A. Hinton, K. E. Prada, J. E. Hare, and C. W. Fairall, 1998: Direct covariance flux estimates from mobile platforms at sea. *J. Atmos. Oceanic Technol.*, **15**, 547–562.

Fairall, C. W., and S. E. Larsen, 1986: Inertial dissipation methods and turbulent fluxes at the air ocean interface. *Bound.-Layer Meteor.*, **34**, 287–301.

——, G. E. Schacher, K. L. Davidson, and T. M. Houlihan, 1980: Measurements of the humidity structure function parameters C_q^2 and C_{tq} over the ocean. *Bound.-Layer Meteor.*, **19**, 81–92.

——, E. F. Bradley, D. P. Rogers, J. B. Edson, and G. S. Young, 1996a: Bulk parameterization of air–sea fluxes for TOGA COARE. *J. Geophys. Res.*, **101**, 3747–3764.

——, ——, J. S. Godfrey, G. A. Wick, J. B. Edson, and G. S. Young, 1996b: Cool-skin and warm-layer effects on sea surface temperature. *J. Geophys. Res.*, **101**, 1295–1308.

——, A. B. White, J. B. Edson, and J. E. Hare, 1997: Integrated shipboard measurements of the marine boundary layer. *J. Atmos. Oceanic Technol.*, **14**, 338–359.

Frederickson, P., K. L. Davidson, and J. B. Edson, 1997: A study of wind stress determination methods from a ship and an offshore tower. *J. Atmos. Oceanic Technol.*, **14**, 822–834.

Frenzen, P., and C. A. Vogel, 1992: The kinetic energy budget in the surface layer: A review and an experimental reexamination in the field. *Bound.-Layer Meteor.*, **60**, 49–76.

Friehe, C. A., J. C. LaRue, F. H. Champagne, C. H. Gibson, and G. F. Dreyer, 1975: Effect of temperature and humidity fluctuations on the optical refractive index in the marine boundary layer. *J. Opt. Soc. Amer.*, **65**, 1502–1511.

Fujitani, T., 1981: Direct measurement of turbulent fluxes over the sea during AMTEX. *Pap. Meteor. Geophys.*, **32**, 119–134.

——, 1985: Method of turbulent flux measurement on a ship by using a stable platform system. *Pap. Meteor. Geophys.*, **36**, 157–170.

Garratt, J. R., 1972: Studies of turbulence in the surface layer over water (Lough Neagh). Part II: Production and dissipation of velocity and temperature fluctuations. *Quart. J. Roy. Meteor. Soc.*, **98**, 642–657.

Geernaert, G. L., K. B. Katsaros, and K. Richter, 1986: Variation of the drag coefficient and its dependence on sea state. *J. Geophys. Res.*, **91**, 4762–4779.

Godfrey, J. S., and A. C. M. Beljaars, 1991: On the turbulent fluxes of buoyancy, heat, and moisture at the air–sea interface at low wind speeds. *J. Geophys. Res.*, **96**, 22 043–22 048.

Hare, J. E., T. Hara, J. B. Edson, and J. Wilczak, 1997: A similarity analysis of the structure of air flow over surface waves, *J. Phys. Oceanogr.*, **27**, 1018–1037.

Hill, R. J., 1989a: Implication of Monin–Obukhov similarity theory for scalar quantities. *J. Atmos. Sci.*, **46**, 2236–2244.

——, 1989b: Structure functions and spectra of scalar quantities in the inertial-convective and viscous-convective ranges of turbulence. *J. Atmos. Sci.*, **46**, 2245–2251.

——, 1996: Corrections to Taylor's frozen turbulence approximation. *Atmos. Res.*, **40**, 153–175.

Högström, U., 1990: Analysis of turbulence structure in the surface layer with a modified similarity formulation for near neutral conditions. *J. Atmos. Sci*, **47**, 1949–1972.

——, 1996: Review of some basic characteristics of the atmospheric surface layer. *Bound.-Layer Meteor.*, **78,** 215–246.

Højstrup, J., 1982: Velocity spectral in the unstable planetary boundary layer. *J. Atmos. Sci.*, **39,** 2239–2248.

Hristov, T., C. Friehe, S. Miller, J. Edson, and S. Wetzel, 1997: Structure of the atmospheric surface layer over the ocean waves—Phase averaging via the Hilbert transform. *Proc. 12th Symp. on Boundary Layers and Turbulence,* Vancouver, BC, Canada, Amer. Meteor. Soc., 283–284.

Izumi, Y., 1971: Kansas 1968 field program data report. Air Force Cambridge Res. Lab. AFCRL-72-0041, Environ. Res. Paper No. 379, Hanscom AFB, MA, 79 pp. [NTIS AD 739165.]

Kaimal, J. C., J. C. Wyngaard, and D. A. Haugen, 1968: Deriving power spectra from sonic anemometers. *J. Appl. Meteor.*, **7,** 827–837.

——, ——, Y. Izumi, and O. R. Cote, 1972: Spectral characteristics of surface layer turbulence. *Quart. J. Roy. Meteor. Soc.*, **98,** 563–589.

Katsaros, K. B., and G. de Leeuw, 1994: Comment on "Sea spray and the turbulent air-sea heat fluxes" by E. L Andreas. *J. Geophys. Res.*, **97,** 14 339–14 343.

——, S. D. Smith, and W. A. Oost, 1987: HEXOS—Humidity Exchange Over the Sea: A program for research on water vapor and droplet fluxes from sea to air at moderate and high wind speeds. *Bull. Amer. Meteor. Soc.*, **68,** 466–476.

——, and Coauthors, 1994: Measurements of humidity and temperature in the marine environment during the HEXOS main experiment. *J. Atmos. Oceanic Technol.*, **11,** 964–981.

Keuttner, J. P., and J. Holland, 1969: The BOMEX project. *Bull. Amer. Meteor. Soc.*, **50,** 394–402.

Kolmogorov, A. N., 1941: Dissipation of energy in the locally isotropic turbulence. *Dokl. Akad. Nauk SSSR,* **32,** 16–18.

Kropfli, R. A., and S. F. Clifford, 1994: The San Clemente Ocean Probing Experiment: A study of air–sea interactions with remote and in-situ sensors. *IGARSS '94,* Pasadena, CA, IEEE, 2407–2409.

Large, W. G., and S. Pond, 1981: Open ocean momentum flux measurements in moderate to strong winds. *J. Phys. Oceanogr.*, **11,** 324–336.

——, and ——, 1982: Sensible and latent heat flux measurements over the ocean. *J. Phys. Oceanogr.*, **12,** 464–482.

Larsen, S. E., J. B. Edson, C. W. Fairall, and P. G. Mestayer, 1993: Measurement of temperature spectra by a sonic anemometer. *J. Atmos. Oceanic Technol.*, **10,** 345–354.

Liu, W. T., K. B. Katsaros, and J. A. Businger, 1979: Bulk parameterization of the air–sea exchange of heat and water vapor including the molecular constraints at the interface. *J. Atmos. Sci.*, **36,** 1722–1735.

Lumley, J. L., and H. A. Panofsky, 1964: *The Structure of Atmospheric Turbulence.* J. Wiley and Sons, 229 pp.

——, and E. A. Terray, 1983: Kinematics of turbulence convected by a random wave field. *J. Phys. Oceanogr.*, **13,** 2000–2007.

Maat, N., C. Kraan, and W. A. Oost, 1991: The roughness of wind waves. *Bound.-Layer Meteor.*, **54,** 89–103.

McBean, G. A., and J. A. Elliott, 1975: The vertical transport of kinetic energy by turbulence and pressure in the boundary layer. *J. Atmos. Sci.*, **32,** 753–766.

Miller, S., C. Friehe, T. Hristov, and J. Edson, 1997: Wind and turbulence profiles in the surface over the ocean. *Proc. 12th Symp. on Boundary Layers and Turbulence,* Vancouver, BC, Canada, Amer. Meteor. Soc., 308–309.

Monin, A. S., and A. M. Obukhov, 1954: Basic laws of turbulent mixing in the surface layer of the atmosphere. *Trudy Geofiz. Inst. Aca. Nauk SSSR,* **24,** 163–187.

Obukhov, A. M., 1946: Turbulence in an atmosphere with non-uniform temperature. *Trudy Inst. Teoret. Geofiz. Nauk SSSR,* **1,** 95–115 (translation in *Bound.-Layer Meteorol.*, **2,** 7–29, 1971).

Oost, W. A., C. W. Fairall, J. B. Edson, S. D. Smith, R. J. Anderson, J. A. B. Wills, K. B. Katsaros, and J. DeCosmo, 1994: Flow distortion calculations and their application in HEXMAX. *J. Atmos. Oceanic Technol.*, **11,** 366–386.

Panofsky, H. A., and J. A. Dutton, 1984: *Atmospheric Turbulence.* J. Wiley and Sons, 397 pp.

Paquin, J. E., and S. Pond, 1971: The determination of the Kolmogorov constants for velocity, temperature and humidity fluctuations and some second- and third-order structure functions. *J. Fluid Mech.*, **50,** 257–269.

Rieder, K. F., J. A. Smith, and R. A. Weller, 1994: Observed directional characteristics of the wind, wind stress, and surface waves on the open ocean. *J. Geophys. Res.*, **99,** 22 589–22 596.

Schmitt, K. F., C. A. Friehe, and C. H. Gibson, 1978: Humidity sensitivity of atmospheric temperature sensors by salt contamination. *J. Phys. Oceanogr.*, **8,** 141–161.

——, ——, and ——, 1979: Structure of marine surface layer turbulence. *J. Atmos. Sci.*, **36,** 602–618.

Skupniewicz, C. E., and K. L. Davidson, 1991: Hot-film measurements from a small buoy: Surface wind stress measurements using the inertial dissipation method. *J. Atmos. Oceanic Technol.*, **8,** 309–321.

Smith, S. D., 1988: Coefficients for sea surface wind stress, heat flux, and wind profiles as a function of wind speed and temperature. *J. Geophys. Res.*, **93,** 15 467–15 472.

——, and Coauthors, 1992: Sea surface wind stress and drag coefficients: The HEXOS results. *Bound.-Layer Meteor.*, **60,** 109–142.

——, C. W. Fairall, G. L. Geernaert, and L. Hasse, 1996: Air–sea fluxes: 25 years of progress. *Bound.-Layer Meteor.*, **78,** 247–290.

Stewart, R. W., 1963: Reconciliation of the available experimental data concerning the spectrum and asymmetry of locally isotropic turbulence. *Dokl. Akad. Nauk SSSR,* **152,** 324–326.

Tatarskii, V. I., 1971: *The Effects of the Turbulent Atmosphere on Wave Propagation.* Keter Press, 471 pp.

Tennekes, H., 1970: Free convection in the turbulent Ekman layer of the atmosphere. *Phys. Fluids,* **11,** 669–671.

Thiermann, V., and H. Grassl, 1992: The measurement of turbulent surface layer fluxes by use of bichromatic scintillation. *Bound.-Layer Meteor.*, **58,** 367–389.

Tsukomoto, O., E. Ohtaki, H. Ishida, M. Horiguchi, and Y. Mitsuta, 1990: On-board direct measurements of turbulent fluxes over the open sea. *J. Meteor. Soc. Japan,* **68,** 203–211.

van Atta, C. W., and W. Y. Chen, 1970: Structure functions of turbulence in the atmospheric boundary layer over the ocean. *J. Fluid Mech.*, **44,** 145–159.

Vogel, C. A., and P. Frenzen, 1992: A new study of the TKE budget in the surface layer. Part II: The dimensionless function and divergent transport terms. *Proc. 10th Symp. on Turbulence and Diffusion,* Portland, OR, Amer. Meteor. Soc., 161–164.

Webster, P. J., and R. Lukas, 1992: TOGA COARE: The coupled ocean–atmosphere response experiment. *Bull. Amer. Meteor. Soc.*, **73,** 1377–1416.

Wetzel, S. W., 1996: An investigation of wave-induced momentum flux through phase averaging of open ocean wind and wave fields. M.S. thesis, Department of Civil Engineering, Massachusetts Institute of Technology, 93 pp.

Wilczak, J., A. J. Bedard, J. Edson, J. Hare, J. Højstrup, and L. Mahrt, 1995: Pressure transport measured from a sea mast during the RASEX program. *Proc. 11th Symp. on Boundary Layers and Turbulence,* Charlotte, NC, Amer. Meteor. Soc., 489–492.

——, J. Edson, T. Hara, J. Højstrup, and J. Hare, 1997: The turbulent kinetic energy budget during RASEX. *Proc. 12th Symp. on Boundary Layers and Turbulence,* Vancouver, BC, Amer. Meteor. Soc., 312–313.

Wyngaard, J. C., 1973: On surface layer turbulence. *Workshop on Micrometeorology,* D. A. Haugen, Ed., Amer. Meteor. Soc., 101–149.

——, 1992: Atmospheric turbulence. *Annu. Rev. Fluid Mech.*, **24,** 205–233.

——, and O. R. Coté, 1971: The budgets of turbulent kinetic energy and temperature variance in the atmospheric surface layer. *J. Atmos. Sci.,* **28,** 190–201.

——, and S. F. Clifford, 1977: Taylor's hypothesis and high frequency turbulence spectra. *J. Atmos. Sci.,* **34,** 922–929.

——, and M. A. Lemone, 1980: Behavior of the refractive index structure function in the entraining convective boundary layer. *J. Atmos. Sci.,* **37,** 1573–1585.

——, O. R. Coté, and Y. Izumi, 1971a: Local free convection, similarity, and the budgets of shear stress and heat flux. *J. Atmos. Sci.,* **28,** 1171–1182.

——, Y. Izumi, and S. A. Collins, 1971b: Behavior of the refractive-index structure function parameter near the ground. *J. Opt. Soc. Amer.,* **61,** 1646–1650.

——, W. T. Pennell, D. H. Lenschow, and M. A. Lemone, 1978: The temperature-humidity covariance budget in the convective boundary layer. *J. Atmos. Sci.,* **35,** 47–58.

Yelland, M. J., and P. K. Taylor, 1996: Wind stress measurements from the open ocean. *J. Phys. Oceanogr.,* **26,** 541–558.

——, ——, I. E. Consterdine, and M. H. Smith, 1994: The use of the inertial dissipation technique for shipboard wind stress determination. *J. Atmos. Oceanic Technol.,* **11,** 1093–1108.